SIlicon Photonic Devices for Optoelectronic Integrated Circuits

Ming-Chun Tien

Electrical Engineering and Computer Sciences
University of California at Berkeley

Technical Report No. UCB/EECS-2009-118
http://www.eecs.berkeley.edu/Pubs/TechRpts/2009/EECS-2009-118.html

August 14, 2009

Silicon Photonic Devices for Optoelectronic Integrated Circuits

by

Ming-Chun Tien

B.S. (National Taiwan University) 2001
M.S. (National Taiwan University) 2003

A dissertation submitted in partial satisfaction of the

requirements for the degree of

Doctor of Philosophy

in

Engineering – Electrical Engineering and Computer Sciences

in the

Graduate Division

of the

University of California, Berkeley

Committee in charge:

Professor Ming C. Wu, Chair
Professor Constance Chang-Hasnain
Professor Xiang Zhang

Fall 2009

The dissertation of Ming-Chun Tien is approved:

Chair _____ Date _____

_____ Date _____

_____ Date _____

University of California, Berkeley

Silicon Photonic Devices for Optoelectronic Integrated Circuits

by Ming-Chun Tien

Abstract

Silicon Photonic Devices for Optoelectronic Integrated Circuits

by

Ming-Chun Tien

Doctor of Philosophy in Engineering – Electrical Engineering and Computer Sciences

University of California, Berkeley

Professor Ming C. Wu, Chair

Electronic and photonic integrated circuits use optics to overcome bottlenecks of microelectronics in bandwidth and power consumption. Silicon photonic devices such as optical modulators, filters, switches, and photodetectors have being developed for integration with electronics based on existing complementary metal-oxide-semiconductor (CMOS) circuits. An important building block of photonic devices is the optical microresonator.

On-chip whispering-gallery-mode optical resonators such as microdisks, microtoroids, and microrings have very small footprint, and thus are suitable for large scale integration. Micro-electro-mechanical system (MEMS) technology enables dynamic control and tuning of optical functions. In this dissertation, microring resonators with tunable power coupling ratio using MEMS electrostatic actuators are demonstrated. The fabrication is compatible with CMOS. By changing the physical gap spacing between the waveguide coupler and the microring, the quality factor of the microring can be tuned

from 16,300 to 88,400. Moreover, we have demonstrated optical switches and tunable optical add-drop filters with an optical bandwidth of 10 GHz and an extinction ratio of 20 dB. Potentially, electronic control circuits can also be integrated.

To realize photonic integrated circuits on silicon, electrically-pumped silicon lasers are desirable. However, because of the indirect bandgap, silicon is a poor material for light emission compared with direct-bandgap III-V compound semiconductors. Heterogeneous integration of III-V semiconductor lasers on silicon is an alternative to provide on-chip light sources. Using a room-temperature, post-CMOS optofluidic assembly technique, we have experimentally demonstrated an InGaAsP microdisk laser integrated with silicon waveguides. Pre-fabricated InGaAsP microdisk lasers were fluidically assembled and aligned to the silicon waveguides on silicon-on-insulator (SOI) with lithographic alignment accuracy. The assembled microdisk lasers exhibited a threshold pump of 0.6 mW and a maximum output power of 90 μW at room temperature under pulsed condition. The light was evanescently coupled to the waveguides on SOI for on-chip optical routing.

_____

Professor Ming C. Wu, Chair

TABLE OF CONTENTS

LIST OF FIGURES

LIST OF TABLES

ACKNOWLEDGEMENT

I would like to thank my advisor, Professor Ming C. Wu, for his mentorship and support in these five years. He provides the resources necessary for successful research work. Without his guidance, this work would not have come to fruition. I would also like to thank Professor Connie Chang-Hasnain, Professor Xiang Zhang and Professor Liwei Lin for being the committee in my qualify exam and giving a lot of feedback about my research.

In the past years, I have received great help from all the members of the Integrated Photonics Lab. Specifically, I would like to thank Sagi Mathai for his mentorship. He gave me much help when I first joined the group. I also benefited greatly from working with Professor Aaron Ohta, Dr. Kyoungsik Yu, Dr. Steven Neale, Arash Jamshidi, Jin Yao, Hsan-Yin "Tony" Hsu, Justin Valley, and Amit Lakhani. Professor Pei-Yu "Eric" Chiou, Professor Ming-Chang "Mark" Lee, and Chao-Hsi "Josh" Chi also gave me many suggestions about doing research. I also appreciate the valuable discussions with Professor Akio Higo, Jing-Yi Chen, Chi-Hung Lee.

I would also like to thank my friends for making my life more balanced in addition to academic research. I thank Melody Yin for being with me when I need encouragement. I also enjoy the time of travelling with Hsin-Yi Lin, Yu-Chih Nien, and Ya-Hui Hsu. I would also like to thank all my friends for making the life in Berkeley so much fun.

Finally, I thank my family for their support for my study so far away from home. I especially thank my twin brother for taking care of our family when I am pursuing my Ph.D. degree.

Chapter 1 Introduction

1.1 Silicon Photonics for Electron & Photonic Integrated Circuits

Since telephones lines were first constructed in the late nineteenth century, electrical interconnect has been crucial for information exchange. With advances in microelectronics, the information capacity of electrical wires increased greatly, however it was not sufficient to meet the dramatically increased amount of information. Starting in the late 70s, fiber-optic connections emerged as the most important method for high-bandwidth, high-speed, and large-capacity interconnects.

Figure 1.1 illustrates a physical hierarchy of interconnects based on different communication distances. It varies from several kilometers for the Metro/Wide Area Network (MAN/WAN) to a few microns for an intra-chip interconnect. Optical fiber has taken over the task of long-haul communication from electrical cables and is increasingly advancing in connections between different parts of large electronic systems [1]. Recent efforts have focused on using optics on circuit boards [2, 3] and even on integrated circuit chips [4-7]. Although electrical interconnects still dominate short-distance

communication, optical interconnects have the potential benefits of low power consumption, larger bandwidth density, and shorter signal delay compared to conventional electrical interconnects using copper wires.

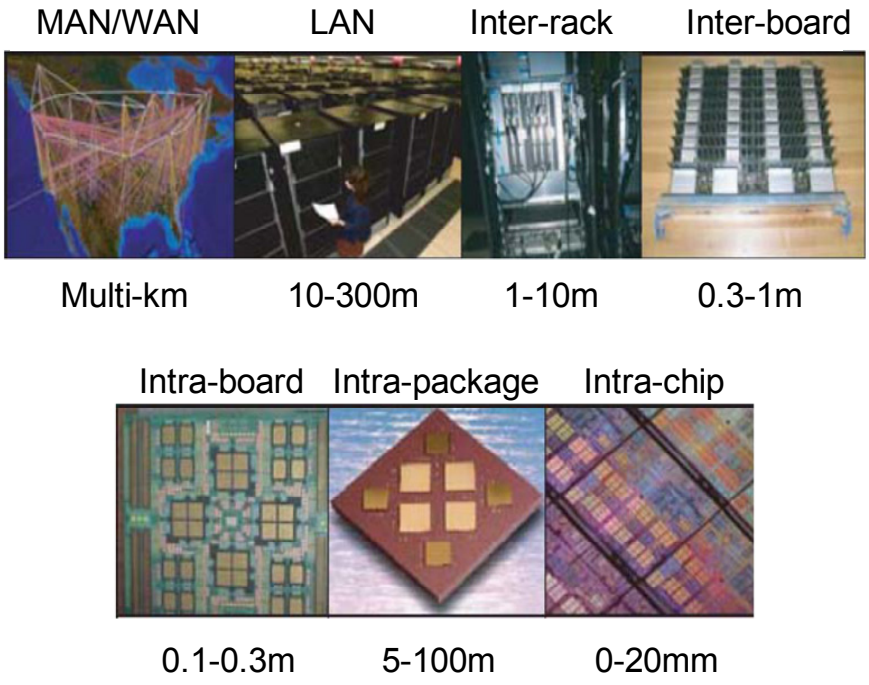

Figure 1.1 Physical hierarchy of optical interconnects from long-haul communication to intra-chip short distance interconnects. Figures are reproduced from [1].

One key challenge in the development of short-distance optical interconnects is the monolithic integration of various photonic devices with different functions. Photonic integrated circuits have been demonstrated on III-V semiconductor platforms; however, integration with existing complementary metal-oxide-semiconductor (CMOS) circuits offers attractive manufacturing advantages. For instance, commercial state-of-the-art CMOS silicon-on-insulator (SOI) foundries have been utilized in monolithic 1550-nm optoelectronic integration. Most optoelectronic devices, such as modulators [8-10],

optical filters [11], multiplexers [12], optical switches [13, 14], and photodetectors [15, 16], are demonstrated the capability of being made of silicon. Among them, integrated optical resonators are key elements to realize various functions, such as modulation, optical filtering and switching, optical delay time, and dispersion compensation. Micro-electro-mechanical system (MEMS) further leverages the capability of optical resonators by enabling the dynamic control and tunability. In the first part of this dissertation, we will demonstrate tunable microring optical resonators with integrated MEMS actuators and waveguides for ON-OFF wavelength switch and tunable optical add-drop filter applications.

The integration of photonic devices with microelectronic circuits could potentially realize low cost, high performance optical systems. There are two main trends for electronic and photonic integrated circuits (EPIC): CMOS front-end and back-end integrations. In the front-end integration, photonic circuits are merged with microelectronic circuits, and processed simultaneously. There are no further processes after CMOS, but modification to the CMOS process may be needed to accommodate photonic circuits. Luxtera Inc., for example, successfully uses 130-nm SOI CMOS processes to integrate optical transceivers with microelectronic circuits [17]. In the back-end integration, photonic and electronic circuits are processed on separate wafers or chips, and then attached together. This is also called post-CMOS integration and there is no need to change current CMOS processes. On the other hand, further processes are needed after CMOS to bring photonics to electronics. IMEC offers this CMOS-based heterogeneous integration and successfully demonstrates a prototype with the research group in the Ghent University in Belgium [18].

Although most optoelectronic devices have been demonstrated on silicon, the progress for on-chip lasers that can be directly integrated with CMOS circuits has been much slower. Silicon Raman lasers have been demonstrated but they still require external lasers for optical pumping [19, 20]. III-V compound semiconductor lasers have been grown directly on silicon substrate [21], but the growth temperature (> 400℃) is usually too high for post-CMOS processing. Direct bonding of III-V epitaxial materials on silicon offers a potential low-temperature process that is compatible with post-CMOS fabrication. Oxygen plasma and the thermosetting polymer divinylsiloxane-benzocyclobutene (DVS-BCB) have been employed to bond III-V materials to Si [22, 23]. AlGaInAs-Si hybrid evanescent lasers [24] and InP-based microdisk lasers [25] have been demonstrated using such bonding techniques. However, integrating lasers on fully-processed CMOS wafers presents some challenges. In SOI-based silicon photonics, the silicon waveguides are buried underneath many (up to ten) layers of electrical interconnects, as illustrated in Figure 1.2. Though bonding windows can be opened in the laser area, the nonplanar topography presents an additional challenge for wafer bonding. An alternative approach has been proposed to add an “optical interconnect layer” on top of CMOS circuits. However, the process is more complicated. The optical interconnect layer, together with the heterogeneously-integrated lasers, are fabricated on separate SOIs and then bonded on top of the CMOS wafers [26].

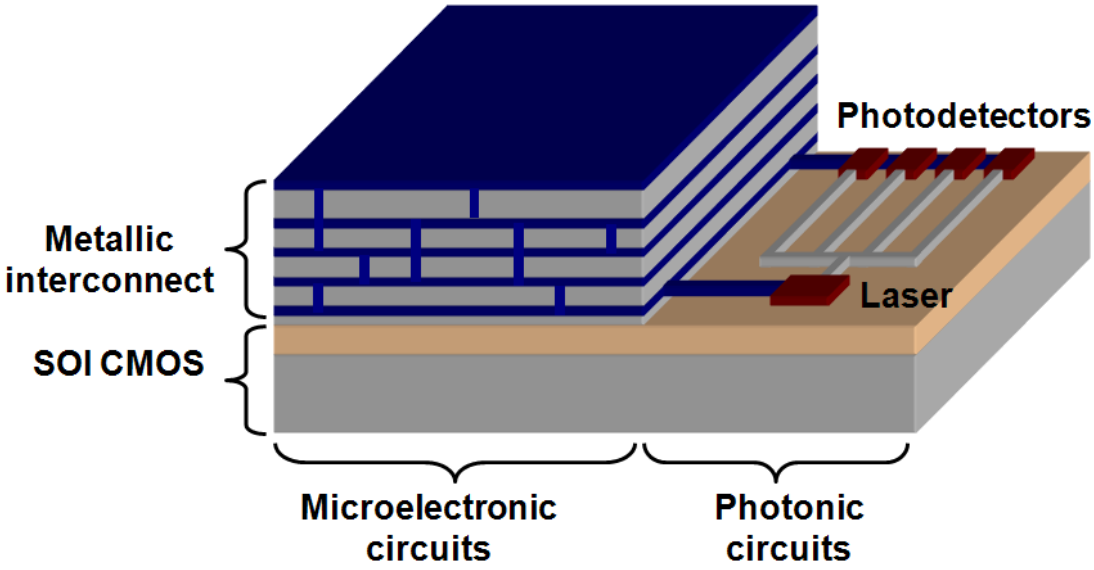

Figure 1.2 Schematic of the integration of III-V optoelectronic devices on SOI CMOS circuits.

In the second part of this dissertation, we will demonstrate a novel optofluidic assembly technique that can integrate prefabricated III-V semiconductor lasers on fully-processed CMOS wafers. The room-temperature optofluidic assembly process is realized using lateral-field optoelectronic tweezers (LOET), which can overcome the topography issue. It also allows for more efficient use of III-V epitaxial wafers. Using LOET, we have successfully assembled and aligned 200-nm-thick InGaAs/InGaAsP multiple-quantum-well (MQW) microdisk lasers to silicon waveguides on SOI with lithographic alignment accuracy. The transferred microdisk laser exhibits the same threshold pump power as similar lasers on their native InP substrate, as well as a maximum output power of 90 μW under pulsed condition.

1.2 Dissertation Overview

In Chapter 2, we give an overview of optical micro-resonators, including standing-wave and traveling-wave resonators, as well as various couplers for microresonators. Rectangular waveguide modes are then analyzed to derive the power coupling between waveguides and microring resonators. Optical resonators are modeled as R-L-C resonance circuits to obtain the different coupling regimes: under-, critically-, and over-coupled regimes. In addition, doublets resulting from the backscattering in the microring resonator are explained using coupled-mode theory.

In Chapter 3, we review tuning mechanisms of optical resonators, and then focus on power coupling tuning, which can be realized by incorporating electrostatic MEMS actuators. We also discuss the design of MEMS actuators and waveguide design to reduce the buckling issue due to stress. The tunable microring resonator with waveguide couplers is also described based on experimental evidence, and then compared with theoretical analysis. Finally, two applications, ON-OFF wavelength switches and tunable optical add-drop filters are demonstrated using the coupling-tunable microring resonators.

In Chapter 4, we theoretically analyze the microdisk laser with integrated output waveguides, and then discuss the design issues. The microdisk lasers are optimized for low threshold and high differential quantum efficiency by adjusting the thickness and radius of microdisk lasers, and the distance between the microdisk lasers and output waveguides.

In Chapter 5, optoelectronic tweezers (OET), the manipulation tool that we use for optofluidic assembly, is introduced. The operation principle and device model are briefly

explained. We also introduce other variations of OET that can be integrated with silicon photonic circuits for microdisk laser assembly.

In Chapter 6, we experimentally demonstrate optofluidic assembly of InP-based microdisk lasers onto silicon photonic circuits with the assistance of LOET. The lithographic assembly accuracy provides precise alignment between the microdisk lasers and the integrated output waveguides.

Finally, Chapter 7 concludes the dissertation and gives an overall perspective on the electronic and photonic integrated circuits.

Chapter 2 Whispering-Gallery Mode Micro-cavity Resonator

2.1 Review of Micro-cavity Resonators

Optical resonators can be realized by utilizing either total internal reflection between a dielectric material and the surrounding cladding media or distributed Bragg reflection (DBR) from periodical structures, such as multilayered reflectors or arrays of holes (photonic crystals), to form a cavity where optical waves resonate at specific wavelengths (resonance wavelengths). The spectra of optical modes supported by microresonators are determined by the size and shape of the cavity. There are two types of optical microresonators: traveling-wave and standing-wave resonators. In a traveling-wave resonator, optical waves propagate in a uni-direction at resonance wavelengths. A typical example is a whispering-gallery mode (WGM) in microsphere, microdisk, microtoroid, or microring resonators. In a standing-wave resonator, optical waves propagate back and forth between the reflectors and form a standing wave. The commonly used reflectors for

standing-wave resonators are cleaved waveguide mirrors, distributed Bragg reflectors, and photonic crystals.

To excite the optical waves in the microresonators, proper couplers are required. In early days, prism couplers with frustrated total internal reflection were the main methods to couple light in and out of optical resonators, although they require bulk optics for the focus and alignment of the light source [27-29]. With optimum gap spacing between the prism and the resonator, the coupling efficiency was demonstrated up to 80% from the prism to the resonator [28]. Alternatively, side-polished fiber couplers [30, 31], pigtailed couplers using angled-polished fiber tips [32], and tapered optical fibers [33, 34] are utilized to couple light into the resonators. The tapered fiber coupler has several distinct advantages such as the built-in coupler alignment, relatively simple fabrication, and control of the coupling efficiency by the change of the fiber radius. However, the couplers need to be mounted on micropositioners to precisely control the distance between the couplers and the resonators.

For photonic integrated circuits, it is desirable to use integrated waveguide couplers. Because of optical mode overlap between the waveguide and the resonator, the optical power can be evanescently coupled into the resonators. The coupling efficiency is controlled by the optical mode overlap between the resonator and the waveguide, matching the mode propagation constants, or changing the length of the evanescent-field coupling region. Figure 2.1 summaries various types of couplers for microresonators [35].

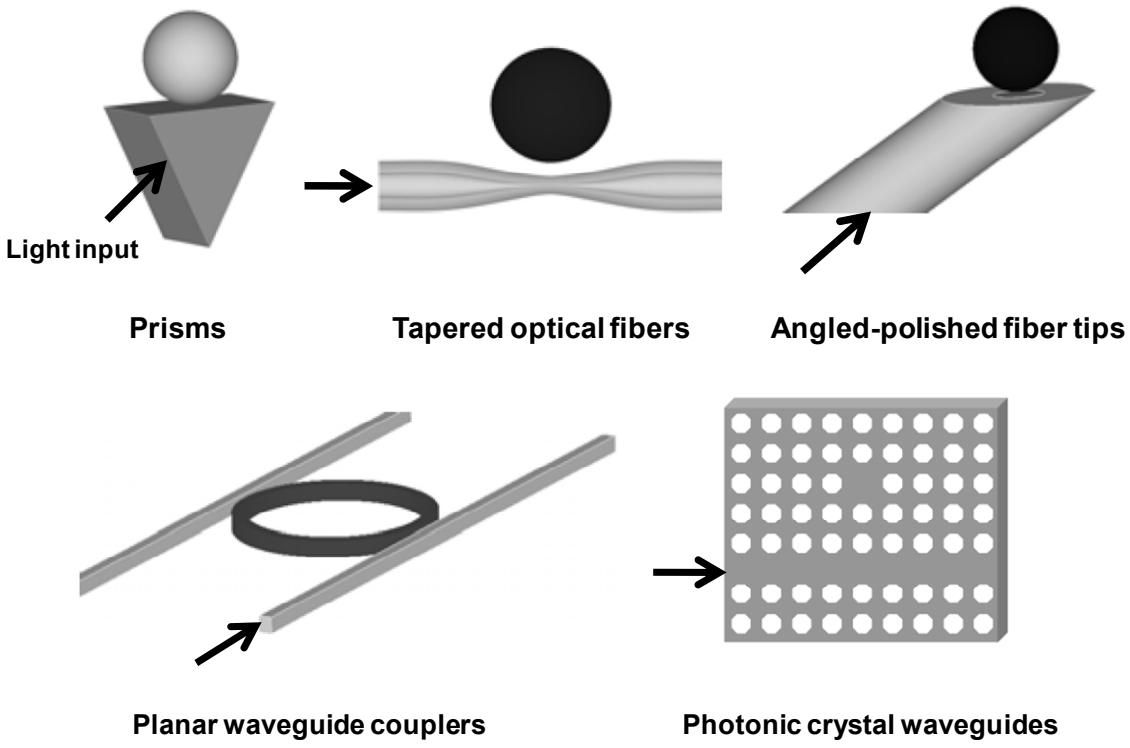

Figure 2.1 Various types of couplers for optical microresonators.

2.2 Microring Resonators with Waveguide Couplers

On-chip optical resonators are key elements in the implementation of the optical functions such as optical filtering, optical modulation, optical delay time, and dispersion compensation. Silicon microring resonators are compact devices that can be easily integrated with optical waveguide couplers as part of photonic circuits. The small footprint of the silicon microring resonator enables the possibility of large-scale photonic integration. To characterize microring resonators with waveguide couplers, we will first discuss some figures of merit.

2.2.1 Quality Factor

A quality factor (Q) is an indication of how fast the optical energy stored in the resonator is dissipated. It is defined by

$$Q \equiv \frac{\omega W}{P_d}, \tag{2.1}$$

where ω is resonance angular frequency of the resonator, W is the stored energy in the resonator, P_d is the power dissipated in the resonator. From conservation of power, the definition implies that the time-dependence for the decay of the energy inside the resonator in the absence of further excitation of the cavity is given by

$$W(t) = W(0)\exp\left(\frac{-\omega t}{Q}\right). \tag{2.2}$$

By a simple Fourier transform, the Q can be measured in spectrum domain. The formula is given by

$$Q = \frac{\omega}{\delta\omega} = \frac{\lambda}{\delta\lambda}, \tag{2.3}$$

where $\delta\omega$ and $\delta\lambda$ are the full width at half maximum (FWHM) of the resonance in frequency and wavelength domains, respectively.

Another common term for optical resonators is the photon lifetime, τ, which is defined by the required time for the energy to decay to e^{-1} of its original value. The relation between the photon lifetime and Q is given by,

$$Q \equiv \omega\tau\ . \tag{2.4}$$

Since Q is an indication of optical loss in the cavity, it can be related to the loss coefficient, α (in linear scale), by the following formula:

$$Q = \frac{\omega}{\alpha v_g}, \tag{2.5}$$

where v_g and α are the group velocity and loss coefficient of the optical mode in the resonator.

Looking into the resonator losses that result in the quality factor, there are two types of losses: waveguide coupling loss and intrinsic loss in the resonator. A general quality factor can thus be expressed as

$$\frac{1}{Q} = \frac{1}{Q_c} + \frac{1}{Q_0}, \tag{2.6}$$

where Q_c represents the quality factor due to waveguide coupling and Q_0, the unloaded Q, represents the quality factor due to intrinsic loss. In general, Q_c is affected by the waveguide-to-microring power coupling ratio, while Q_0 is determined by the power dissipation in the microring resonator due to bending loss, surface scattering, surface absorption, free carrier absorption, and two-photon absorption [36].

2.2.2 Free Spectral Range

Free spectral range (FSR) is defined as the frequency spacing or wavelength spacing between the modes of an optical cavity. Generally speaking, the FSR always increases as the physical size of the resonator shrinks. From an engineering perspective, a larger FSR allows for the development of single-mode and high-efficiency lasers from materials with broadband gain. A larger FSR also allows narrowband filtering for dense wavelength

division multiplexing (DWDM) without crosstalk between channels. The FSR also gives us the information of group velocity in the resonator. It can be derived from the following expression:

$$\Delta\lambda = \frac{\lambda^2}{2\pi R n_g}, \tag{2.7}$$

where $\Delta\lambda$ is the FSR, λ is the optical wavelength in free space, R is the radius of the microring resonator, n_g is the group index of the optical mode in the resonator, and the group velocity is given by

$$v_g = \frac{c}{n_g}, \tag{2.8}$$

where c is the speed of light.

2.2.3 Power Coupling Ratio

The power coupling ratio (κ) is a measure of how much optical power is coupled from the waveguide to the microring resonator. It is also related to the quality factor due to waveguide coupling, Q_c, given by

$$Q_c = \frac{\omega T}{\kappa}, \tag{2.9}$$

where $T = \frac{2\pi R}{v_g}$ is the round-trip time of the microring resonator.

2.3 Design of Waveguide Couplers

2.3.1 Analysis of Silicon Rectangular Waveguides

An important design parameter for waveguide couplers is the power coupling ratio between the rectangular waveguide and the microring resonator. In order to obtain the power coupling ratio, the optical mode in the rectangular waveguide is analyzed using Marcatili's method [37, 38], which assumes the electromagnetic field in the shaded area in Figure 2.2 can be neglected since the electromagnetic field of a well-guided mode decays rapidly in the cladding region. The refractive index of the waveguide core is n_1 while that of the cladding is n_0. The waveguide width and thickness are denoted by 2a and 2d.

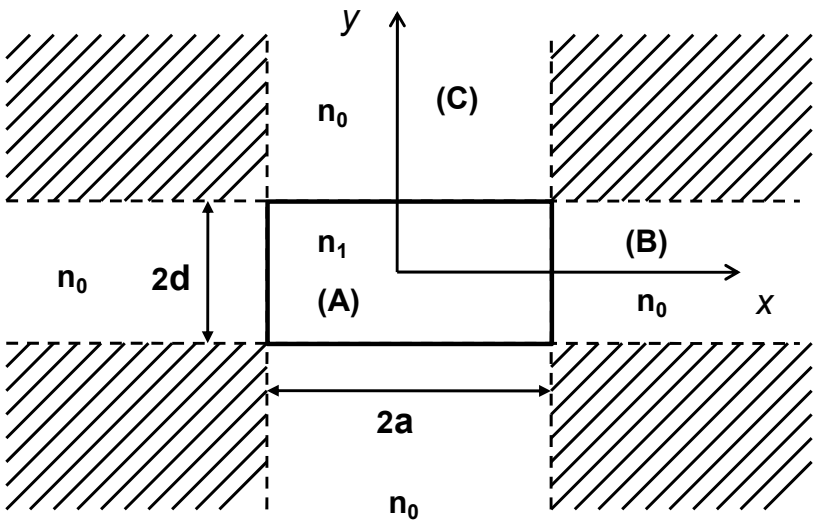

Figure 2.2 Cross-sectional view diagram of a rectangular waveguide.

The rectangular waveguide can support a dominant electric field either in *x* direction (E_{pq}^{x} modes, p=q=1 for the fundamental mode) or in *y* direction (E_{pq}^{y} modes, p=q=1 for the fundamental mode). The following analysis is based on E_{pq}^{x} modes. The E_{pq}^{y} modes

can be analyzed in the same method. According to Marcatili's model, the *x*-component of the magnetic field is set to zero ($H_x=0$) for E_{pq}^{x} modes, and then the electromagnetic field can be expressed as follows based on Maxwell's equations:

$$\begin{aligned}
&\frac{\partial^2 H_y}{\partial x^2}+\frac{\partial^2 H_y}{\partial y^2}+\left(k^2 n^2-\beta^2\right)H_y=0\\
&H_x=0\\
&H_z=\frac{-j}{\beta}\frac{\partial H_y}{\partial y}\\
&E_x=\frac{\omega\mu_0}{\beta}H_y+\frac{1}{\omega\varepsilon_0 n^2\beta}\frac{\partial^2 H_y}{\partial x^2}\\
&E_y=\frac{1}{\omega\varepsilon_0 n^2\beta}\frac{\partial^2 H_y}{\partial x\partial y}\\
&E_z=\frac{-j}{\omega\varepsilon_0 n^2}\frac{\partial H_y}{\partial x}
\end{aligned} \quad , \tag{2.10}$$

where n is the refractive index, k is the free-space wavenumber, β is the propagation constant, ω is the optical frequency, and ε_0 and μ_0 are the permittivity and permeability, respectively. For the fundamental mode of the waveguide, the *y*-component of the magnetic field at different regions can be written as

$$H_y=\begin{cases}
A\cos(k_x x)\cos(k_y y) & (A)\\
A\cos(k_x a)\cos(k_y y)\exp[-\gamma_x(x-a)] & (B)\\
A\cos(k_x x)\cos(k_y d)\exp[-\gamma_y(y-d)] & (C)
\end{cases} \quad , \tag{2.11}$$

where k_x, k_y, γ_x, and γ_y are the transverse wavenumbers. (A), (B), and (C) represent the regions inside the waveguide, on the top of the waveguide, and to the right of the waveguide (Figure 2.2). Since the waveguide is symmetric, we only analyze the top and right cladding regions, and the electromagnetic field in the bottom and left cladding

regions can be derived by symmetry. The transverse wavenumbers and the propagation constant satisfy the following relations:

$$\begin{cases} -k_x^2 - k_y^2 + k^2 n_1^2 - \beta^2 = 0 & (A) \\ \gamma_x^2 - k_y^2 + k^2 n_0^2 - \beta^2 = 0 & (B) \\ -k_x^2 + \gamma_y^2 + k^2 n_0^2 - \beta^2 = 0 & (C) \end{cases} . \tag{2.12}$$

The β in the above equations can be eliminated and the relation of k_x, k_y, γ_x, and γ_y can be written as

$$\begin{aligned} \gamma_x^2 &= k^2(n_1^2 - n_0^2) - k_x^2 \\ \gamma_y^2 &= k^2(n_1^2 - n_0^2) - k_y^2 \end{aligned} . \tag{2.13}$$

When we apply the boundary conditions, the z-component electric field $E_z \propto (1/n^2)\frac{\partial H_y}{\partial x}$ should be continuous at $x=a$ and the z-component magnetic field $H_z \propto \frac{\partial H_y}{\partial y}$ should be continuous at $y=d$. Two dispersion equations for the eigenvalues are obtained.

$$\begin{aligned} k_x a &= \tan^{-1}\left(\frac{n_1^2 \gamma_x}{n_0^2 k_x}\right) \\ k_y d &= \tan^{-1}\left(\frac{\gamma_y}{k_y}\right) \end{aligned} . \tag{2.14}$$

From Equation (2.13) and (2.14), all the transverse wavenumbers, k_x, k_y, γ_x, and γ_y , can be solved. The propagation constant β is then obtained from

$$\beta^2 = k^2 n_1^2 - (k_x^2 + k_y^2) . \tag{2.15}$$

2.3.2 Power Coupling between Two Waveguides

The coupling coefficient between two identical parallel rectangular waveguides (Figure 2.3) is well known and can be expressed as [38]

$$c_0 = \begin{cases} \dfrac{\omega\varepsilon_0(n_1^2 - n_0^2)\int_{-a}^{a}\int_{-d}^{d} E_{1x}^* E_{2x}\,dxdy}{2\int_{-\infty}^{\infty}\int_{-\infty}^{\infty} E_{1x}^* H_{1y}\,dxdy} & \text{(for } E_{pq}{}^{x} \text{ modes)} \\ \dfrac{\omega\varepsilon_0(n_1^2 - n_0^2)\int_{-a}^{a}\int_{-d}^{d} E_{1y}^* E_{2y}\,dxdy}{2\int_{-\infty}^{\infty}\int_{-\infty}^{\infty} E_{1y}^* H_{1x}\,dxdy} & \text{(for } E_{pq}{}^{y} \text{ modes)} \end{cases}, \qquad (2.16)$$

where c_0 is the coupling coefficient between two identical parallel waveguides, E_{1x}, E_{1y}, H_{1x}, and H_{1y} are x- and y-components of the electrical and magnetic fields in waveguide 1, and E_{2x} and E_{2y} is x- and y-component of the electric field in waveguide 2.

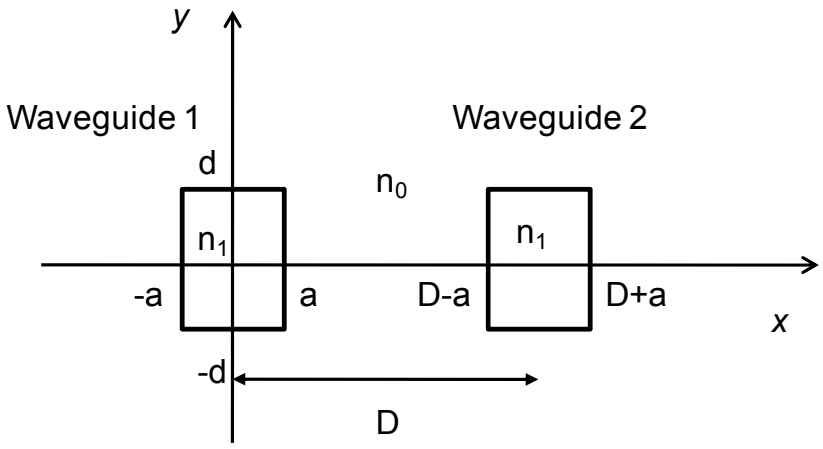

Figure 2.3 Directional coupler consisting of two rectangular waveguides.

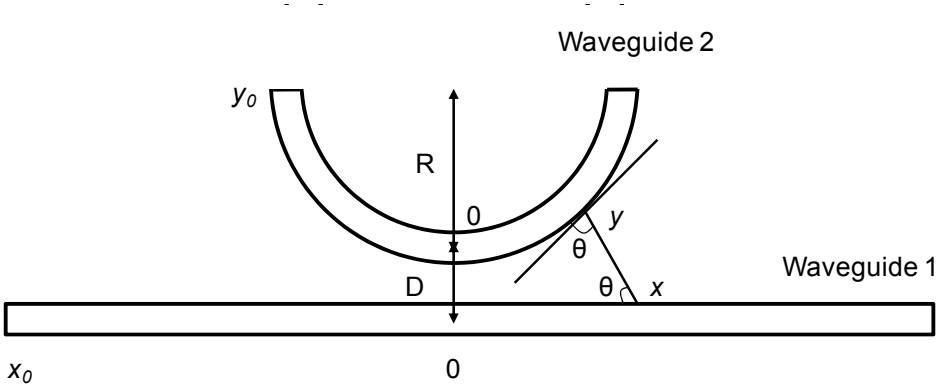

Figure 2.4 Geometry of a straight waveguide and a semi-ring waveguide. R is the radius of the ring and D is the center-to-center spacing between these two waveguides.

We are primarily interested in the coupling between a straight waveguide and a microring. To analyze this problem, a modified coupling model has been proposed by Matsuhara et al. using a curved transmission line approach based on curvilinear coordinates [39]. The geometry of a coupler consisting of a straight waveguide and a semi-ring is illustrated in Figure 2.4. Wave theory predicts that the entire field distribution in waveguide 1 contributes to the field at position *y* in waveguide 2. However, rigorous calculations of the coupling interaction are difficult. To obtain an analytical description, we made a simplifying assumption that only the field in a certain position of waveguide 1 contributes to the field in another position of waveguide 2. The corresponding coupling positions in the two waveguides follow $\theta_1 = \theta_2 = \theta$, where θ_1 is the angle between line $\overline{xy}$ and the straight waveguide 1, θ_2 is that between line $\overline{xy}$ and the tangent to semi-ring waveguide 2. In order to follow this relation, *x* and *y* are related by the following equation on curvilinear coordinates.

$$x = (2R + D)\tan\frac{y}{2R} \ , \tag{2.17}$$

where R is the radius of the ring and D is the closest center-to-center distance between the semi-ring and the straight waveguide.

The coupling coefficient between the straight waveguide and the semi-ring waveguide can thus be modified as [39]

$$\begin{aligned} c_{12} &= c_0 \cos(\pi - 2\theta)\left(\frac{dy}{dx}\right)^{1/2} = \frac{c_0 \cos\left(\frac{y}{R}\right)}{\sqrt{1+\frac{D}{2R}\sec\left(\frac{y}{2R}\right)}} \\ c_{21} &= c_0 \cos(\pi - 2\theta)\left(\frac{dx}{dy}\right)^{1/2} = c_0 \cos\left(\frac{y}{R}\right)\sqrt{1+\frac{D}{2R}}\sec\left(\frac{y}{2R}\right) \end{aligned} \ , \tag{2.18}$$

where c_{12} and c_{21} are the coupling coefficients from waveguide 2 to waveguide 1 and from waveguide 1 to waveguide 2, respectively. Using Equations (2.16)-(2.18), the straight waveguide-to-microring coupling coefficient distribution along the propagation direction for various gap spacing is plotted in Figure 2.5. The dimensions of the waveguide and the ring are 350 nm wide and 500 nm thick, and the radius of the ring is 20 μm for calculation. The E_{11}^{x} optical mode encounters stronger coupling than the E_{11}^{y} optical mode for the same gap spacing. This is because the E_{11}^{x} optical mode is less confined in a tall, narrow waveguide, resulting in more optical field overlap between the microring and the waveguide. In both cases, most of the coupling occurs in the 10 μm region where these two waveguides are closest.

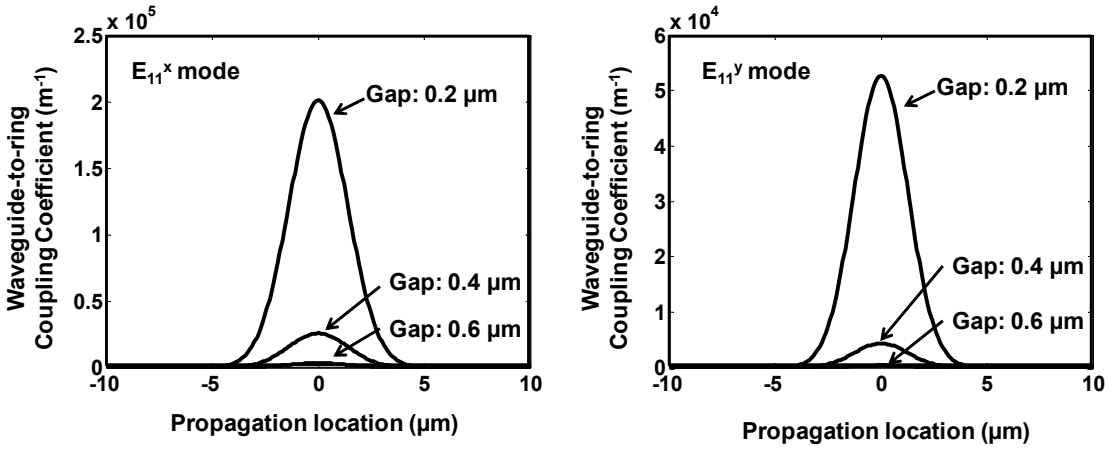

(a) (b)

Figure 2.5 Waveguide-to-ring coupling coefficients along the propagation direction for various gap spacing in the cases of (a) E_{11}^{x} modes and (b) E_{11}^{y} modes, respectively. The widths and thicknesses of the straight waveguide and the microring are 350 nm and 500 nm, while the radius of the ring is 20 μm.

Since the dimensions of the microring and straight waveguide are the same, the propagation constants are approximately the same ignoring the bending effect for a large-radius ring. The power in the ring (P_2) and waveguide (P_1) can be expressed as [38]

$$\begin{aligned} P_2 &= \sin^2(c_{21}x) \\ P_1 &= 1-\sin^2(c_{21}x) \end{aligned}, \tag{2.19}$$

where x is the propagation distance along the straight waveguide. From Equations (2.18) and (2.19), the power coupling ratio from the straight waveguide to the microring can be obtained. Figure 2.6 plots the power coupling ratio versus the gap distance for (a) the E_{11}^{x} mode and (b) the E_{11}^{y} mode. For the E_{11}^{x} mode, when the gap is less than 0.4 μm, the power coupling ratio increases dramatically and oscillates in the small-gap region because the power is oscillating between the waveguide and the ring. A similar situation also occurs for the E_{11}^{x} mode. However, because of the smaller coupling coefficient, the power coupling ratio only bounces back once when the gap is smaller than 0.02 μm.

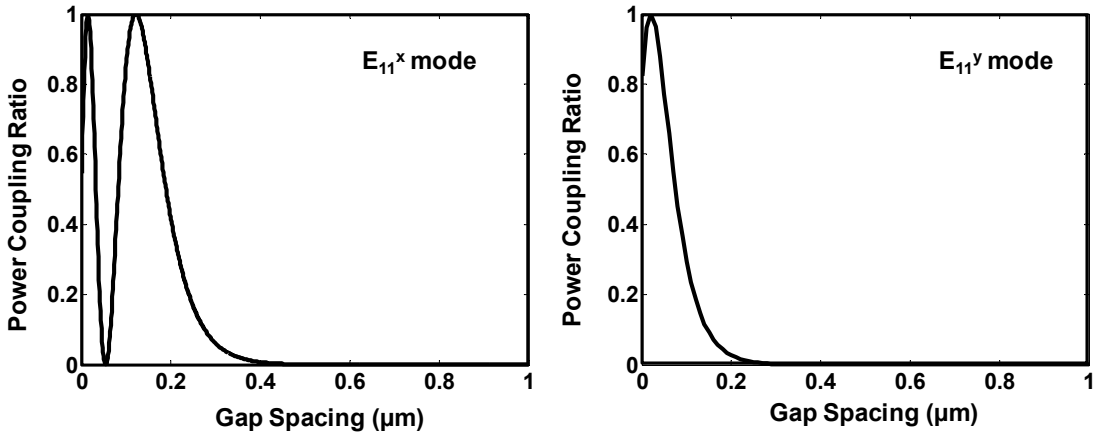

(a) (b)

Figure 2.6 Power coupling ratio from the straight waveguide to the microring versus gap spacing in the cases of (a) E_{11}^x modes and (b) E_{11}^y modes, respectively. The waveguide and the ring are both 350 nm wide and 500 nm thick.

2.4 Mathematical Model of Microring Resonators with Waveguide Couplers

2.4.1 Microring with a Single Waveguide Coupler

The phenomenon of resonance is a general one that can occur in mechanical, electrical, and optical forms. Mechanical resonance usually involves a spring and a mass while electrical resonance happens in R-L-C circuits. Both are analyzed using second-order differential equations. Optical resonance is analogous to R-L-C resonance and can be analyzed in the same way [40].

Figure 2.7 illustrates a microring optical resonator with a waveguide coupler and the corresponding R-L-C circuits. a_{in} and a_t denote the input and transmitted optical fields, respectively, while a_c represents the field in the cavity. κ and γ_0 are the power coupling ratio and intrinsic cavity loss during one round-trip time, which is denoted as T. The

resonance angular frequency of the cavity is denoted as ω_0. The optical mode coupled to the microring resonator can be described by the following equation:

$$\frac{d}{dt}a_c = i\omega_0 a_c - \left(\frac{\gamma_0}{2T} + \frac{\kappa}{2T}\right)a_c + i\frac{\sqrt{\kappa}}{T}a_{in} \ . \tag{2.20}$$

Here, γ_0/T and κ/T represent the decay rate of the field due to intrinsic cavity loss and coupling loss to the waveguide.

In the absence of the coupling from the waveguide, we can derive the energy dissipation rate in the cavity from the above equation:

$$P_d = \frac{d}{dt}W = a_c^* \frac{d}{dt}a_c + a\frac{d}{dt}a_c^* = \left(\frac{\gamma_0}{T} + \frac{\kappa}{T}\right)W \ , \tag{2.21}$$

where W is the total energy stored in the cavity and P_d is the dissipated power. According to the definition of quality factor in Equation (2.1),

$$\frac{1}{Q} = \frac{P_d}{\omega W} = \frac{\gamma_0}{\omega T} + \frac{\kappa}{\omega T} = \frac{1}{Q_0} + \frac{1}{Q_c}, \tag{2.22}$$

where Q_0 and Q_c are the intrinsic quality factor (unloaded Q) and the quality factor due to coupling loss. The total quality factor, Q, is also called loaded Q.

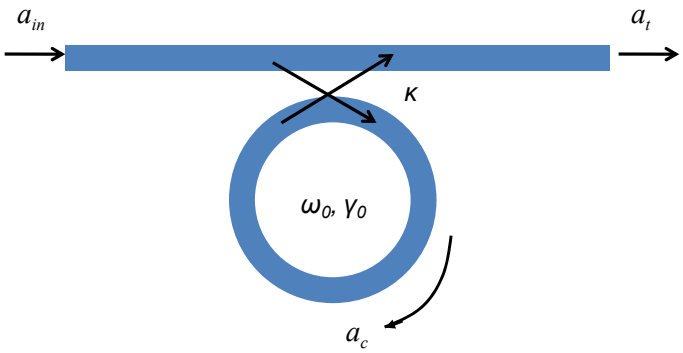

(a)

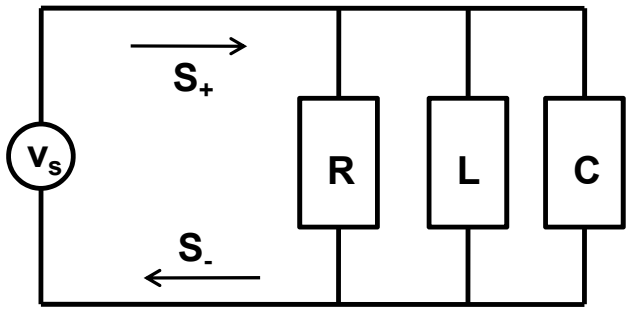

(b)

Figure 2.7 (a) Schematic of an optical microring resonator with a single waveguide coupler. (b) The corresponding R-L-C circuit model with external excitation.

Another important property for resonators is transmission spectrum. From Figure 2.7(a), the transmitted optical field is contributed from the transmittance of input field (a_{in}) and the coupling of the field in the microring (a_c), which can be described as

$$a_t = \sqrt{1-\kappa}\,a_{in} + i\sqrt{\kappa}\,a_c \,. \tag{2.23}$$

If the input optical field is sinusoidal, $a_{in} \propto \exp(i\omega t)$, we can solve the steady-state solution of Equation (2.20) and substitute it into Equation (2.23). For a high-Q resonator ($\gamma_0, \kappa << 1$), the power transmittance is thus obtained and expressed as follows:

$$\left(\frac{a_t}{a_{in}}\right)^2 = \left|\frac{\frac{\gamma_0}{2T} - \frac{\kappa}{2T} + i(\omega-\omega_0)}{\frac{\gamma_0}{2T} + \frac{\kappa}{2T} + i(\omega-\omega_0)}\right|^2 . \tag{2.24}$$

The transmission properties are commonly characterized by under-coupling ($\kappa < \gamma_0$), critically-coupling ($\kappa = \gamma_0$), and over-coupling ($\kappa > \gamma_0$). In the under-coupled regime, the power coupling rate from the waveguide is smaller than the intrinsic loss rate in the cavity, while in the over-coupled regime, the power coupling rate is larger than the

intrinsic loss rate. The transmission spectra of both cases exhibit a resonance dip, however the FWHM of the resonance dip in the over-coupled regime is larger because of the smaller loaded Q (Figure 2.8 (a) and (c)). When the resonator operates in the critically-coupled regime, the power coupling rate from the waveguide to the resonator is equal to the loss rate in the resonator. In this case, the power in the resonance wavelengths vanishes in the transmission spectrum because of the destructive interference of the field transmitted from the input and the field coupled from the resonator (Figure 2.8(b))

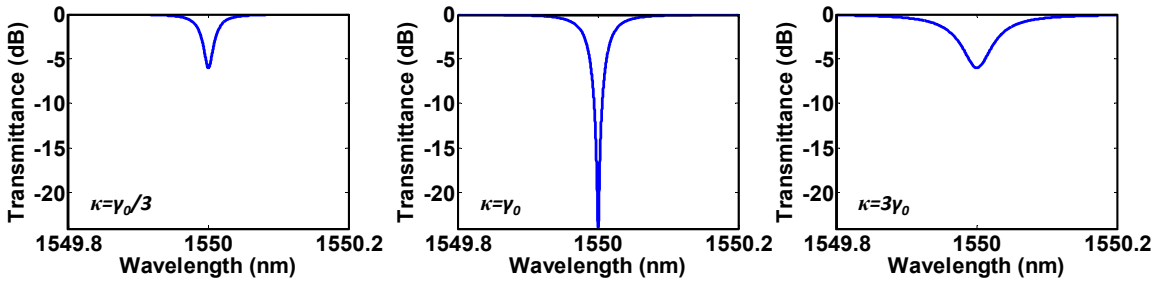

(a) (b) (c)

Figure 2.8 Calculated transmission spectra of a microring resonator operated in (a) under-coupled, (b) critically-coupled, and (c) over-coupled regimes. The resonance wavelength is set at 1550 nm.

2.4.2 Microring with Two Waveguide Couplers

For the application of optical add-drop filters, a microring resonator is integrated with two waveguide couplers as shown in Figure 2.9. Different from the microring with a single waveguide coupler, this device has four ports: input, through, add, and drop. Similar to Equation (2.20), the optical mode coupled to the resonator can be written as

$$\frac{d}{dt}a_c = i\omega_0 a_c - \left(\frac{\gamma_0}{2T} + \frac{\kappa_1}{2T} + \frac{\kappa_2}{2T}\right)a_c + i\frac{\sqrt{\kappa_1}}{T}a_{in} + i\frac{\sqrt{\kappa_2}}{T}a_a \ , \qquad (2.25)$$

where κ_1 and κ_2 are the power coupling ratios between the microring and waveguide 1 and waveguide 2, respectively. The input optical field from the add port is denoted as a_a. To simplify the analysis, the excitation from the add port is assumed to be zero. The optical field in the through and drop ports can be written as

$$\begin{aligned} a_t &= \sqrt{1-\kappa_1}\, a_{in} + i\sqrt{\kappa_1}\, a_c \\ a_d &= i\sqrt{\kappa_2}\, a_c \end{aligned} . \tag{2.26}$$

For a time-harmonic input optical field ($a_{in} \propto \exp(i\omega t)$) and high-Q resonators ($\gamma_0, \kappa_1, \kappa_2 << 1$), the solution to Equation (2.25) in a steady-state can be solved and substituted into Equation (2.26). Then we can obtain the spectra at the through and drop ports.

$$\begin{aligned} \left(\frac{a_t}{a_{in}}\right)^2 &= \left|\frac{\gamma_0 + \kappa_2 - \kappa_1 + i2T(\omega-\omega_0)}{\gamma_0 + \kappa_2 + \kappa_1 + i2T(\omega-\omega_0)}\right|^2 \\ \left(\frac{a_d}{a_{in}}\right)^2 &= \left|\frac{-2\sqrt{\kappa_1\kappa_2}}{\gamma_0 + \kappa_2 + \kappa_1 + i2T(\omega-\omega_0)}\right|^2 \end{aligned} . \tag{2.27}$$

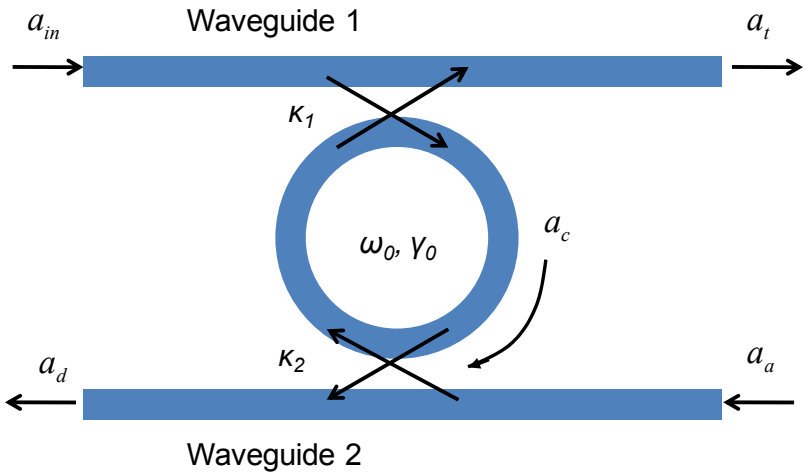

Figure 2.9 Schematic of a microring resonator with two waveguide couplers.

2.5 Mode Intercoupling in Microring Resonators: Doublets

The splitting of degenerate levels in the presence of coupling is a common phenomenon in physics. The formation of energy bands in a semiconductor can be attributed to this phenomenon, as well as the splitting of atomic levels in the presence of coupling. Similar phenomena could happen in WGM optical resonators, such as microspheres, microdisks, microtoroids, and microrings. Each mode in the WGM resonator possesses a natural 2-fold degeneracy, resulting from different propagation directions, clockwise (CW) and counterclockwise (CCW). When these two modes couple to each other via backscattering in the resonator, the degeneracy is lifted, and splitting of the resonance mode is observed. The same situation can be observed by designing two identical resonators coupled to each other since they have the same optical modes. Here we will expand the resonator model discussed in Section 2.4, and analyze the behavior of the microring resonator due to backscattering.

Rayleigh scattering from surface inhomogeneities or density fluctuations in a WGM resonator will transfer power from the initially excited mode to all the confined and radiative modes. The scattering to all modes other than the CW and CCW modes is included in the overall intrinsic loss (Q_0) of the resonator. The backscattering either from the CW to CCW mode or from the CCW to CW mode results in intercoupling of these two modes. The coupling of modes can be described using coupled-mode theory and slowly varying envelope approximation [41, 42]. Assuming only one excitation from the input port (Figure 2.10), the coupled-mode equations for the microring with two waveguide couplers can be described as

$$\begin{aligned}
&\frac{d}{dt}a_{cw}+\left[\frac{1}{2}\left(\frac{\gamma_0}{T}+\frac{\kappa_1}{T}+\frac{\kappa_2}{T}\right)+i(\omega_0+\Delta\omega)\right]a_{cw}=i\frac{\beta}{2T}a_{ccw}+i\frac{\sqrt{\kappa_1}}{T}a_{in}\\
&\frac{d}{dt}a_{ccw}+\left[\frac{1}{2}\left(\frac{\gamma_0}{T}+\frac{\kappa_1}{T}+\frac{\kappa_2}{T}\right)+i(\omega_0+\Delta\omega)\right]a_{ccw}=i\frac{\beta}{2T}a_{cw}
\end{aligned}, \tag{2.28}$$

where a_{in} denotes the input optical field, while a_{cw} and a_{ccw} represent the CW and CCW modes in the cavity. The power coupling ratio to waveguide 1 and 2, backscattering power ratio, and intrinsic cavity loss during one round-trip time, which is denoted as T, are κ_1, κ_2, β, and γ_0. The excitation frequency is detuned by $\Delta\omega$ with respect to the resonance frequency ω_0 of the initially degenerate modes.

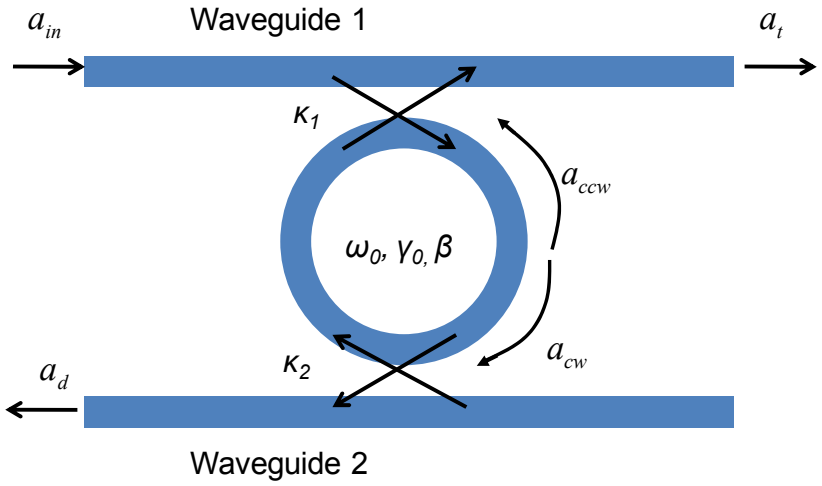

Figure 2.10 Illustration of coupling of the CW and CCW modes in a microring ring resonator with two waveguide couplers. β represents backscattering power ratio during one round-trip.

Similar to Equation (2.26), the output in the through (a_t) and drop (a_d) ports can be written as

$$\begin{aligned}
a_t &= \sqrt{1-\kappa_1}\,a_{in}+i\sqrt{\kappa_1}\,a_{cw}\\
a_d &= i\sqrt{\kappa_2}\,a_{cw}
\end{aligned}. \tag{2.29}$$

In order to simplify the analysis, we consider a single waveguide coupler case first ($\kappa_1 = \kappa$, $\kappa_2 = 0$). For a high-Q resonator ($\gamma_0, \kappa << 1$), the power transmission can be derived by solving the steady-state solution of Equation (2.28) and substituting it into Equation (2.29).

$$\left|\frac{a_t}{a_{in}}\right|^2 = \left|\frac{\left(\frac{\gamma_0}{2T}\right)^2 - \left(\frac{\kappa}{2T}\right)^2 + \left(\frac{\beta}{2T}\right)^2 - (\omega_0 + \Delta\omega)^2 + i\Delta\omega(\omega_0 + \Delta\omega)\frac{\gamma_0}{T}}{\left(\frac{\gamma_0 + \kappa}{2T}\right)^2 + \left(\frac{\beta}{2T}\right)^2 - (\omega_0 + \Delta\omega)^2 + i(\omega_0 + \Delta\omega)\left(\frac{\gamma_0 + \kappa}{T}\right)}\right|^2 . \quad (2.30)$$

It is interesting that the critically-coupled regime with zero power transmission changes with the existence of backscattering. We can define new coupling regimes as follows: (1) under-coupled regime when $\kappa^2 < \gamma_0^2 + \beta^2$, (2) critically-coupled regime when $\kappa^2 = \gamma_0^2 + \beta^2$, (3) over-coupled regime when $\kappa^2 > \gamma_0^2 + \beta^2$. Figure 2.11 shows the transmission spectra with different coupling regimes. When the resonator operates in the critically-coupled regime, the transmission power vanishes at the resonance frequency ($\Delta\omega = 0$) as what is observed for the ideal microring resonators without backscattering. However, when the resonator operates in the under-coupled regime, double resonance dips (doublets) are observed because the mode coupling between the CW and CCW modes lifts the degeneracy. The locations of the doublets with respect to the resonance follow the relation described as

$$\Delta\omega = \pm\frac{1}{2T}\sqrt{\gamma_0^2 + \beta^2 - \kappa^2} . \quad (2.31)$$

The separation increases with backscattering power ratio, but decreases with the power coupling ratio from the waveguide. When the resonator operates in the over-coupled

regime, the doublet disappears in the transmission spectrum. Only one resonance dip is observed as the case without backscattering in the microring resonator.

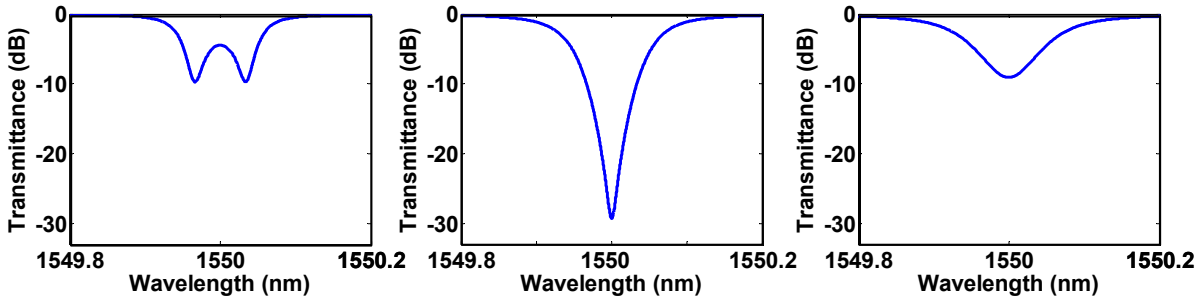

Figure 2.11 Calculated transmission spectra of a microring resonator with backscattering in the cavity operated in (a) under-coupled, (b) critically-coupled, and (c) over-coupled regimes. The resonance wavelength is set at 1550 nm.

For a microring resonator with two waveguide couplers as an add-drop filter (Figure 2.10), the doublets can also be observed in the drop port in addition to the through port. The transmission spectra at the through and drop ports can be derived from Equations (2.28) and (2.29). The analytic solution can be written as follows:

$$\left|\frac{a_t}{a_{in}}\right|^2 = \left|\sqrt{1-\kappa_1} - \frac{\left(\frac{\kappa_1}{T}\right)\left(\frac{1}{2}\left(\frac{\gamma_0+\kappa_1+\kappa_2}{T}\right)+i(\omega_0+\Delta\omega)\right)}{\left(\frac{1}{2}\left(\frac{\gamma_0+\kappa_1+\kappa_2}{T}\right)+i(\omega_0+\Delta\omega)\right)^2+\left(\frac{\beta}{2T}\right)^2}\right|^2$$
$$\left|\frac{a_d}{a_{in}}\right|^2 = \left|\frac{-\frac{\sqrt{\kappa_1\kappa_2}}{T}\left(\frac{1}{2}\left(\frac{\gamma_0+\kappa_1+\kappa_2}{T}\right)+i(\omega_0+\Delta\omega)\right)}{\left(\frac{1}{2}\left(\frac{\gamma_0+\kappa_1+\kappa_2}{T}\right)+i(\omega_0+\Delta\omega)\right)^2+\left(\frac{\beta}{2T}\right)^2}\right|^2 \quad (2.32)$$

Figure 2.12 shows typical transmission spectra at the through and drop ports of a microring resonator operated in the under-coupled regime. Both through and drop ports

exhibit doublets in the transmission spectra due to backscattering in the microring resonator.

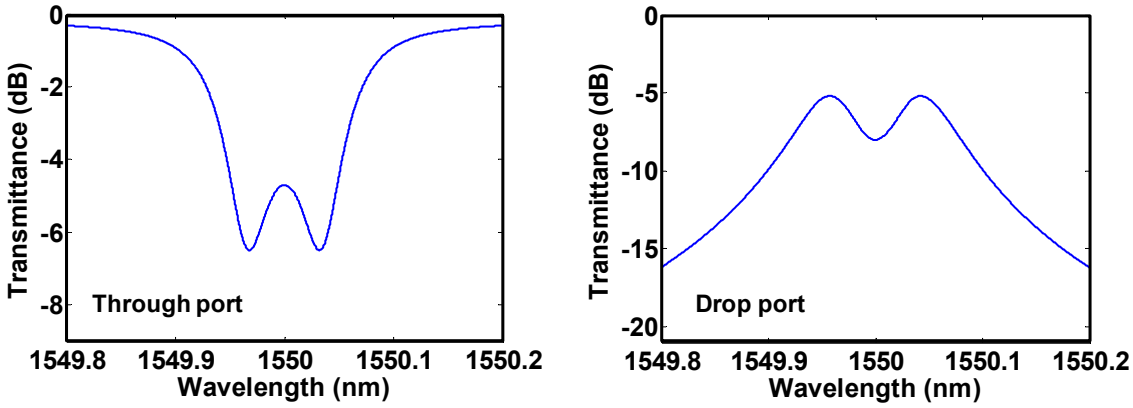

(a) (b)

Figure 2.12 Transmission spectra of a microring resonator with two waveguide couplers at the (a) through port and (b) drop port. The resonator is operated in the under-coupled regime. With backscattering in the resonator, a doublet is observed in both through and drop ports. The parameters used in the calculation are: γ_0=0.01, β=0.1, κ_1= κ_2=0.04.

Despite the fact that a symmetric doublet in the transmission spectrum is predicted by the coupled-mode theory, an asymmetric doublet is observed more often [36, 43, 44]. The asymmetry of the doublet can be attributed to the reflection from both ends of the waveguide [43]. As shown in Figure 2.13(a), the reflected optical field is taken into consideration as part of the excitation to the microring resonator. The coupled-mode theory described in Equation (2.28) can be modified as follows for the single waveguide coupler case:

$$\begin{aligned}\frac{d}{dt}a_{cw}+\left[\frac{1}{2}\left(\frac{\gamma_0}{T}+\frac{\kappa}{T}\right)+i\left(\omega_0+\Delta\omega\right)\right]a_{cw}&=i\frac{\beta}{2T}a_{ccw}+i\frac{\sqrt{\kappa}}{T}\left(ta_{in}+ra_r\right)\\ \frac{d}{dt}a_{ccw}+\left[\frac{1}{2}\left(\frac{\gamma_0}{T}+\frac{\kappa}{T}\right)+i\left(\omega_0+\Delta\omega\right)\right]a_{ccw}&=i\frac{\beta}{2T}a_{cw}+i\frac{\sqrt{\kappa}}{T}ra_t\end{aligned}, \tag{2.33}$$

where t and r are the transmittance and reflectivity of the optical field at the facet of the waveguide. a_t and a_r represent the optical fields that pass through and reflect from the resonator, respectively. The transmitted and reflected optical fields of the resonator can be written as

$$\begin{aligned}a_t&=\sqrt{1-\kappa}\left(ta_{in}+ra_r\right)+i\sqrt{\kappa}a_{cw}\\ a_r&=\sqrt{1-\kappa}\left(rA_r\right)+i\sqrt{\kappa}a_{ccw}\end{aligned}, \tag{2.34}$$

where $r^2+t^2=1$. To clarify the influence of the reflection at the waveguide facets on transmission spectrum, we use an equivalent transmittance of the resonator, t_{res}, to replace the dotted box in figure 2.13(a). t_{res} can be written as [45]

$$t_{res}=\frac{A_t}{tA_{in}+rA_r}. \tag{2.35}$$

The total transmittance of the optical field including Fabry-Perot effect is then written as

$$t_{tot}=\frac{t^2\exp(ik_0Ln_{eff})t_{res}}{1-r^2\exp(i2k_0Ln_{eff})t_{res}^2}, \tag{2.36}$$

where L is the length of the waveguide, k_0 is free space propagation constant, and n_{eff} is the effective refractive index of the waveguide. Figure 2.14 shows a typical transmission spectrum of a microring resonator operating in the under-coupled regime with partial reflection at the ends of the waveguide. The doublet is asymmetric due to the reflection at the waveguide facets. In addition, the spectrum also exhibits ripple-like oscillation in the passband because of the Fabry-Perot effect.

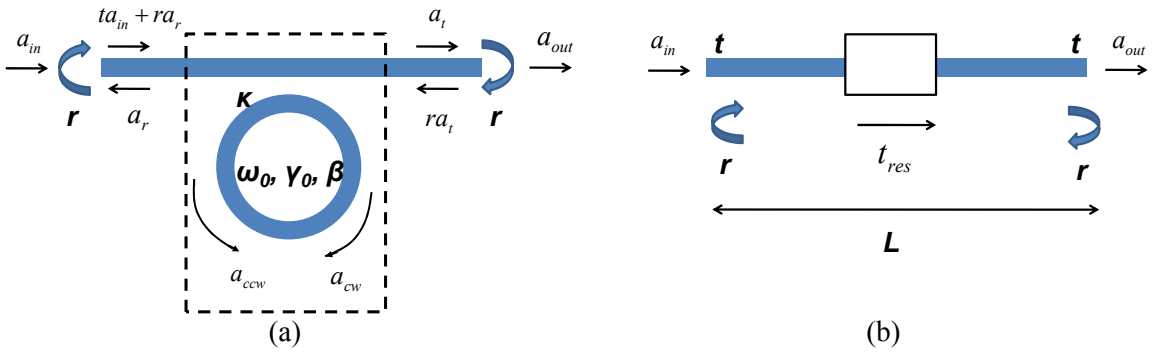

Figure 2.13 (a) Illustration of a microring with a single waveguide coupler. The microring has a backscattering power ratio of β. The optical field is partially reflected at both ends of the waveguide. (b) The equivalent model of the resonator using the equivalent transmittance of the resonator, t_{res}, to represent the dotted box in (a). The reflectivity and transmittance of the optical field at the waveguide facet are denoted by *r* and *t*, respectively.

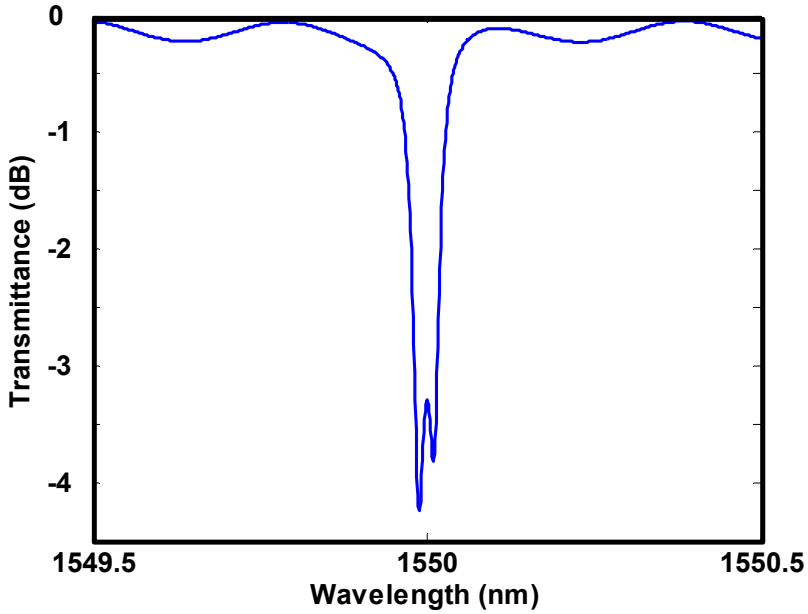

Figure 2.14 Transmission spectrum of a microring with a single waveguide coupler. The reflection at the waveguide facet is taken into consideration, resulting in an asymmetric doublet as well as a Fabry-Perot oscillation in the passband. The parameters used in the calculation are: γ_0=0.023, β=0.033, κ=0.01, r=0.1, L= 1 mm.

Chapter 3 Tunable Microring Resonators Using MEMS Actuators

In this chapter, we discuss the performance of microring resonators with integrated waveguide couplers. The schematic diagrams are depicted in Figure 3.1. Microring resonators with a single integrated waveguide can be used as dynamic optical notch filters or ON-OFF wavelength switches (Figure 3.1(a)) while those with two waveguides can be used as reconfigurable optical add-drop multiplexers (ROADM) or bandpass filters (Figure 3.1(b)). Thanks to the planar structure of microring resonators and waveguides, MEMS actuators can be integrated to move the waveguide coupler and thus control the power coupling ratio from the waveguide to the resonator.

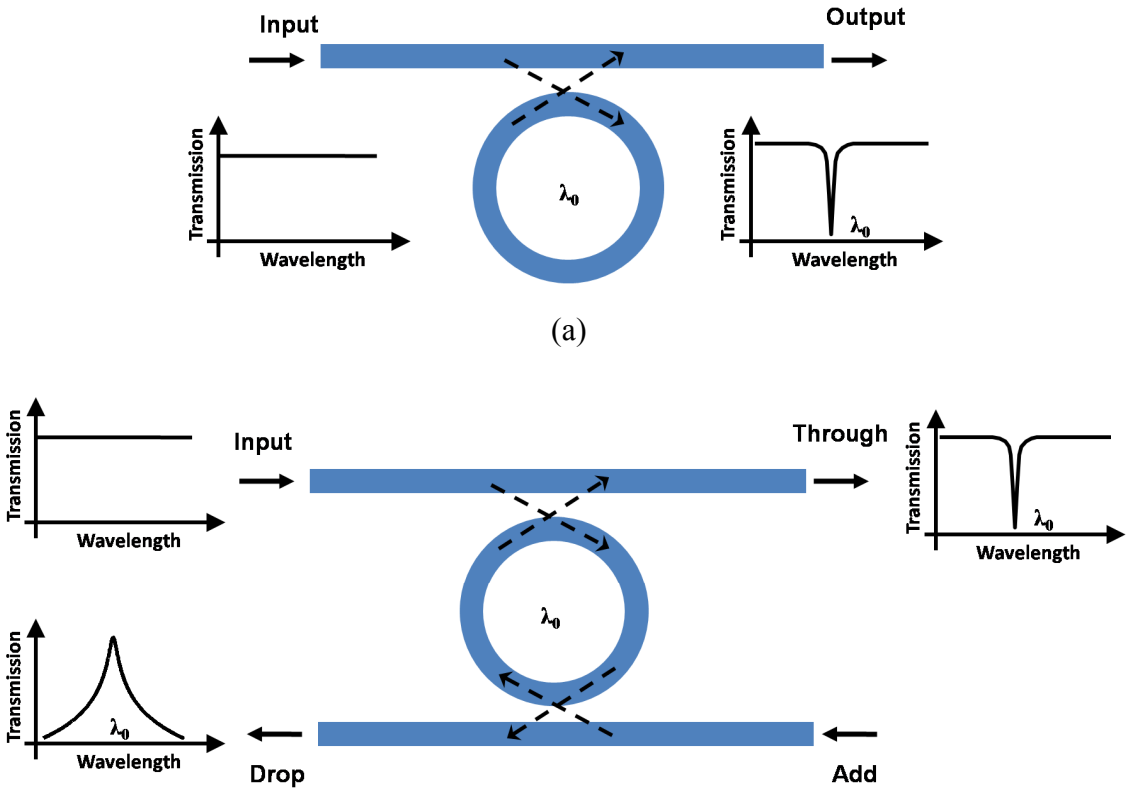

Figure 3.1 Schematic of microring resonators integrated with (a) a single waveguide as an optical notch filter or an ON-OFF wavelength switch (b) two waveguides as an optical add-drop multiplexer or a bandpass filter.

3.1 Tuning of Optical Microresonators

The performance of optical microresonators is primarily determined by three parameters: resonator loss, the power coupling ratio between the resonator and the waveguides, and resonance wavelengths. The resonator loss results from the optical power dissipation in the resonator cavity, while the resonance wavelength is determined by the refractive index and the optical path length of the cavity. The power coupling ratio depends on how much the power transfers via the evanescent fields between the waveguide and the microresonator. Altering any of these three parameters can change the microresonator properties. Tuning of the resonator loss or power coupling ratio can vary

the transmission power and bandwidth, while tuning of the resonance wavelengths shifts the transmission spectrum, as illustrated in Figure 3.2.

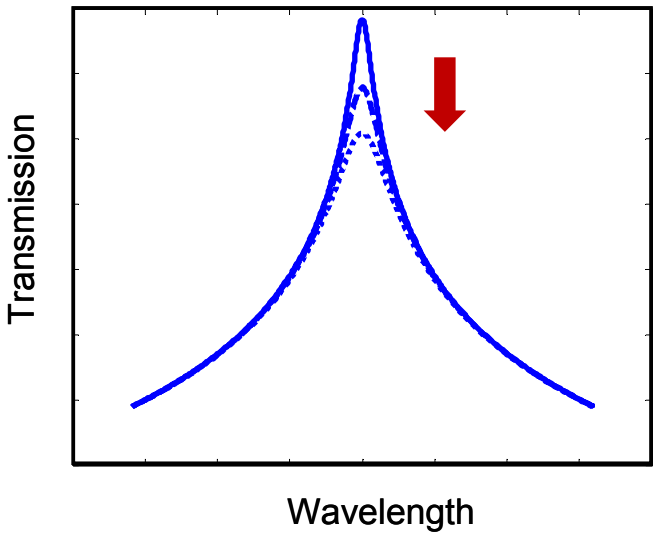

(a)

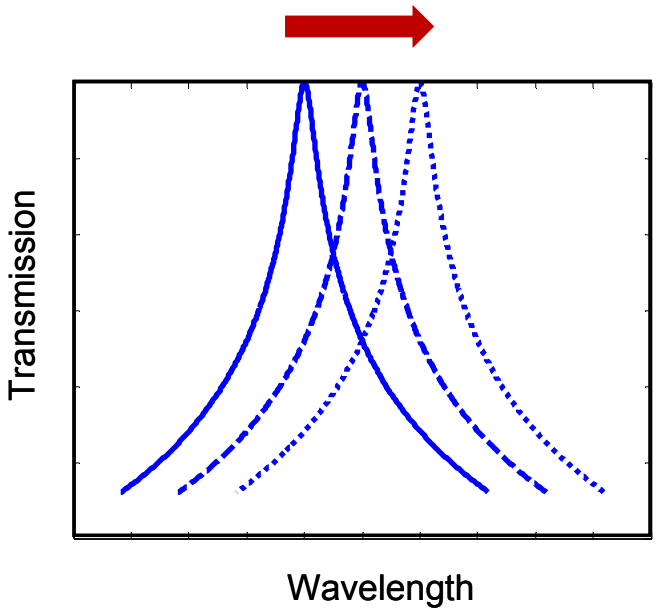

(b)

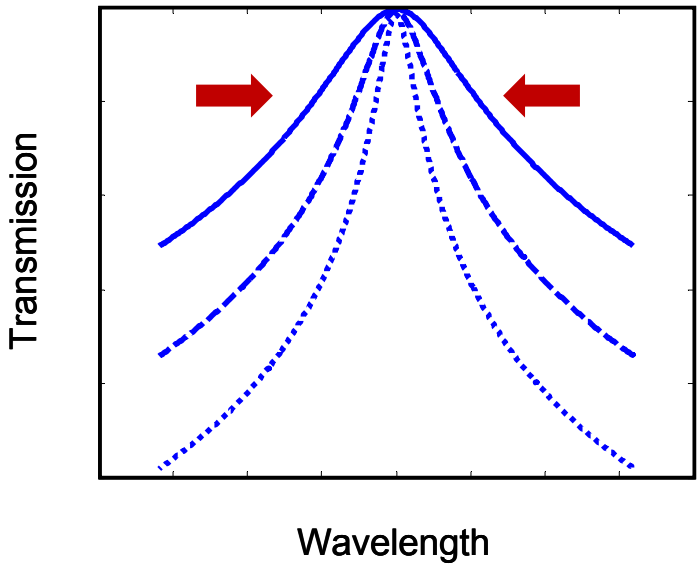

(c)

Figure 3.2 The transmission spectra of the microresonator with tunable (a) insertion loss, (b) resonance wavelength, and (c) transmission bandwidth. Tuning the resonator loss or power coupling ratio varies the insertion loss and transmission bandwidth, while tuning the resonance wavelength shifts the passband wavelength.

Most of the tuning mechanisms reported in literature focus on varying the resonator loss and the resonance wavelengths. The resonator loss can be controlled by attaching a lossy metal film to spoil the Q and achieve a switching function [46]. For III-V compound active microresonators, the resonator loss can also be tuned by electroabsorption [47], and gain trimming effects [48, 49]. The loss tuning is generally utilized for applications in ROADM and dynamic switches.

The resonance wavelength can be tuned by changing the refractive index of the resonator by local heating [12, 50-52], the electro-optical effect [53], or free carrier injection [54, 55]. It also can be tuned via a direct change of cavity size by applying physical strain [56-58]. These devices usually have applications in tunable optical filters.

Despite the large quantity of literature about resonator loss and resonance wavelength tuning, most of the microfabricated resonators reported to date have fixed power coupling ratios. For microresonators with integrated waveguides, the power coupling ratio is determined by the gap spacing between the resonator and the waveguides, defined by microfabrication. However, the power coupling ratio is very sensitive to gap spacing, and it can change dramatically, especially for those waveguides with high index contrast. It is very challenging to fabricate a waveguide integrated resonator with an exact power coupling ratio as designed.

Therefore, controlling the power coupling ratio to achieve the optimum performance is highly desirable. As mentioned in Section 2.1, prism couplers [27-29], side-polished fiber couplers [30, 31], pigtailed couplers using angled-polished fiber tips [32], and tapered optical fibers can be utilized to couple light into the resonators [33, 34]. The power coupling ratio is controlled by physically changing the gap spacing between those couplers and the resonators. With piezo-controlled micropositioners, moving tapered fiber couplers controls the power coupling ratio very well [36], however, the setup is bulky and not easily integratable.

Recently, control of the power coupling ratio of microresonators in integrated systems has been reported [45, 59, 60]. A Mach-Zehnder interferometer (MZI) has been integrated with a racetrack resonator [59], which can operate in all coupling regimes (uncoupled, under-coupled, critically-coupled, and over-coupled). An unloaded Q of 1.9×10^4 and an extinction ratio of 18.5 dB have been achieved. However, the circumference of the resonator is as large as 1.43 mm due to the long MZI structure,

which limits the free spectral range. In addition, the large footprint may restrict its application in large-scale integration. A microring resonator integrated with smaller interferometric couplers and microheaters has been demonstrated [61] as a bandwidth-tunable filter. The unloaded Q of the resonator is approximately 1.5×10^4 while the extinction ratio is more than 23 dB. The bandwidth can be tuned from 0.1 nm to 0.7 nm on a footprint of less than 0.001 mm^2. However, due to the current-driven microheaters, the power consumption is large, especially for the microresonators which are made of poor thermal conductive materials. A microfluidic approach has also been deployed to tune both resonance wavelength and the power coupling ratio of low-index microring resonators made of UV-curable epoxy SU8 [62]. The refractive index of the surrounding media is controlled by mixing two different liquids, and critical coupling with an extinction of 37 dB is achieved. However, the tuning range of the power coupling ratio is small due to the small index variation (~0.04). In addition, the tuning speed is slow (~2 sec) because a well-mixed solution is needed to stabilize the output.

With the advances in fabrication technologies, MEMS actuation has become a viable and effective means to control the gap spacing precisely between the microresonators and the waveguide coupler [45, 60, 63]. The devices have a small footprint for large-scale monolithic integration. Compared with the tuning mechanism using current injection, electrostatic MEMS actuators have much lower power consumption and a larger tuning range. Table 3.1 summarizes all the tuning mechanisms.

Tuning parameters	Controlled variables	Mechanisms
Resonance wavelength	Refractive index	Thermo-optics [12, 50-52]
	Refractive index	Electro-optics [53]
	Refractive index	Free carrier injection [54, 55]
	Cavity size	Strain control (MEMS) [56-58]
Resonator loss	Propagation loss	Metal-attachment (MEMS) [46]
	Propagation loss	Electro-absorption [47]
	Propagation amplification	Gain trimming [48,49]
Power coupling ratio	Effective coupling coefficient	Thermo-optics [61] Interferometry [59]
	Surrounding refractive index	Fluidic mixture [62]
	Coupling gap	Gap tuning (MEMS) [45,60,63]

Table 3.1 Summary of different tuning mechanisms of microresonators.

3.2 Microring Resonators with MEMS-actuated Waveguides

In order to have a small footprint, low power consumption, precise coupling gap control, and CMOS compatible processes, we propose a microring optical resonator with tunable waveguide couplers actuated by pairs of electrostatic actuators as illustrated in Figure 3.3 [64]. With proper bias voltages applied to the actuator electrodes, the waveguides can be actuated and thus the coupling gap can be controlled to vary the power coupling ratio. The optical power is evanescently coupled from the integrated waveguide to the microring resonator. The device has potential applications for bandwidth-tunable optical filters, reconfigurable optical add-drop multiplexers, dispersion compensators, and dynamic optical switches and crossconnects.

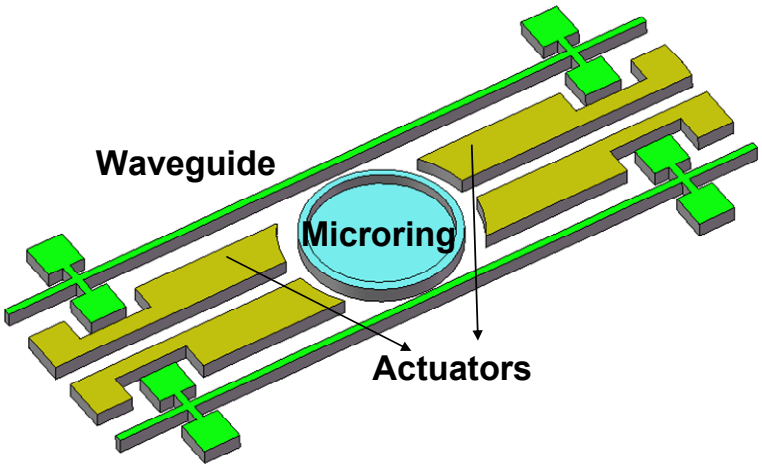

Figure 3.3 Schematic of a microring resonator with integrated silicon optical waveguides and electrostatic MEMS actuators.

3.2.1 Design of Electrostatic Actuators

Electrostatic actuators are utilized to actuate waveguide couplers because of the advantages of low power consumption and a small footprint. To design a proper electrostatic actuator, we have to analyze the waveguide deformation due to actuation. The silicon waveguide with two anchors on both ends can be considered a fixed-fixed beam. Assuming a continuous electrode is parallel to the waveguide with fixed separation (Figure 3.4), the complete governing beam equation can be written as [65-67]

$$EI\frac{\partial^4}{\partial x^4}g_{w-e}(x)-\left[hw\sigma_0(1-\nu)+hwE\frac{\Delta L_w}{L_w}\right]\frac{\partial^2}{\partial x^2}g_{w-e}(x)=-\frac{\varepsilon_0 hV^2}{2\left|g_{w-e}(x)\right|^2}(1+F_r), \quad (3.1)$$

where $g_{w\text{-}e}(x)$ is the gap between the waveguide and the electrode, E is the Young's module of silicon, $I=\frac{1}{12}w^3h$ is the moment of inertia of the waveguide, w is the waveguide width, h is the waveguide thickness, σ_0 is the biaxial residual stress in the waveguide (positive for tension and negative for compression), ν is the Poisson ratio of

silicon, L_w is the length of the suspended waveguide, ΔL_w is the length change due to deformation, V is the applied voltage to the electrode, $F_r = 0.65\frac{g_{w-e}(x)}{h}$ is the fringing-field correction.

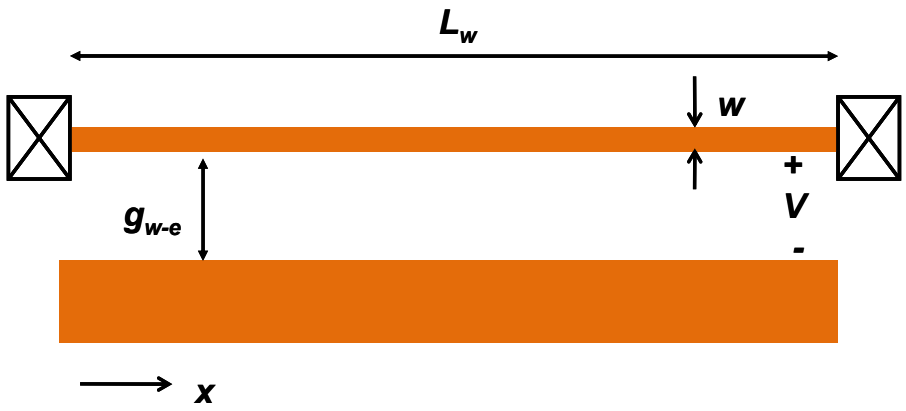

Figure 3.4 Fixed-fixed waveguide with a continuous parallel electrode. L_w: suspended waveguide length, $g_{w\text{-}e}$: gap between the waveguide and the electrode which is a function of x when applying bias voltages, w: waveguide width, V: applied voltage.

The applied electrostatic force is stored in three mechanical formats: bending, residual stress, and strain-induced stress. The first term of Equation (3.1) is contributed by bending, while the second and third terms are contributed by residual stress and strain-induced stress, respectively. When the waveguide is elongated due to deformation, the strain induces tensile stress, which increases the stiffness of the waveguide. This is called the strain-stiffening effect. Numerical solutions of the waveguide from Equation (3.1) can give us complete information of waveguide actuation, including the pull-in voltage and waveguide travel range before pull-in happens.

A simplified analytic solution can facilitate the actuator design. We parameterize the beam deflection using a constant beam shape *f(x)* and deflection parameter *a* so that the gap between the resonator and the waveguide can be written as

$$g_{w-e}(x) = g_0 - af(x), \tag{3.2}$$

where g_0 is the original gap spacing between the waveguide and the electrode before actuation, and x is between 0 and L_w. Note that this is a reasonable first-order approximation for beams that are dominated by purely stress effects from either residual stress or strain-induced stress. Assume beam deflection is much less than beam length ($a << f'(x)$),

$$\Delta L_w = \int_0^{Lw} \sqrt{1 + \left(af'(x)\right)^2}\, dx - L_w \approx ca^2, \tag{3.3}$$

where $c = \frac{1}{2}\int_0^{Lw} \left(f'(x)\right)^2 dx$. Therefore, the strain term, $\Delta L_w/L_w$, scales to the first order as the square of deflection *a*. Substituting Equation (3.3) into Equation (3.1), we get a new expression for the governing equation:

$$\left[EI\frac{d^4}{dx^4}f(x) + hw\sigma_0(1-\nu)\frac{d^2}{dx^2}f(x)\right]a + \left(chwE\frac{d^2}{dx^2}f(x)\right)a^3 = F_{elec}, \tag{3.4}$$

where $F_{elec} = -\frac{\varepsilon_0 h V^2}{2\left[g_{w-e}(x)\right]^2}\left(1 + F_r\right)$ is the electrostatic force. The terms proportional to *a* give rise to the usual linear beam stiffness, represented in lumped models by a linear Hooke's law spring, while the strain-stiffening effect gives rise to the term proportional to a^3, a cubic spring. The beam is dominated by a linear spring for a small deflection and

a cubic spring for a large deflection. We consider that the pull-in effect happens when the beam has a large deflection and is dominated by a cubic spring. Using a cubic spring lumped model and ignoring the fringing field, the travel distance is 60% of the gap before pull-in happens. For a regular linear spring, the travel distance is one third of the gap. We know the travel range for a fixed-fixed beam should be in-between, but closer to 60% since pull-in happens in a large deflection.

For our application, the electrode of the actuator is divided into two regions since the microring resonator is incorporated in the center, as shown in Figure 3.5. The actuators are located on the two sides of the microring, resulting in an absence of electrostatic force to the center of the waveguide. The force is applied only to the portions of the waveguide close to the anchors, which deflect less than the center waveguide; therefore, the travel range is increased [65]. The complete calculation is done by commercial software using the finite element method, COMSOL. A beam profile solved by the two-dimensional COMSOL simulation is shown in Figure 3.6(a). Each curve represents the beam profile under the bias voltage from 10 V to 100 V with a step of 10 V. The suspended waveguide length is 180 μm, and the electrode length is 60 μm. The gap spacing between the waveguide and the electrode is 3.85 μm for the simulation. The beam profile under a continuous electrode actuation (Figure 3.4) without incorporation of the microring is also shown in Figure 3.6(b) for comparison. The waveguide without force applied to the middle region becomes flatter in the center than that with distributed forces over the entire waveguide, and thus the coupling region between the waveguide and the resonator is also increased at the expense of larger actuation voltage. The calculated travel range is approximately 2.5 μm under 213 V bias. It should be noted that the residual stress of the

structure and fringing field are ignored in the calculation. Both compressive stress and fringing field can increase the travel range [65, 66]. To operate the device under a reasonable bias voltage, the gap between the waveguide and the resonator is designed approximately 1 μm.

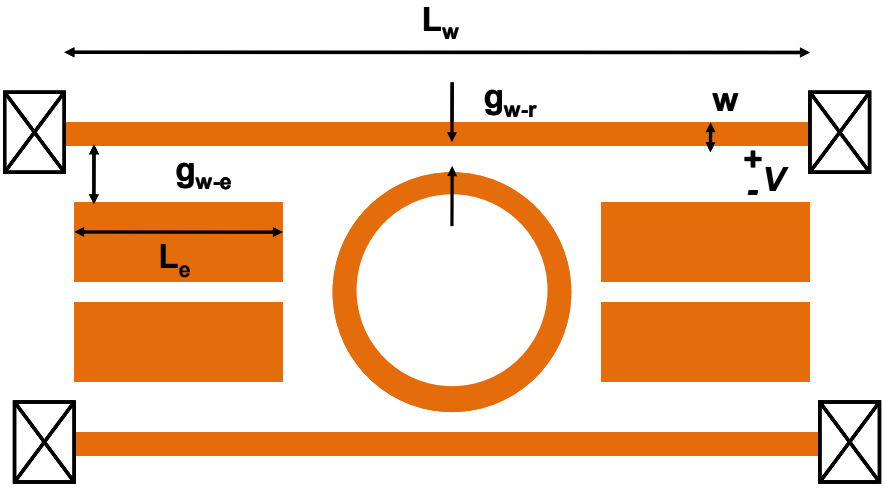

Figure 3.5 Model of a microring resonator with waveguide couplers. L_w: suspended waveguide length, L_e: electrode length, g_{w-r}: gap between the waveguide and the ring resonator, g_{w-e}: gap between the waveguide and the electrode, w: waveguide width, V: applied voltage.

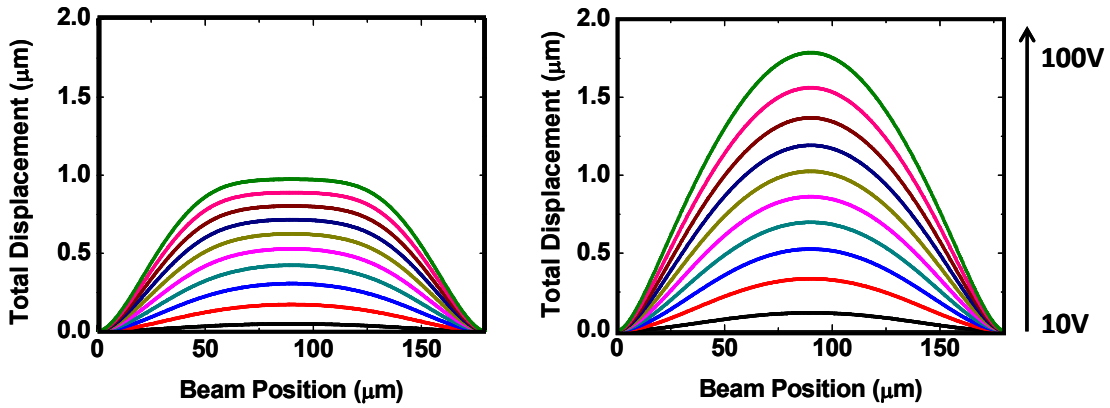

(a) (b)

Figure 3.6 (a) Simulated beam profile without electrostatic forces applying to the middle region of the waveguide under different bias voltages. The suspended beam length is 180 μm and the length of the electrode at each side is 60 μm with

gap spacing of 3.85 μm without bias voltages. (b) Simulated beam profile with continuously distributed electrostatic force over the entire waveguide. The beam length is 180 μm and the gap spacing is 3.85 μm.

3.2.2 Prebent Waveguides

Because of the residual compressive stress in SOI wafers, the fabricated suspended waveguides might have buckling problems if the waveguide is not stiff enough or the residual stress is too large. The relation between the buckling of the suspended waveguides and the compressive strain for a fixed-fixed beam can be expressed as [68]

$$d_{buckle} = \sqrt{\frac{4\varepsilon L_w^2}{\pi^2} - \frac{16I}{wh}} \quad \text{for } L_w > L_c \,, \tag{3.5}$$

where d_{buckle} is the buckling distance at the center of the beam, ε is the strain, and L_c is the Euler critical limit which can be written as,

$$L_c = \sqrt{\frac{\pi^2 w^2}{3\varepsilon}} \,. \tag{3.6}$$

For instance, a single-mode silicon waveguide with dimensions of 350 nm in width and 500 nm in height is fabricated on a typical SOI that has compressive residual stress approximately 13 MPa. As a result, the Euler buckling limit is approximately 70 μm, which is unfortunately too short for our design. The resulting bias voltage is too large for any operations.

For a perfect waveguide, it will be in a bi-stable state when the compressive stress is larger than the Euler critical limit. It may buckle either toward the microring or away from the microring to relax the stress, which causes another problem for our application. If the suspended waveguide buckles toward the microring resonator, but does not touch it,

the device still works well. However, if the waveguide buckles away from the microring resonator, the actuator needs a larger bias voltage to bring the waveguide from an outward stable state to an inward stable state because of a larger gap between the waveguide and the resonator. When the waveguide is pulled to the inward state, the bias voltage is too large (more than the pull-in voltage), and causes the waveguide to get stuck on the microring resonator.

To solve this issue, the waveguide is intentionally bent toward the microring in the layout (Figure 3.7). That creates an imperfection in the waveguide, and the waveguide will tend to buckle in the same direction as the pre-bending with compressive stress. The relation between the buckling distance of the pre-bent waveguide and the compressive strain is [68]

$$d_{buckle}^3 + \left(16\frac{I}{wh} - \frac{4}{\pi^2}L_w^2\varepsilon - d_{bent}^2\right)d_{buckle} - 16\frac{I}{wh}d_{bent} = 0, \tag{3.7}$$

where d_{bent} is the pre-bent distance introduced in the layout and d_{buckle} is the resulting buckling distance in the center of the waveguide. The calculated buckling distance of a 120-μm-length suspended silicon waveguide with a thickness of 500 nm and a width of 350 nm is depicted in Figure 3.8. The trend shows that larger pre-bent waveguides are less sensitive to stress. In other words, we can eliminate stress-induced buckling with sufficiently large pre-bending.

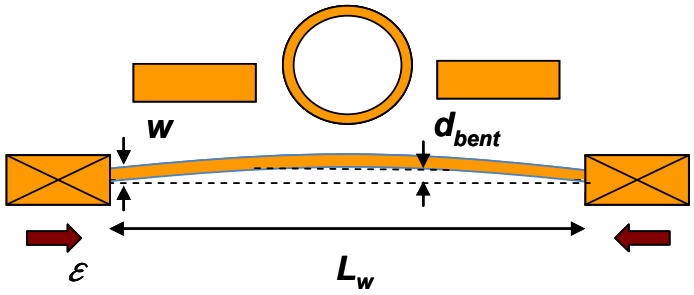

Figure 3.7 Schematics of the pre-bent waveguide design. d_{bent}: the pre-bent distance of the waveguide, w: width of the waveguide, L_w: suspended length of the waveguide, ε: strain due to the compressive stress.

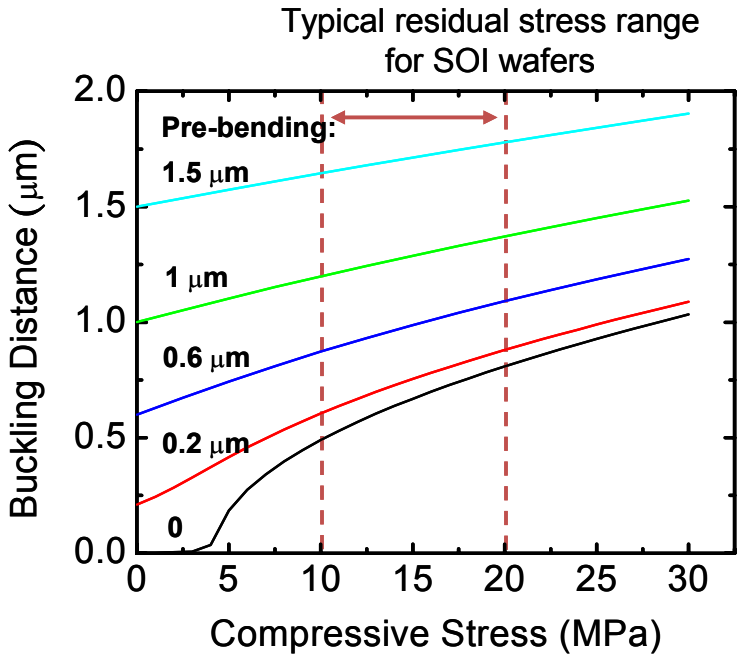

Figure 3.8 Design plot of a 120-μm-length pre-bent waveguide. The buckling distance becomes less sensitive to stress with a larger pre-bent design. The perfect waveguide without any pre-bending is also shown in the plot for comparison which exhibits critical stress of 4 MPa.

3.3 Sidewall Smoothing by Thermal Oxidation

Scattering due to sidewall roughness is a major source of loss in micro-optical resonators. It degrades the Q of the resonator and increases the propagation loss of waveguides. Different material systems have different post-fabrication treatment to

smooth out the roughness due to microfabrication. For instance, laser annealing is utilized to reflow silicon dioxide to form highly smooth microtoroidal resonators [69, 70]. High temperature thermal annealing is used to reflow phosphosilicate glass (PSG) to form a smoother surface [71, 72]. For silicon, hydrogen-assisted thermal annealing [73-75] and thermal oxidation [76-78] are generally used to smooth out the roughness. The mobility of silicon atoms on the structure surface is enhanced by heated hydrogen [79, 80], and thus they can migrate from convex corners to concave corner to reduce the roughness. Using this approach, high-Q tunable microdisk and microtoroidal resonators with MEMS actuators were demonstrated [45, 60]. Similarly, thermal oxidation can reduce the sidewall roughness because the oxidation rate on the convex surface is faster than that on the concave surface [81]. Since thermal oxidation is a common step in standard CMOS processes, we incorporate it into our process for tunable microring resonators to reduce the sidewall roughness. In addition, it can shrink the dimensions of waveguides to support a single optical mode.

Figure 3.9 exhibits the cross-sectional profile of a waveguide before and after wet thermal oxidation using two-dimensional process simulation software, Tsuprem-4. The rough sidewall is smoothed out after a ten-minute wet thermal oxidation at 1050^{o}C because of the different oxidation rates of the convex and concave surfaces. The roughness is then transferred to the oxide surface, which will be removed during release processes.

The dimension of the waveguides and the microring can also be reduced to support a single optical mode by thermal oxidation. Our target dimension of a single-mode silicon

waveguide is 350 nm in width and 500 nm in height. Figure 3.10 shows the dimensions and profiles of the waveguide and the microring resonator before and after thermal oxidation. With proper calibration, the target dimension can be achieved consistently. The corner of the microring became round after thermal oxidation because of slower oxidation on the concave surface.

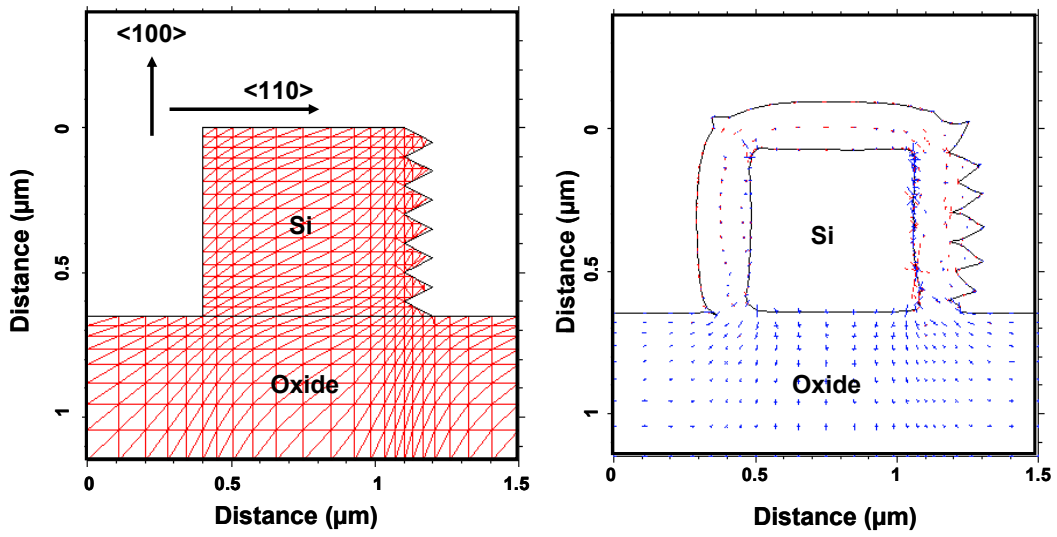

(a) (b)

Figure 3.9 Cross-sectional profiles of a waveguide (a) before and (b) after wet thermal oxidation at 1050°C for 10 minutes using Tsuprem-4.

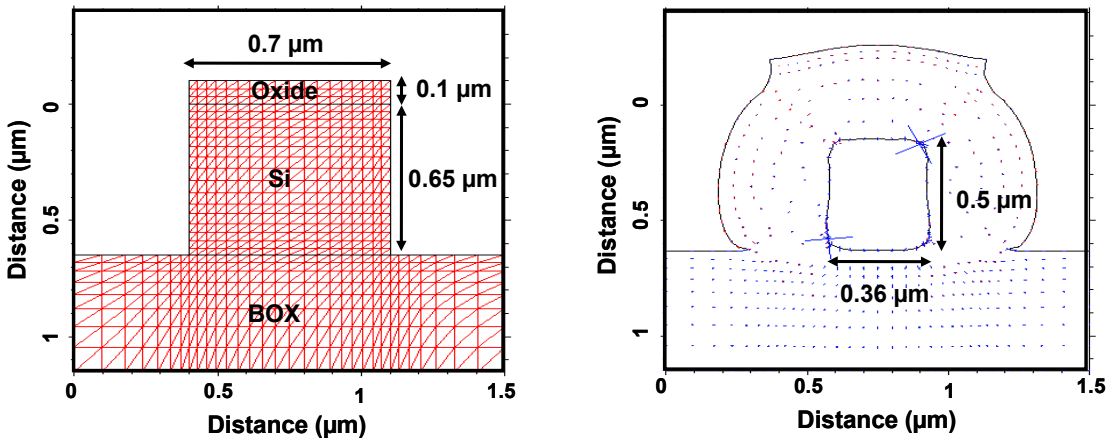

(a) (b)

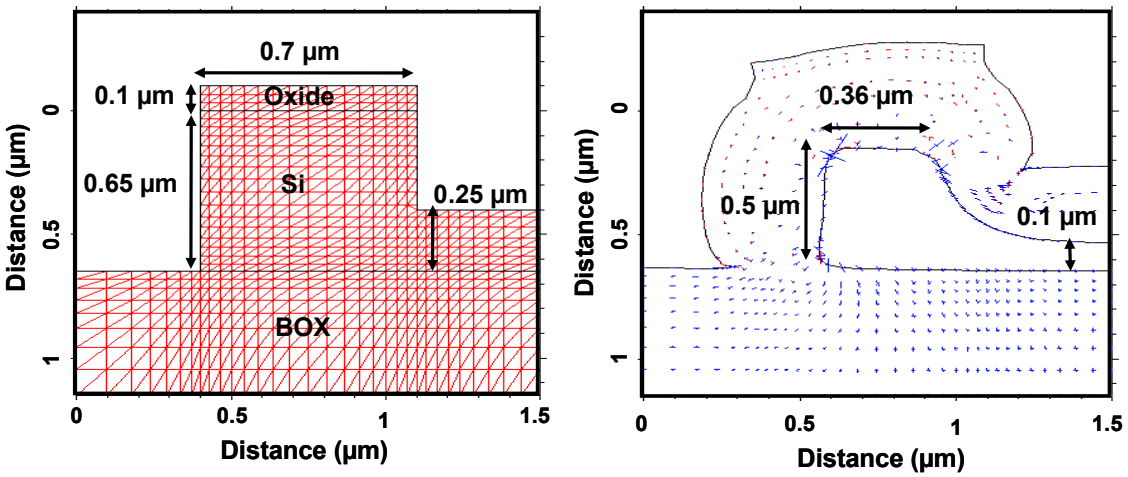

(c) (d)

Figure 3.10 Cross-sectional profiles and dimensions of the waveguide and the microring before and after thermal oxidation. (a) The profile and dimension of the waveguide before oxidation. (b) The profile and dimension of the waveguide after oxidation. (c) The profile and dimension of the microring before oxidation. (d) The profile and dimension of the microring after oxidation.

3.4 Device Fabrication

The integrated device is fabricated on a 150 mm SOI wafer with 0.8 μm silicon device layer and 3 μm buried oxide (BOX) layer from Soitec. The fabrication includes a two-step etching process and thermal oxidation, followed by the release of the waveguides and actuators (Figure 3.11). It starts with a partial etch of silicon microring resonators, waveguides, and electrostatic actuators using thermal oxide as a hardmask (Figure 3.11(a)). A silicon device layer of 250 nm is preserved as an anchor for the microring resonator. With protection of the inner microring using photoresist, the outer microring, waveguides, and actuators continue to be etched down to the BOX layer (Figure 3.11(b)). Thermal oxidation is then utilized to smooth out the sidewall roughness due to microfabrication and reduce the dimensions of the waveguide (Figure 3.11(c)). After oxidation, the thickness of the remaining silicon layer in the inner microring is

approximately 100 nm, as shown in Figure 3.10(d), which is sufficiently thin to cut off higher radial modes. Finally, the electrostatic actuators and waveguides are released in buffered oxide etchant (BOE) followed by super-critical drying to avoid stiction (Figure 3.11(d)). The remaining silicon in the inner microring prevents it from being released. All processes are CMOS compatible using deep-UV photolithography.

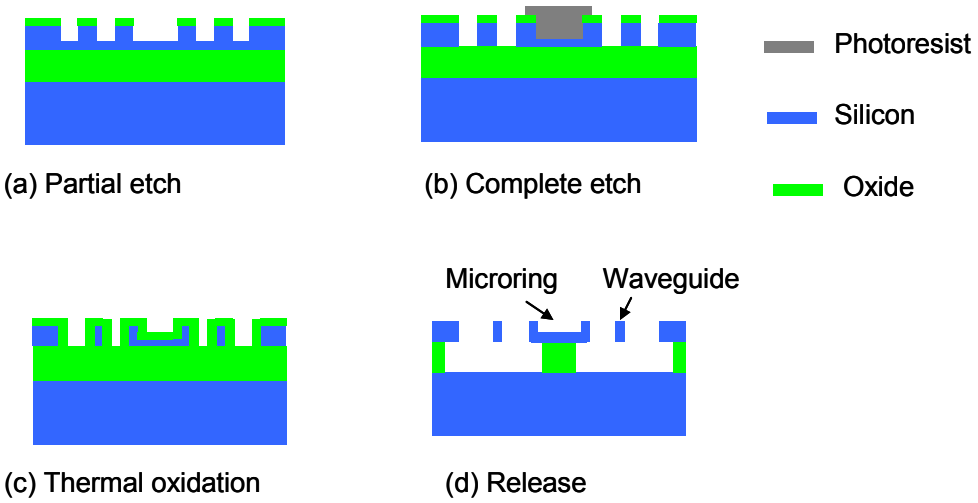

Figure 3.11 Fabrication process flow of tunable microring resonators with integrated MEMS actuators. (a) Partial etch of microring resonators, waveguides, and actuators. (b) Compete etch of waveguides, actuators, and outer microrings. Inner microrings are protected by photoresist to preserve the silicon underneath. (c) Thermal oxidation to reduce the sidewall roughness. (d) The devices are released in BOE by etching oxide, followed by super-critical drying.

The scanning electron microscope (SEM) image of a fabricated tunable microring resonator with an integrated MEMS actuator is shown in Figure 3.12(a), which consists of a microring resonator, two suspended waveguides, and MEMS electrostatic actuators. By applying proper bias voltages to the electrodes, the gap spacing between the microring and the waveguides can be continuously varied, and thus the power coupling ratio is adjusted by MEMS actuators. As shown in Figure 3.12(b), the silicon waveguide is surrounded by SiO_2 before release. The fabricated silicon waveguide dimensions are 220

nm wide by 500 nm high, which satisfies the single mode condition. Figure 3.12(c) displays the smooth sidewall of the microring resonator with thermal oxidation treatment to reduce the roughness, which is a key step to reach a high-Q resonator.

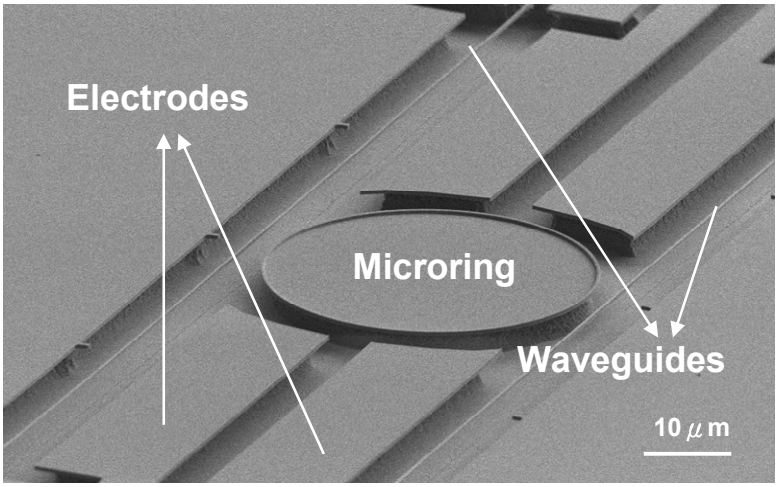

(a)

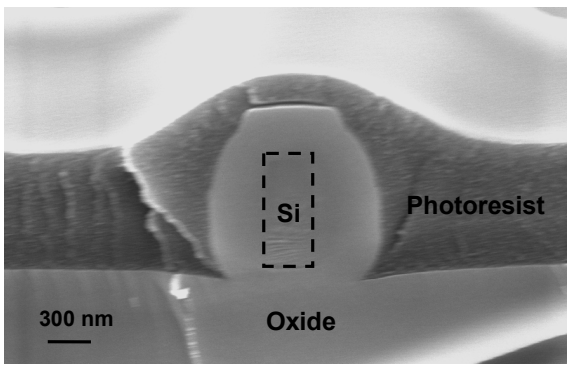

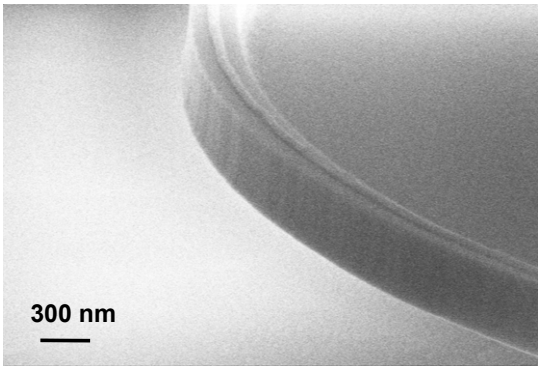

(b) (c)

Figure 3.12 (a) Fabricated tunable microring resonators with integrated MEMS actuators and suspended waveguides. (b) Cross-sectional view of the silicon waveguide surrounded by thermal oxide. The top photoresist is used to define a release window for BOE etching. (c) Close-up view of the sidewall of the microring resonator.

3.5 Characterization of Tunable Microring Resonators

The transmission spectra of the tunable microring resonator are measured using an Agilent 81680A tunable laser and an Agilent 81340B power meter, which are synchronized to provide fast and high-resolution (1 pm) wavelength sweeping measurements (Figure 3.13). The laser power is coupled into the silicon waveguide through a polarization maintaining lensed fiber, and another single mode lensed fiber collects the transmitted light. By applying a bias to the electrodes of the MEMS actuators through DC probes, the integrated silicon waveguides are actuated and thus the gap spacing between the waveguide and the microring resonator is systematically varied.

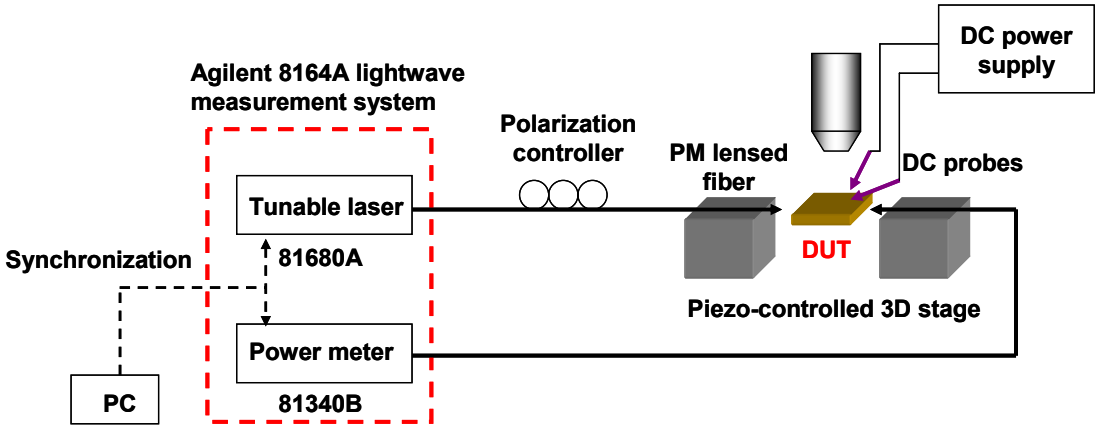

Figure 3.13 Experiment setup for characterization of tunable microring resonators. A synchronized tunable laser and a power meter are used as an optical source and detector for spectrum measurement. The lensed fibers attached on the piezo-controlled 3D stage are used to couple the light in and out of the on-chip silicon waveguides. Bias voltages are applied to MEMS actuators via DC probes.

To characterize the tunable microring resonator, only one waveguide is actuated while the other parallel waveguide is decoupled from the microring resonator. In this case, the device behaves as an optical notch filter, and the measured transmission spectra are shown in Figure 3.14. The suspended waveguide length of the device is 180 μm and the

electrode length is 60 μm. The gap between the waveguide and the microring resonator is 1.15 μm while that between the waveguide and the electrodes is 3.85μm. By applying different voltages to the MEMS actuators, the resonator can be operated in the under-coupled or over-coupled regime. In the under-coupled regime, a double resonance dip (doublet) caused by backscattering in the resonator is observed. The clockwise and counterclockwise propagating modes couple to each other via backscattering, which lifts the degeneracy and splits the resonance dip. However, in the over-coupled regime, the doublet is not observable, as shown in Figure 3.14 at a bias of 71 V.

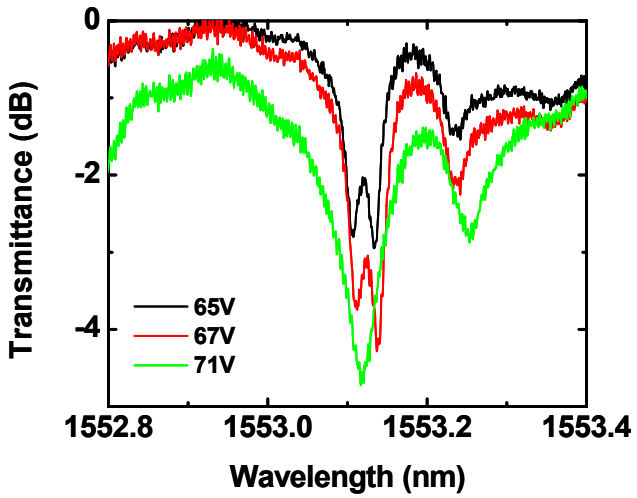

Figure 3.14 Measured transmission spectra of tunable microring resonators with different bias voltages. At 65 V or 67 V, the resonator operated in the under-coupled regime, and a doublet is observed due to the backscattering in the resonator. When the bias was increased to 71 V, the resonator operated in the over-coupled regime, and the doublet was not observable anymore.

As described in Chapter 2, the transmission spectrum is determined by the power coupling ratio between the waveguide and the resonator (κ), the optical round-trip loss in the resonator (γ), the backscattering power ratio (β), and the reflection at the waveguide

facets (r). The coupling gap between the waveguide and the resonator varies with the bias voltages, and thus so does the power coupling ratio. By fitting a family of transmission spectra at different bias voltages with these variables, the Q of the resonator can be extracted. Figure 3.15 shows a family of measured and fitted transmission spectra of the resonator. The fitting parameters of optical round-trip loss, backscattering in the resonator, and reflection at the waveguide facet are constant, while the power coupling varies with bias voltages. An intrinsic Q of the microring resonator is extracted approximately 88,400, and a loaded Q can be tuned from 16,300 to 88,400.

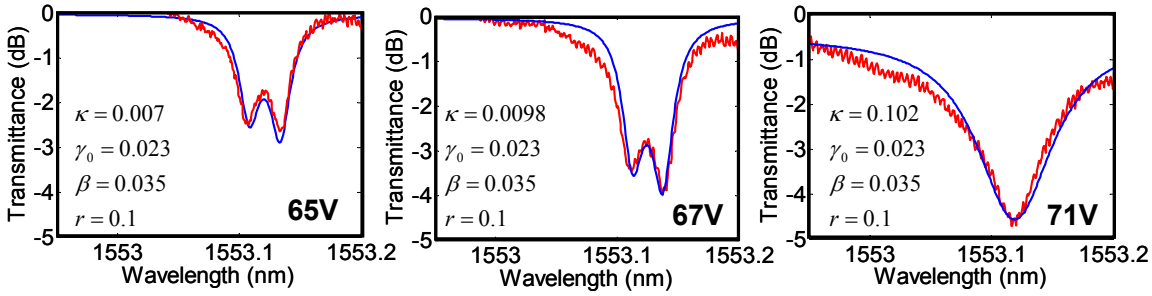

Figure 3.15 A family of measured and fitted transmission spectra of the microring resonator at different bias voltages. The extracted intrinsic Q of the resonator is approximately 88,400 while the loaded Q can be tuned from 16,300 to 88,400.

3.6 Applications of Tunable Microring Resonators

There are several applications for tunable microring resonators with integrated waveguides. Here we demonstrate two applications, ON-OFF wavelength switches and tunable optical add-drop filters based on single- and two-waveguide configurations.

3.6.1 ON-OFF Wavelength Switches

An ON-OFF wavelength switch can be realized by a microring optical resonator with an integrated waveguide and MEMS actuators that control the power coupling ratio

between the resonator and the waveguide (Figure 3.16). Without any bias, the waveguide is decoupled from the microring resonator since the original position of the waveguide is far from the resonator. Therefore, input optical waves with all wavelengths can pass through to the output end. When a bias voltage is applied to the actuator, the waveguide is pulled toward the microring resonator, and the light starts to couple into the microring resonator. The light whose wavelength matches the resonance wavelength is coupled and stored in the resonator, and thus resonance dips are observed in the output spectrum. As shown in Figure 3.17, the optical switch exhibits an extinction ratio of 20 dB, an optical bandwidth of 10 GHz, and a resonance wavelength of 1553.9 nm. The ON-OFF wavelength can also be used for secure communications.

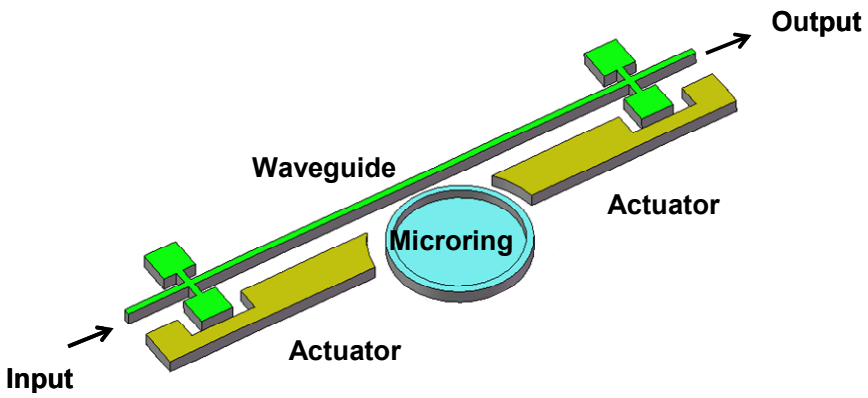

Figure 3.16 Schematic of an ON-OFF wavelength switch based on a microring resonator, an integrated silicon waveguide, and MEMS actuators.

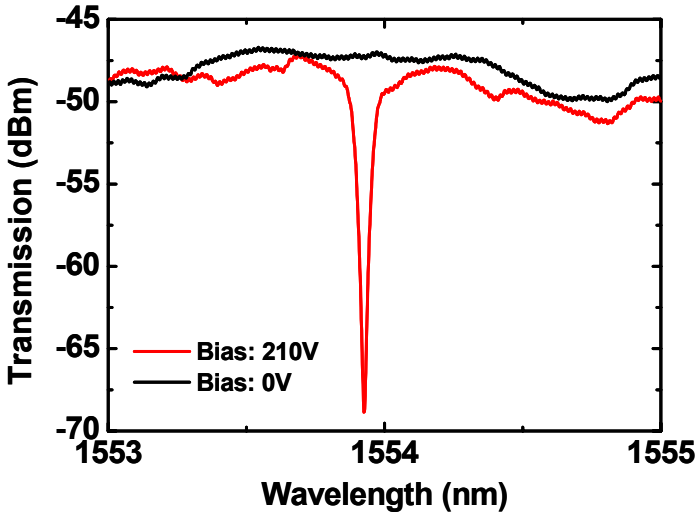

Figure 3.17 Transmission spectrum of an ON-OFF wavelength switch based on a tunable microring resonator. The extinction ratio and the bandwidth of the switch are 20 dB and 10 GHz, respectively. The specifications of the device used for the switch are as follows: suspended waveguide length: 180 μm, electrode length: 60 μm, initial gap spacing between the waveguide and the resonator: 2.25μm, the gap between the waveguide and the electrodes: 5.35 μm.

3.6.2 Tunable Optical Add-drop Filters

To satisfy the increasing demand for network bandwidth, the deployment of optical networks is moving increasingly closer to the end-user's premises. Since cost is a major issue in optical access networks, a low-cost optical filtering function is desirable. Integrated optical add-drop filters are the key components to realize this function. They can be implemented using arrayed waveguide gratings (AWGs) or MZIs. Since AWGs can only split the wavelengths, additional components such as switches are required for optical add-drop multiplexers (OADM). MZI-based OADMs usually require multiple MZIs for the selection of a single channel. Microrings are viable candidates to realize OADM because they have very small footprints and require a minimal number of components for implementation.

A tunable optical add-drop filter consists of a microring resonator, two integrated waveguides, and MEMS actuators to control the gap spacing between the resonator and the waveguides (Figure 3.18). With appropriate coupling between the microring resonator and the waveguides, the light with the wavelength that matches the resonance wavelength is coupled from the input waveguide to the microring, and then to the drop port. Non-resonance wavelengths pass to the through port. The measured transmission spectra at the through and drop ports are depicted in Figure 3.19. The resonance wavelength and optical bandwidth are approximately 1553.75 nm and 10 GHz, respectively.

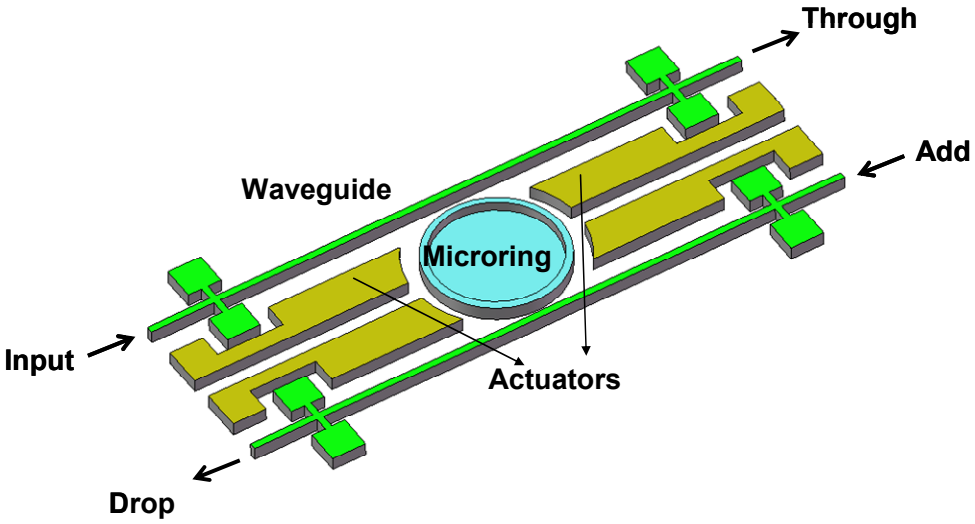

Figure 3.18 Schematic of a tunable add-drop filter based on a microring resonator with integrated silicon waveguides and MEMS actuators.

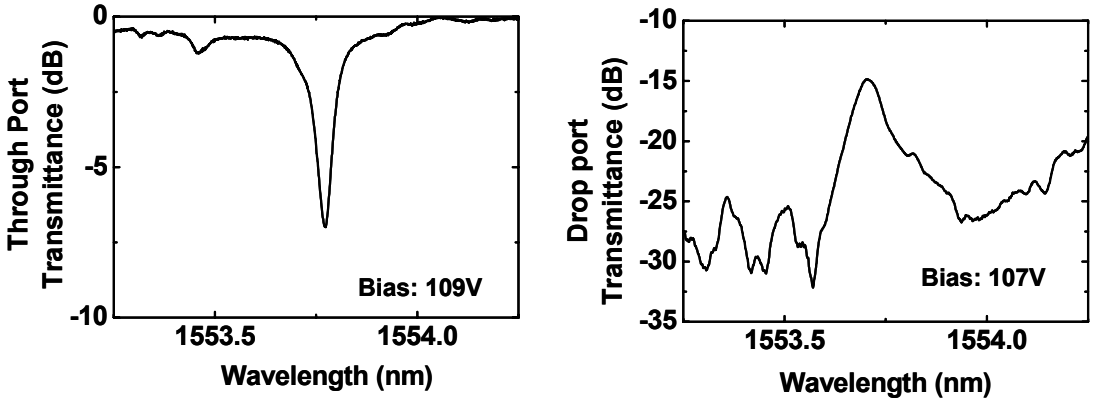

(a) (b)

Figure 3.19 Measured transmission spectra at the (a) through port and (b) drop port. The specifications of the device are as follows: suspended waveguide length: 140 μm, electrode length: 40 μm, initial gap spacing between the waveguide and the resonator: 1.15μm, the gap between the waveguide and the electrodes: 3.85 μm.

3.7 Summary

In this chapter, we review tuning mechanisms of microresonators, including resonance wavelength tuning, cavity loss tuning, and power coupling ratio tuning. We use MEMS electrostatic actuators to change waveguide-resonator spacing, which in turn changed the power coupling ratio. The advantages of this approach include a small footprint and low power consumption. We also describe the design and fabrication problems, including the pull-in effect of the electrostatic actuators, buckling and stiction of suspended waveguides, and sidewall roughness resulting from the etching process. Solutions in the design and fabrication aspects are proposed to solve these problems and make the device feasible.

Experimentally, we have demonstrated laterally-coupled microring resonators with integrated silicon waveguides and MEMS actuators using CMOS-compatible fabrication

processes. The intrinsic Q of the microring resonator is 88,400, and the loaded Q can be tuned from 16,300 to 88,400. This device has potential applications in bandwidth-tunable filters, reconfigurable optical add-drop multiplexers, wavelength-selective switches and crossconnects, and optical sensors. In this chapter, we demonstrate the feasibility of ON-OFF wavelength switches and tunable optical add-drop filters.

Chapter 4 Microdisk Lasers

Microdisk lasers attract a lot of attention as light sources for on-chip optical interconnects in CMOS photonics because of the advantages of a low threshold, small footprint, and low power consumption. Because of the large refractive index contrast, microdisk lasers also provide better vertical optical confinement and thus a lower threshold. In addition, thin microdisk lasers can provide effective coupling of the power to the integrated optical waveguides because of larger overlap of the optical modes between the microdisk lasers and waveguides. This chapter discusses the theoretical modeling and design trade-offs of microdisk lasers.

4.1 Review of Microdisk Lasers

Microdisks can support whispering-gallery modes (WGMs) as optical resonators Figure 4.1 illustrates a typical mode profile of microdisk resonators with air cladding. The microdisk has a 1.5 μm radius and 253 nm of thickness. The effective index of the

microdisk is 2.8. The large refractive index contrast provides good optical confinement in the vertical direction. In the radial direction, the optical field tends to move close to the edge of the disk. Figure 4.1(d) shows the optical field distribution in the x-y plane of the microdisk.

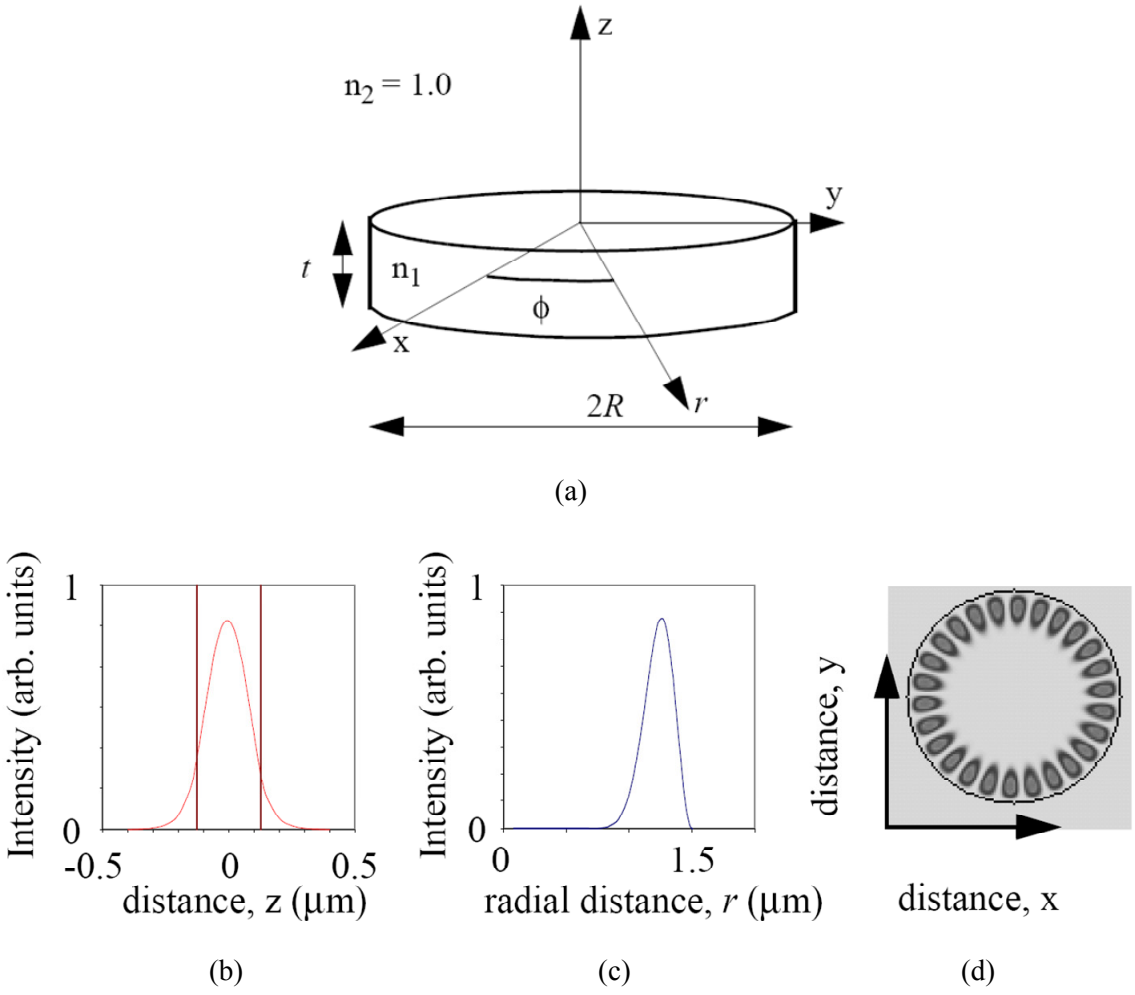

Figure 4.1 (a) Illustration of a microdisk resonator. The radius and the thickness of the microdisk are 1.5 μm and 253 nm, respectively. (b) Optical field distribution in the vertical direction of a microdisk. The boundaries of the microdisk at z = t/2 and z = -t/2 are marked. (c) Optical field distribution along the radial direction. (d) Optical mode profile in the x-y plane of the microdisk [82].

III-V materials further provide the required optical gain for a microdisk laser. S. L. McCall first demonstrated microdisk lasers in InGaAs/InGaAsP MQW material systems using optical pulse pumping at low temperatures in 1992 [83]. The microdisk laser was supported on an InP pedestal by undercutting the InP layer. Room-temperature electrically-pumped microdisk lasers were also demonstrated under pulsed condition by Levi in the same research group [84]. A double-disk structure was used to reduce contact resistance and inject current in the microdisk laser. Room-temperature continuous-wave (CW) microdisk lasers were successfully demonstrated by reducing etched disk sidewall roughness and improving heat sink design [85, 86]. In addition to these standalone lasers, microdisk lasers with integrated waveguides on InP substrate were reported [87]. Microdisk lasers on silicon platforms also attract a lot of attention because they are compatible with CMOS processes [88-90]. This dissertation focuses on the integration of III-V microdisk lasers with silicon photonic circuits. The design of microdisk lasers with integrated waveguides is explained in the following sections of this chapter.

4.2 Microdisk Laser Resonances

A typical semiconductor laser is composed of active media and a cavity (resonator) that provide the required optical gain and feedback, respectively. Here, we embed semiconductor MQW layers in microdisk resonators. At the threshold, the optical loss is compensated by gain. In other words, the optical round-trip gain is equal to one:

$$e^{\Gamma_{QW} G - \alpha_{tot}} = 1 \ , \tag{4.1}$$

where Γ_{QW} is the optical confinement factor of quantum wells, G is the optical gain coefficient of the quantum wells, and α_{tot} is the total optical loss. In addition, the round-

trip cavity length is equal to the integral multiple of the wavelength. The condition can be written as

$$2\pi R = m\frac{\lambda}{n_e}\ , \tag{4.2}$$

where n_e is the effective index of WGM in the microdisk, λ is the free space laser wavelength, and m is an integer. The resonance mode spacing $\Delta\lambda$ is derived as

$$\Delta\lambda = \frac{\lambda^2}{2\pi R n_g}\ , \tag{4.3}$$

where n_g is the group index of WGM in the microdisk.

For quantum-well lasers, the gain coefficient is well approximated by a logarithmic function of the carrier density [91]:

$$G(N) = G_0 \ln\left(\frac{N}{N_0}\right)\ , \tag{4.4}$$

where G_0 is the gain parameter and N_0 is the transparency carrier density. In an InP-based quantum-well system, typical values are $G_0 = 1500$ cm^{-1} and $N_0 = 2.2\times10^{18}$ cm^{-3} [92].

4.3 Optical Losses in Microdisk Lasers

4.3.1 Intrinsic Loss

Intrinsic loss in a semiconductor, which is also called material loss, is contributed by (1) interband absorption, (2) intraband free-carrier absorption (FCA), and (3) free-carrier absorption between different conduction bands [93]. All absorption is a function of photo

energy (Figure 4.2). For a microdisk laser operating above the threshold, the major intrinsic loss is due to free-carrier absorption, which can be described by

$$\alpha_{FCA} = k_p p + k_n n \ , \tag{4.5}$$

where p and n are hole and electron concentrations, while k_p and k_n are loss coefficients. For bulk InGaAsP, $k_p = 40 \times 10^{-18} cm^2$ and $k_n = 10^{-18} cm^2$, respectively [94].

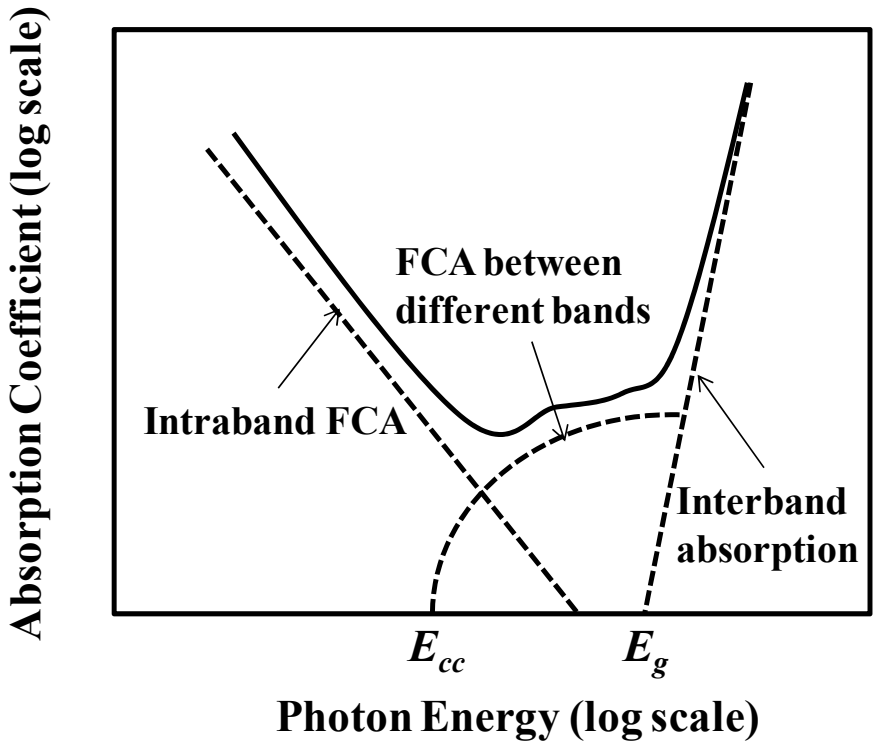

Figure 4.2 Schematic of the absorption coefficient versus photon energy. It can be divided into three regimes. When photon energy is larger than the bandgap, interband absorption dominates. When photon energy is smaller than, but close to, the bandgap, FCA between different conduction bands dominates. For photon energy much smaller than the bandgap, intraband FCA is the major loss mechanism.

4.3.2 Scattering Loss

Scattering loss of microdisk resonators is mainly from the surface roughness caused by fabrication processes. It can be modeled using the volume-current method [36, 95] assuming the scattering is only caused by the disk edge roughness, and the top and bottom surfaces of the disk are perfect. The scattering loss can be written as [92]

$$\alpha_s = \frac{1}{2\pi R}\frac{P_s}{P_g} = \frac{16\pi^3}{3R}\left(1-\frac{n_0^2}{n_e^2}\right)^2\left(\frac{n_e\sigma}{\lambda}\right)^2\frac{n_e L_c}{\lambda}\Gamma_z\frac{t}{\lambda}\ , \tag{4.6}$$

where P_g is the power in the guided mode, P_s is the scattered power on the disk edge, R is the disk radius, n_0 is the refractive index of the surrounding medium, n_e is the effective index of the disk region, σ is the root mean square (rms-value) of the edge roughness, L_c is the correlation length of the edge roughness, Γ_z is the vertical disk confinement factor, t is the disk thickness, and λ is the free-space optical wavelength. The scattering loss depends on several parameters. It is proportional to the ratio of the scattered power to total guided power. Figure 4.3 shows the scattering loss versus disk thickness and radius with different rms-values of roughness. It is approximately inversely proportional to the disk radius and linearly proportional to the disk thickness. Optimal microdisk design for minimal roughness-induced scattering loss is discussed in Section 4.4.

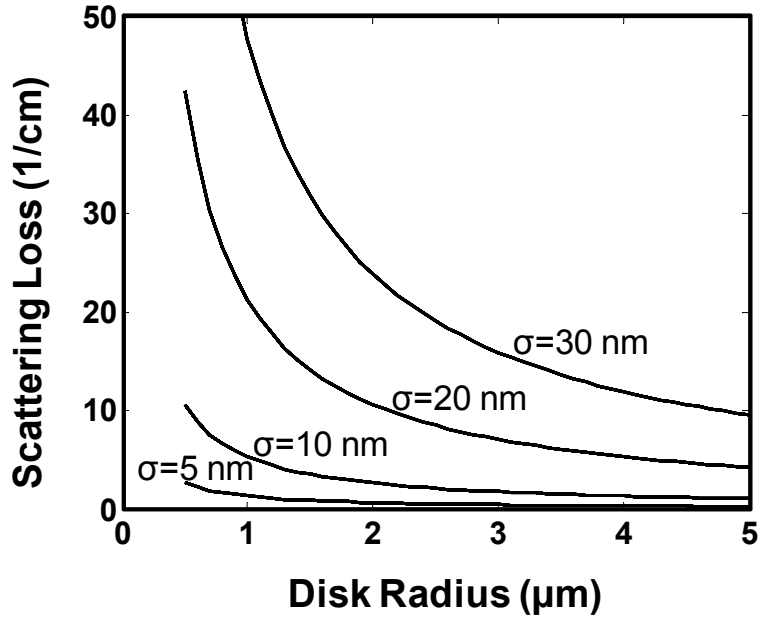

(a)

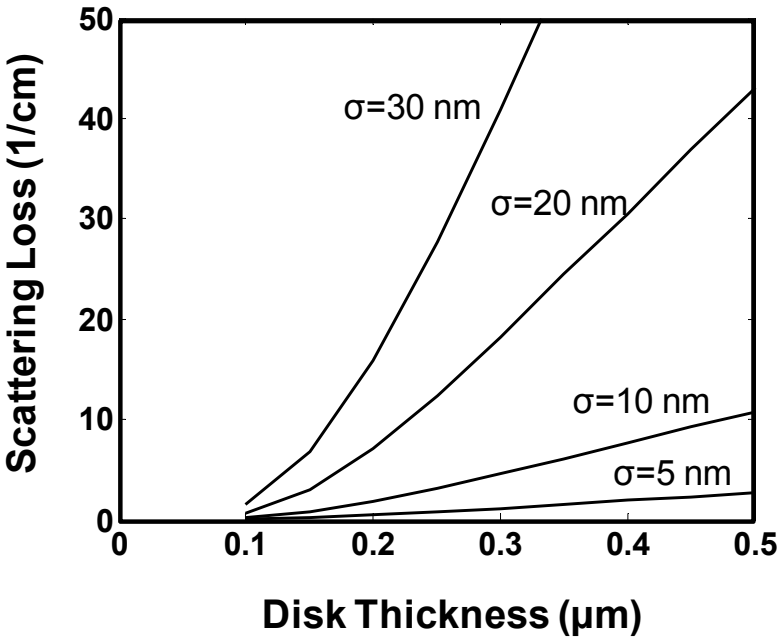

(b)

Figure 4.3 Calculated scattering loss of microdisk lasers. (a) Scattering loss versus radius for different rms-values of the roughness. Disk thickness is assumed to be 200 nm. (b) Scattering loss versus disk thickness for different rms-values of the roughness. Disk radius is assumed to be 3 μm. The roughness correlation length L_c is assumed to be 100 nm for both figures.

4.3.3 Bending Loss

When light propagates in a curved waveguide, the mode profile is shifted toward the outer edge. This results in radiation via tunneling from the azimuthally guided modes. Such radiation loss is often referred to as bending loss. Strictly speaking, all WGMs are "leaky" due to bending loss, which can be approximately expressed as [96]

$$\alpha_b = K \exp\left(-\beta \left(\frac{2\Delta n_e}{n_e} \right)^{3/2} R \right), \tag{4.7}$$

where β is the propagation constant, Δn_e is the effective index difference between the disk and the surrounding medium, and K is a constant depending on the refractive indices of the disk and the surrounding medium and on disk thickness. The bending loss is exponentially dependent on the disk radius. Figure 4.4 plots the bending loss and the corresponding Q versus radius for TM-polarized WGM in 200-nm-thick microdisk resonators with air and SiO_2 cladding. The bending loss is strongly dependent on the effective index difference between the disk and the surrounding medium. For a 200-nm-thick and 5-μm-radius microdisk, the bending loss is eight orders larger with SiO_2 cladding than air cladding. In our designed microdisk lasers, the surrounding medium is air, and the bending loss can be neglected ($\alpha_b < 0.01 cm^{-1}$) when the radius is larger than 2 μm.

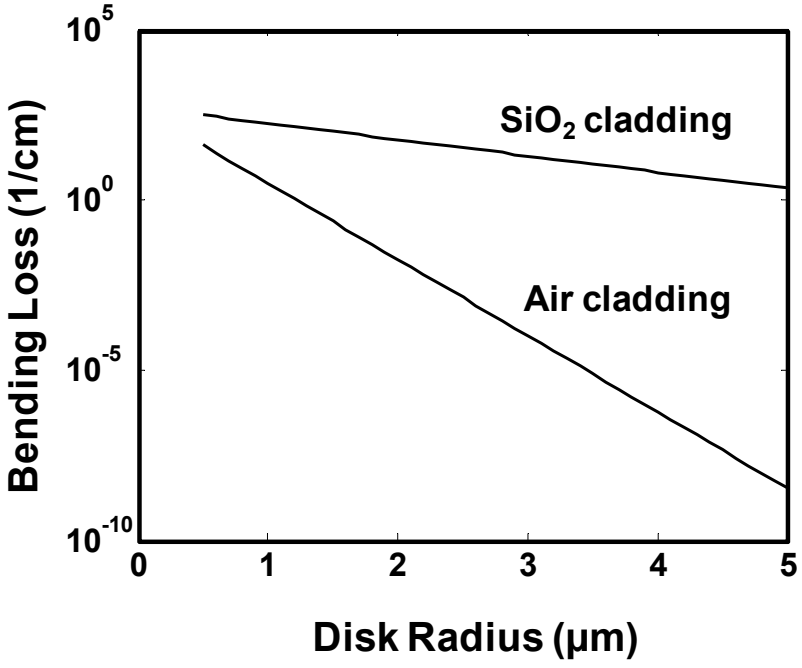

(a)

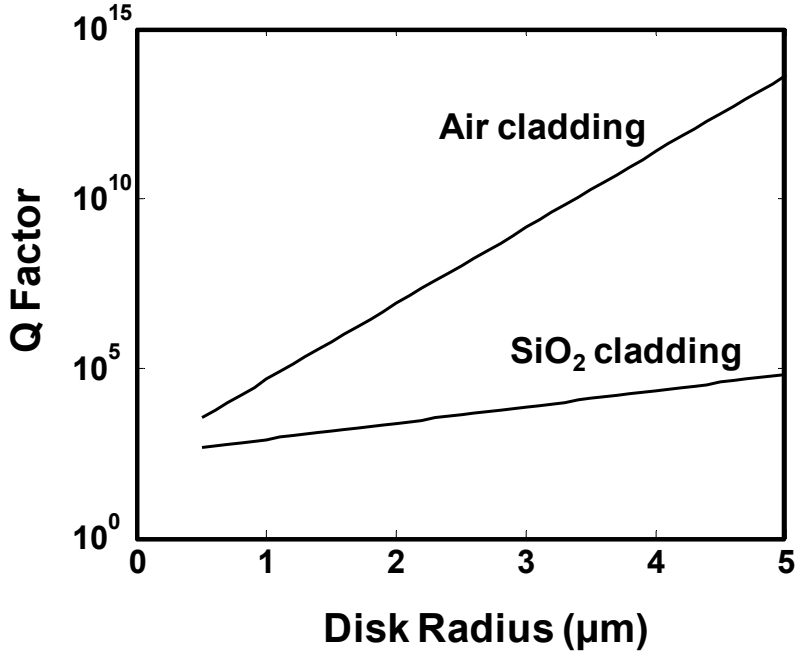

(b)

Figure 4.4 (a) Bending loss versus disk radius for TM-polarized WGM in 200-nm-thick InGaAsP microdisk resonators with air and SiO2 cladding. (b) The bending loss limited Q versus disk radius.

4.3.4 Output Coupling Loss

For waveguide integrated microdisk lasers, as shown in Figure 4.5, the coupling loss from the microdisk to the output waveguide is a "useful" loss whose energy is attracted as output power. Larger coupling leads to higher differential quantum efficiency, but it also increases the laser threshold. Therefore, there is a trade-off between the differential quantum efficiency and the laser threshold. The numerical calculation of the coupling between the disk and the waveguide is performed using commercial finite-difference-time-domain (FDTD) software (Lumerical Solutions). A three-dimensional FDTD calculation result of the coupling from a microdisk to a waveguide with silicon oxide as a spacer is shown in Figure 4.6. The microdisk is 3 μm in radius and 250 nm in thickness, while the waveguide is 500 nm wide and 250 nm thick. The coupling is normalized to the circumference and the effective distributed coupling loss is used here for comparison with the other losses.

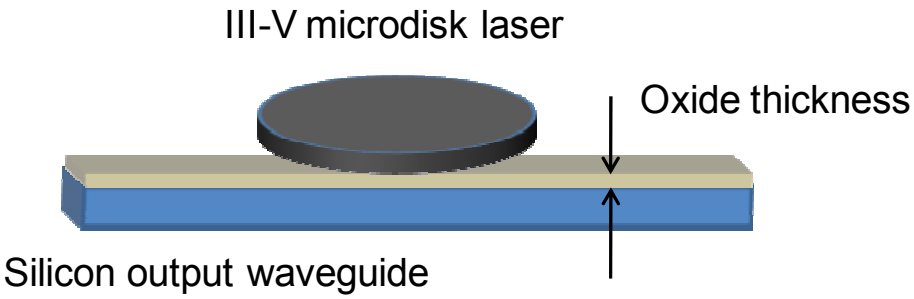

Figure 4.5 Schematic of a waveguide-integrated microdisk laser. The laser power is evanescently coupled to the silicon output waveguide with the coupling determined by the oxide thickness.

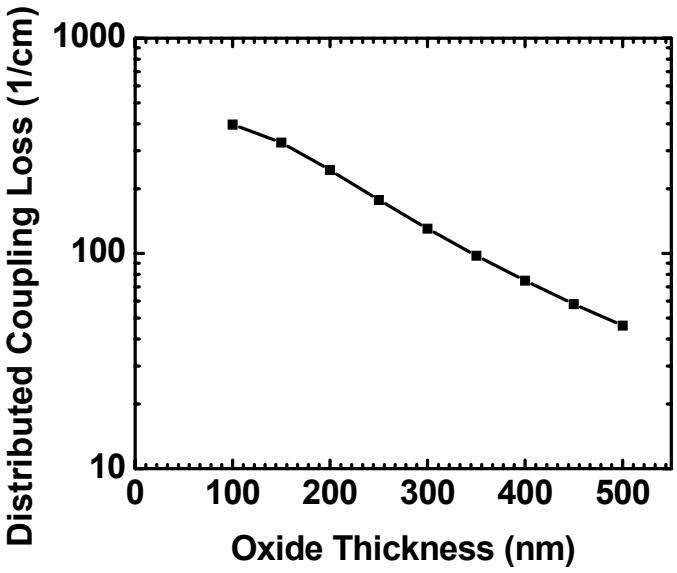

Figure 4.6 Distributed coupling loss for a 3-μm-radius and 250-nm-thick microdisk laser. The silicon waveguide is 500 nm wide and 250 nm thick. The gap between the disk and the waveguide is determined by the oxide thickness, ranging from 100 nm to 500 nm.

4.4 Design of Microdisk Lasers with Integrated Waveguides

Microdisk lasers offer the advantages of a small footprint, easier integration for EOIC, and better optical confinement in the active region because of a larger refractive index contrast. An InP-based semiconductor laser with a lasing wavelength in the 1550 nm regime can be used as a light source for silicon photonic circuits since silicon optical waveguides are transparent in this wavelength regime. In this section, the optimization of microdisk lasers for high differential quantum efficiency and low threshold power is discussed. The device parameters include disk thickness, radius, and the coupling gap between the disk and the output waveguide.

4.4.1 Optical Confinement

Optical confinement in the gain region is determined by the disk thickness and the refractive index contrast between the disk and the surrounding mdeium. In our design, InGaAsP/InGaAs MQWs are used as gain media while larger-bandgap (lower refractive index) InGaAsP layers are used as optical confinement layers. Table 4.1 describes the details of the layer structure for our calculations. We fix the thickness of the gain medium (100 nm) and vary that of the optical confinement layers. Figure 4.7 plots the calculation results by Beam Propagation Method (BPM) using commercial software, Rsoft BeamProp. The confinement factor per quantum well is maximized with a disk thickness of 150 nm, and the corresponding vertical disk confinement is about 0.6. When the disk is too thin (< 150 nm in our design), the optical field can't be completely confined in the disk, and more power leaks to the air, resulting in a lower confinement factor per quantum well.

Layer	Refractive index	Thickness	Function
1.1-μm-bandgap InGaAsP	3.26	Variable (0 ~ 200 nm)	Optical confinement layer
InGaAsP/InGaAs MQWs	3.4	100 nm	MQWs as gain media
1.1-μm-bandgap InGaAsP	3.26	Variable (0 ~ 200nm)	Optical confinement layer

Table 4.1 Layer structure used for optical confinement factor calculations. The thickness of the gain medium is fixed while that of the optical confinement layers varies from 0 to 200 nm.

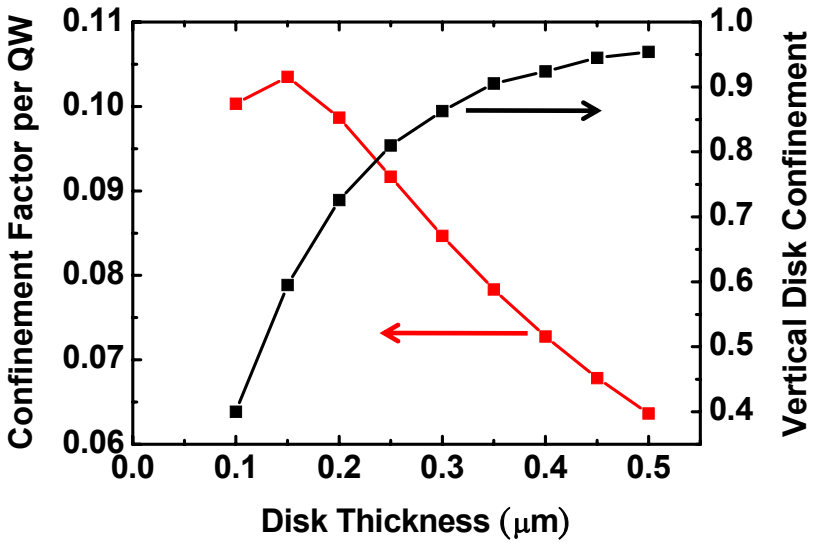

Figure 4.7 Calculated optical confinement factors versus disk thicknesses. The confinement factor per quantum well is shown in the left *y* axis, while the vertical disk confinement is shown in the right *y* axis.

4.4.2 Optimization of Cavity Loss

As described in Section 4.3, microdisk laser cavity loss consists of semiconductor intrinsic loss, scattering loss, and bending loss. These losses need to be minimized in order to reduce the required gain for lasing conditions. The cavity loss is described as [92]

$$\alpha_{cavity} = \alpha_s + \alpha_b + f(R)\alpha_{\text{int}} \ , \tag{4.8}$$

where *f(R)* is a normalization factor that transforms the local intrinsic loss to a modal loss defined with respect to the disk circumference, as are other loss contributions. *f(R)* is calculated as [92]

$$f(R) = \int_0^R H_z^2(r)\frac{r}{R}2\pi r dr \ , \tag{4.9}$$

with $H_z^2(r)$ the radial laser mode profile. The formulas for scattering loss and bending loss are described in Equation (4.6) and (4.7), respectively. The intrinsic loss can be described as

$$\alpha_{\text{int}} = \Gamma_{QW}\alpha_{QW} + \Gamma_{OCL}\alpha_{OCL} \ , \tag{4.10}$$

where Γ_{QW} is the confinement factor of the quantum wells, Γ_{OCL} is the confinement factor of optical confinement layers, and α_{QW} and α_{OCL} are the loss coefficients in quantum wells and optical confinement layers, respectively. For InP-based MQW lasers, α_{QW} and α_{OCL} are approximately 100 cm^{-1} and 4 cm^{-1}, respectively [97].

The calculated cavity loss of microdisk lasers versus disk radius and thickness is shown in Figure 4.8. The scattering loss is inversely proportional to the radius, and approximately linearly proportional to the disk thickness. Bending loss is determined by the radius, and it becomes influential when the radius is smaller than 2 μm. Intrinsic loss is determined by the confinement factors of quantum wells and optical confinement layers, and thus slightly changes with disk thickness but not with disk radius. Figure 4.8 shows that scattering loss is the major loss that is dependent on the radius and thickness when the radius is larger than 1 μm. The bending loss becomes dominant when the radius is smaller than 1μm. The total cavity loss increases with the disk thickness, but decreases with the disk radius.

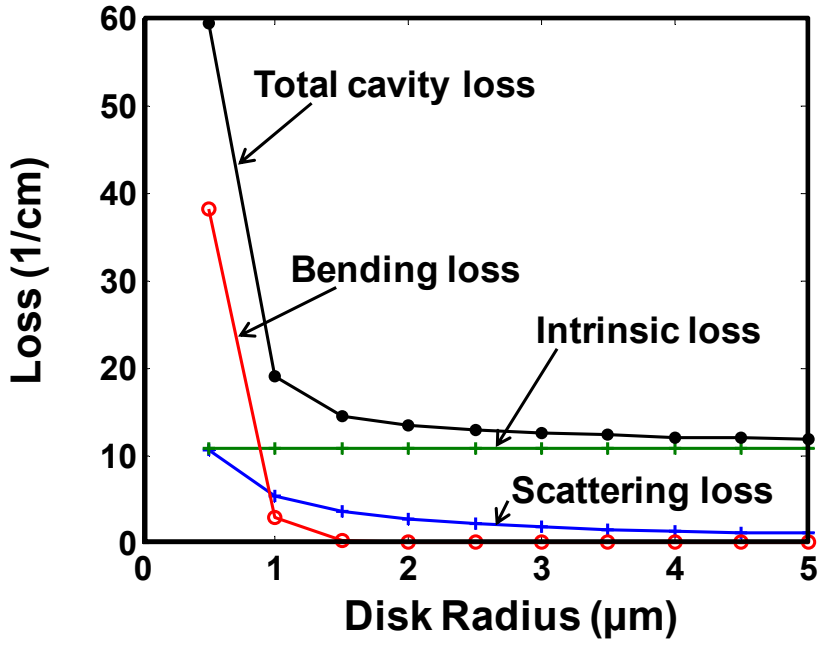

(a)

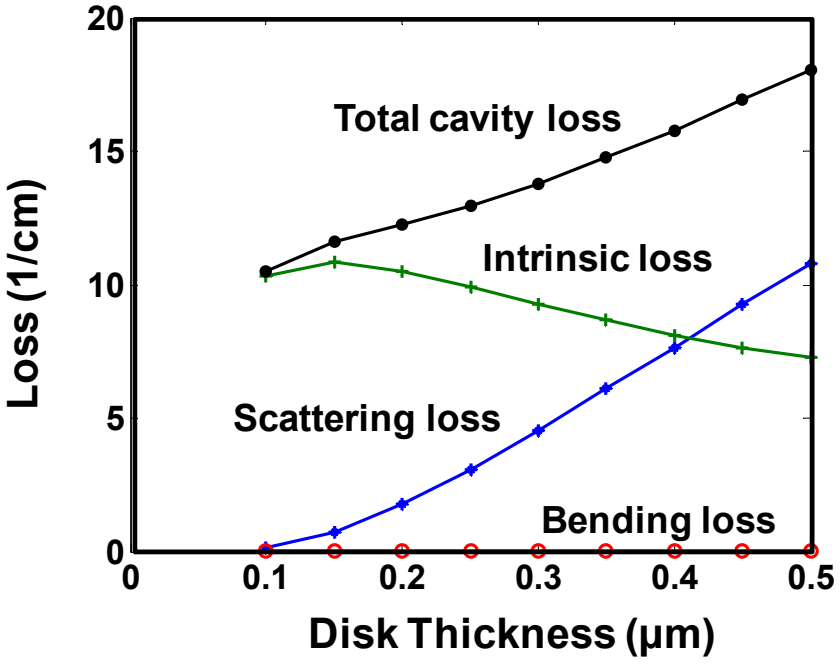

(b)

Figure 4.8 Breakdown of the cavity loss contributed by scattering loss, bending loss, and scattering loss versus (a) disk radius and (b) disk thickness.

4.4.3 Laser Threshold

From Equation (4.1) and (4.4), the threshold carrier density is calculated as

$$N_{th} = N_0 \exp\left(\frac{G_{th}}{G_0}\right) = N_0 \exp\left(\frac{\alpha_{tot}}{G_0 \Gamma_{QW} f(R)}\right), \tag{4.11}$$

where α_{tot} is the total modal optical loss consisting of laser cavity loss and output coupling loss.

$$\alpha_{tot} = \alpha_c + \alpha_{cavity} . \tag{4.12}$$

With threshold carrier density, the threshold pump power can be easily derived by the following relation:

$$P_{th} = N_{th} V_a \frac{hc}{\tau_e} \frac{1}{\lambda_{pump}}, \tag{4.13}$$

where V_a is the volume of the active region, h is Planck's Constant, c is the speed of light, λ_{pump} is the pump wavelength, and τ_e is the carrier lifetime defined by

$$\tau_e = \frac{1}{A + BN_{th} + CN_{th}^2}, \tag{4.14}$$

where A is the Scholey-Read-Hall recombination coefficient (10^8 s^{-1}), B is the spontaneous recombination coefficient (2×10^{-10} $cm^3 s^{-1}$), and C is the Auger recombination coefficient (1.65×10^{-28} $cm^6 s^{-1}$). The calculated threshold pump power and threshold pump power density for microdisk lasers are plotted in Figure 4.9. Since the output coupling loss is a useful loss, and determines the laser output power and differential quantum efficiency, we will optimize it separately in the next section.

Here, we only consider the microdisk lasers without output waveguide integration ($\alpha_c = 0$). Figure 4.9(c) and Figure 4.9(d) show that thicker microdisk lasers exhibit higher threshold due to larger cavity loss, which is mainly caused by scattering loss as shown in Figure 4.8(b). Larger-radius microdisk lasers exhibit smaller threshold pump power density because of smaller cavity loss (Figure 4.9(b)). However, because larger microdisk lasers need more power to pump the whole disk, assuming uniform illumination, the threshold pump power increases with the radius even though the threshold pump power density decreases. In conclusion, smaller and thinner microdisk lasers exhibit lower threshold pump power. However, we cannot make the microdisk lasers too thin. Otherwise, the confinement factor of quantum wells will decrease, resulting in smaller modal gain and thus higher threshold. In addition, the optical mode will not be completely confined if the disk is too thin. It will also be too fragile for assembly on a silicon platform.

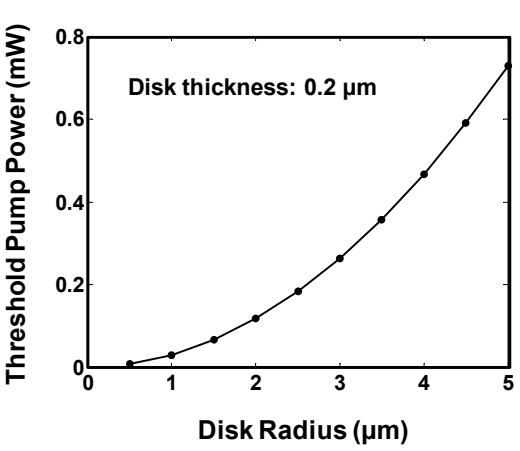

(a)

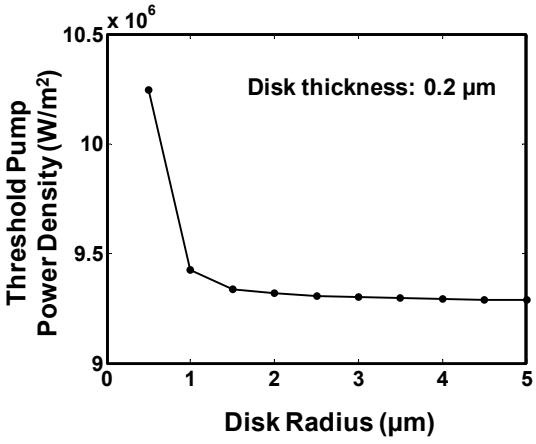

(b)

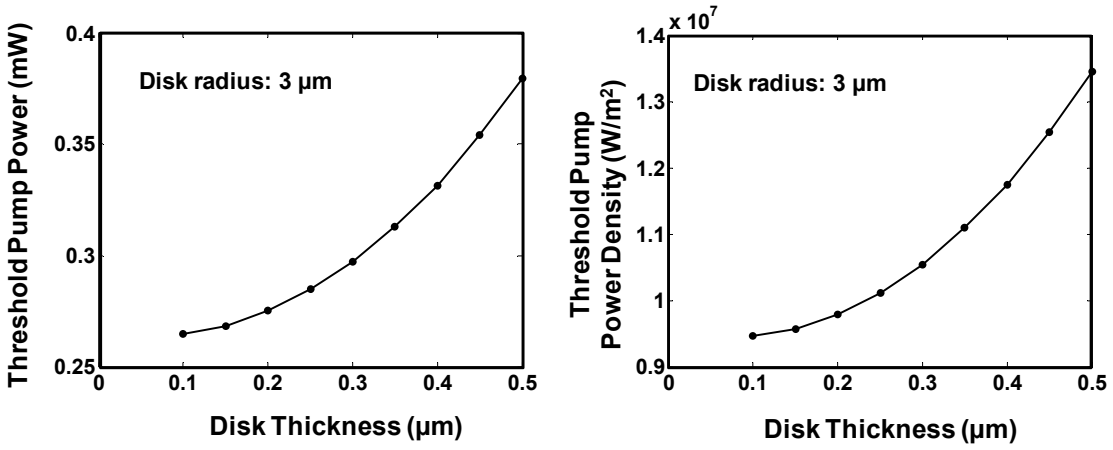

(c) (d)

Figure 4.9 Calculated threshold pump power and threshold pump power density for InP-based microdisk MQW lasers versus (a, b) disk radius and (c, d) disk thickness. The pump wavelength is assumed to be 635 nm.

4.4.4 Output Coupling of Microdisk Lasers

The output coupling from the microdisk laser to the integrated waveguide is an important parameter that determines the laser output power and external differential quantum efficiency, in addition to the threshold pump power. The laser threshold is described in Equation (4.13) and the external differential quantum is given by

$$\eta_{ex} = \eta_{\text{int}} \frac{\alpha_c}{\alpha_c + \alpha_{cavity}} , \tag{4.15}$$

with η_{int} the internal quantum efficiency of microdisk lasers and α_c distributed coupling loss. Figure 4.10 plots the calculated (a) laser threshold and (b) external differential quantum efficiency of microdisk lasers with different radii versus the coupling loss. The threshold pump power of microdisk lasers increases with disk radius (Figure 4.10(a)), but the differential quantum efficiency is almost independent of disk radius (Figure 4.10(b)). Larger coupling loss results in larger threshold power since it contributes more total

modal loss, and thus a larger gain is required to reach the lasing condition. On the other hand, larger coupling loss also means a larger portion of laser power is coupled to the output waveguide and results in higher differential quantum efficiency. Therefore, there is a trade-off between the laser threshold and differential quantum efficiency, and the coupling loss needs to be carefully chosen to have lasers with high differential quantum efficiency while maintaining reasonably low threshold power. For example, a 3-μm-radius microdisk laser with 80% of differential quantum efficiency will have a threshold power of 0.6 mW, and the corresponding gap between the microdisk and the silicon waveguide (500 nm by 250 nm) is about 500 nm, according to Figure 4.6.

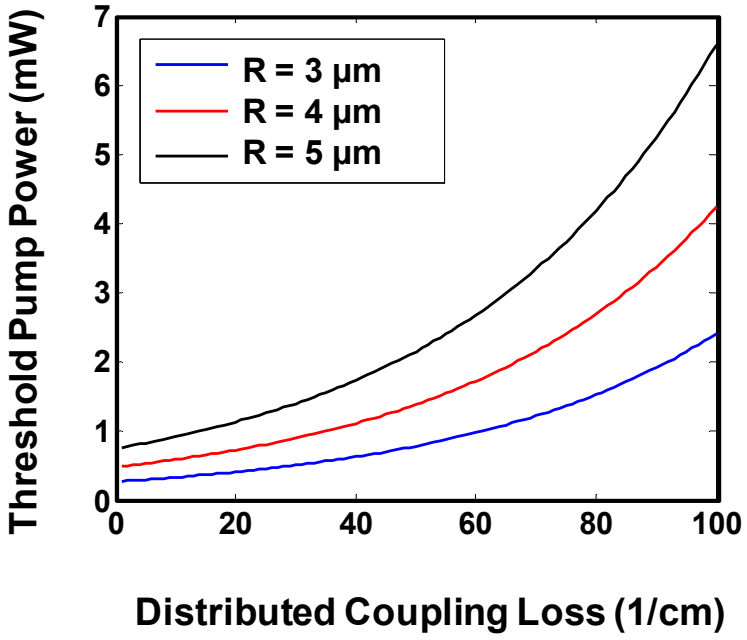

(a)

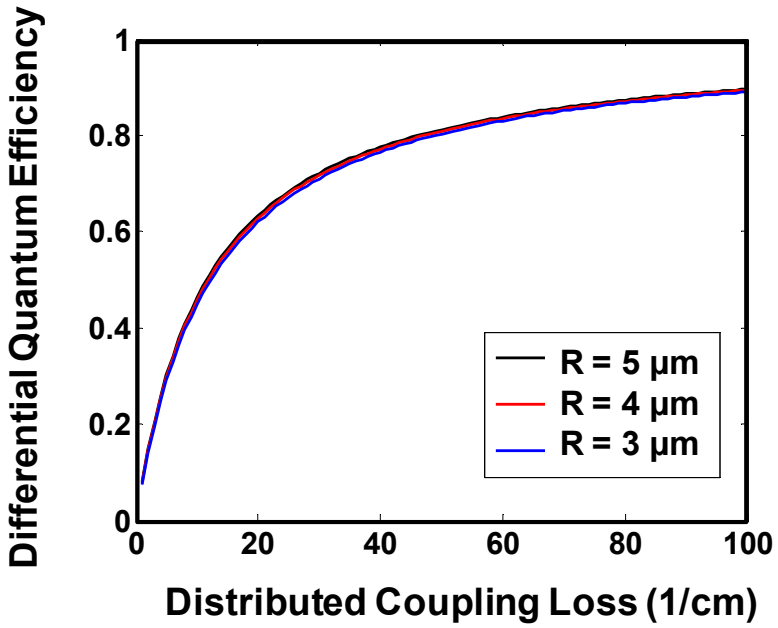

(b)

Figure 4.10 (a) Threshold pump power and (b) external differential quantum efficiency of microdisk lasers with different radii versus distributed coupling loss from the microdisk to the output waveguide. The internal quantum efficiency is assumed to be 100%.

Chapter 5 Optofluidic Assembly Techniques

5.1 Fluidic Self-assembly

Fluidic self-assembly technology uses a simple process to integrate various types of devices onto a common substrate, and thus enables fast, parallel heterogeneous integration. Fluidic self-assembly has been demonstrated utilizing different forces, such as gravity [98], capillary forces [99], coulombic forces [100], and magnetic forces [101]. Alien Technology Corporation has developed their products by fluidically self-assembling semiconductor devices on a low-cost substrate. Some examples are radio-frequency identification (RFID) tags and light emitting diode (LED) displays on plastics in conjunction with roll-to-roll manufacturing techniques. They utilize gravitational and hydrodynamic forces to place trapezoidally shaped micro-components into similarly shaped holes on a target substrate. The parts are fluidically transported across the substrate in water. Once assembled into the holes, they are held in place by gravity, van

der Waals forces, and upon drying, capillary forces. The assembly is then laminated to affix the parts permanently. The schematic assembly process is depicted in Figure 5.1.

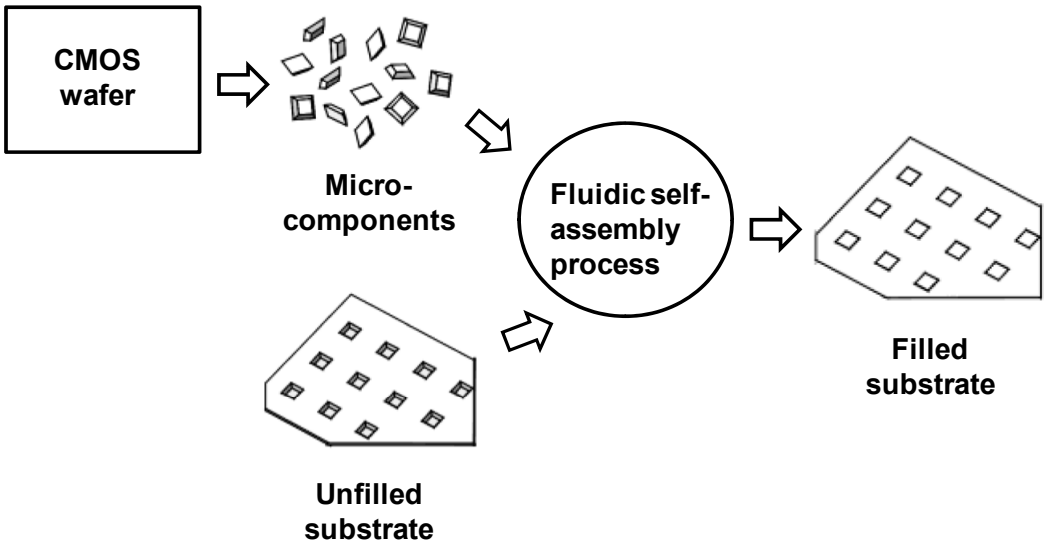

Figure 5.1 Block diagram of fluidic self-assembly process developed by Alien Technology Corporation [98].

Optical MEMS is another application of fluidic self-assembly. Researchers at the Berkeley Sensor and Actuator Center (BSAC) demonstrated self-assembly of micromirrors onto microactuators located on another substrate using capillary forces [99]. The microactuators are coated with hydrophobic adhesive liquid as the self-assembly bonding sites. Then the released hydrophobic mirrors are directed towards the substrate with microactuators using a pipette. When a hydrophobic pattern on a mirror comes into contact with an adhesive-coated bonding site, shape-matching occurs spontaneously due to interfacial free-energy minimization. The assembled mirrors are held in place by capillary forces. Once the assembly is complete, permanent bonding is achieved by thermally curing the adhesives. Finally, the substrate is removed from the water and dried

by a super-critical carbon dioxide process. The final assembled mirror on a microactuator is shown in Figure 5.2.

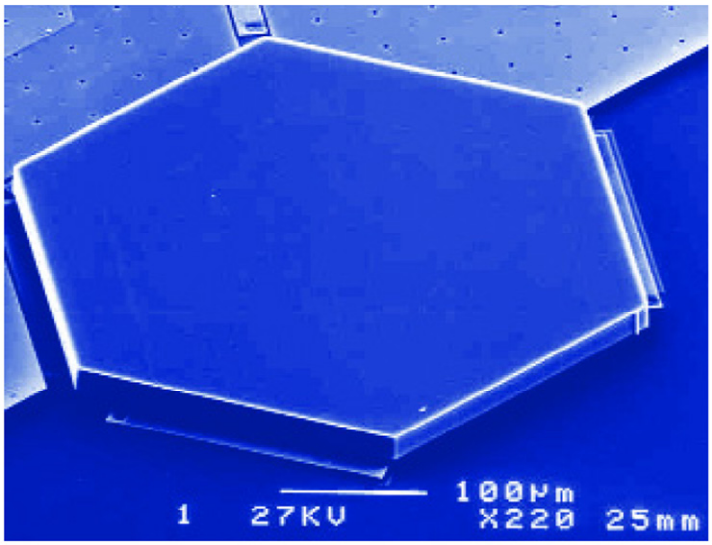

Figure 5.2 An assembled silicon micromirror on a microactuator for an adaptive optics application (reproduced from [99]).

III-V optoelectronic devices can also be assembled onto silicon substrates using similar approaches. GaAs LEDs and InGaAs vertical cavity surface emitting lasers (VCSELs) are demonstrated to be self-assembled in shape-matching holes on silicon substrates [102, 103]. Furthermore, fast fluidic self-packaging of LEDs is also made feasible by utilizing geometrical shape recognition with site-specific wetting and binding involving liquid solder [104].

One problem with self-assembly is that it is difficult to fix assembly defects if a bonding site misses the target. In addition, the size of these assembled devices is typically more than 10 µm. For electronics and photonics integration, the footprints of devices are becoming smaller, which necessitates sub-micron alignment accuracy. Therefore, we

propose an optofluidic assembly process assisted by optoelectronic tweezers (OET) that can fix the assembly defects and maintain high assembly accuracy simultaneously [90].

5.2 Optoelectronic Tweezers

5.2.1 Overview of OET

OET [105] is a manipulation tool that utilizes optically induced dielectrophoresis (DEP) forces to actuate micro- and nano-particles in liquid. It uses optical beams to pattern virtual electrodes on photoconductive materials, generates a local non-uniform electric field, and then induces a DEP force on those polarized particles. As shown in Figure 5.3, the OET device is a two-electrode device consisting of top and bottom transparent electrodes made of indium tin oxide (ITO). A photoconductive layer, hydrogenated amorphous silicon (a-Si:H), lies on the top of the bottom electrode and spacers are used to create a chamber between the photoconductive layer and the top electrode. Filling with an aqueous solution containing particles of interest in the chamber, OET can fluidically manipulate the particles.

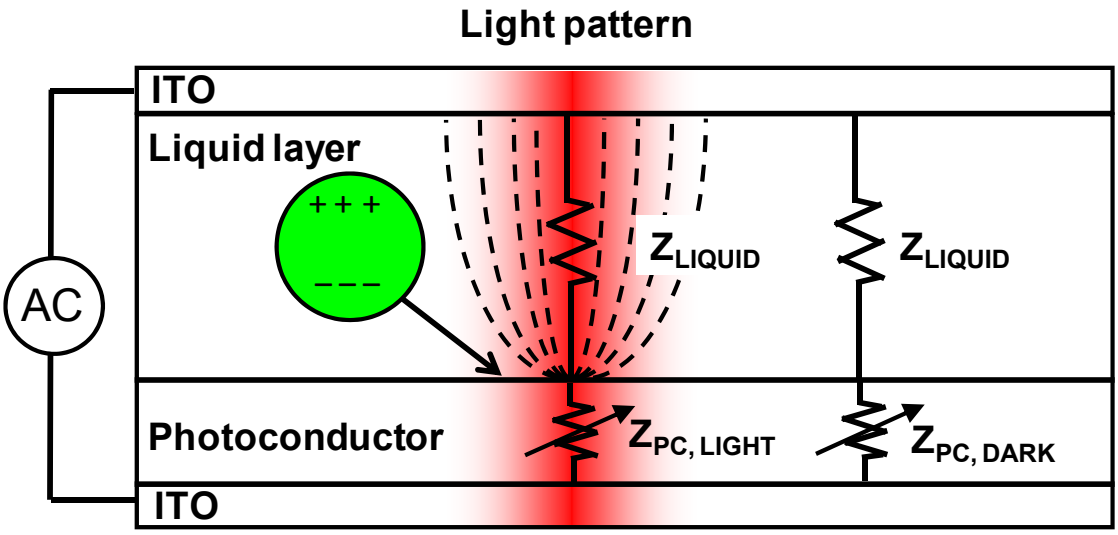

Figure 5.3 Cross-sectional view diagram of OET showing the working principle. The photoconductor is sandwiched by top and bottom electrodes with liquid in between for fluidic manipulation. With optical illumination, the photoconductor is locally turned on, and thus generates a non-uniform electric field that induces DEP forces on particles.

The photoconductive layer acts as a gate that controls the passing of the electric field through the liquid layer. Without optical illumination on the photoconductive layer, the impedance of the photoconductor is larger than that of the liquid ($Z_{PC,DARK} > Z_{LIQUID}$). Most of the ac bias voltage drops across the photoconductive layer and there is no electric field in the liquid layer. When light is projected onto the photoconductors, the impedance of the photoconductive layer decreases so that it is smaller than that of the liquid ($Z_{PC,LIGHT} < Z_{LIQUID}$), up to three orders of magnitudes smaller under an illumination intensity of 2.5 W/cm^2 [106, 107]. Most of the ac bias voltage then drops across the liquid layer and generates a local non-uniform electric field that polarizes the particles and induces DEP forces. Due to the optical gain from the photoconductor, the minimum required optical intensity to turn on a virtual electrode is approximately 1 W/cm^2. This allows us to use a digital projector to generate any desired optical images on the OET device for massively parallel manipulation as shown in Figure 5.4.

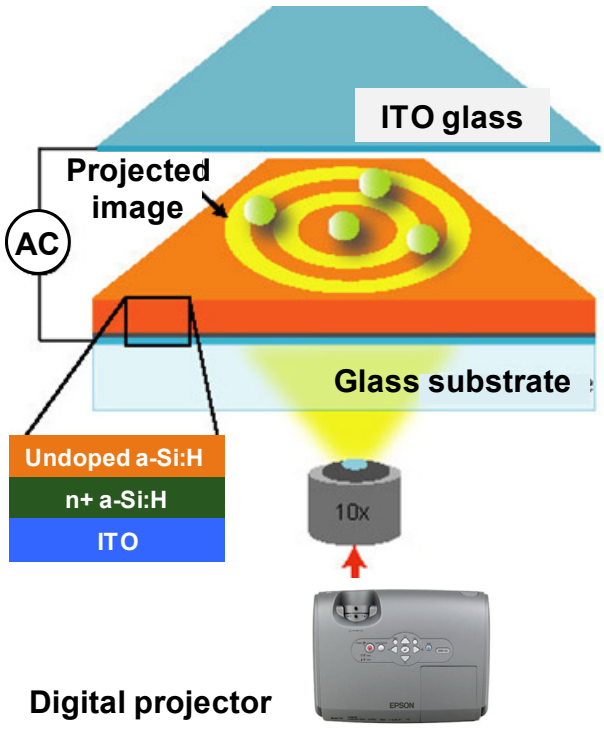

Figure 5.4 Schematic of OET. Optical patterns are projected onto the OET device through an objective to actuate the particles of interest. A large manipulation area and low required optical power enable massively parallel manipulation.

5.2.2 Theoretical Analysis of OET

Electric field gradients in the OET devices are controlled by the a-Si photoconductivity depending on the illumination intensity [107]. Figure 5.5 shows the simulated conductivity of the a-Si layer and the resulting electric field distribution in the OET device. The light intensity profile follows the Gaussian distribution; therefore, the conductivity also follows the Gaussian distribution and has the highest point in the center of the light. The highly conductive a-Si acts as a virtual electrode and generates an electric field in the liquid layer by applying a bias voltage to the top and bottom electrodes. The electric field distribution is similar to the electric field between a point electrode and a planar electrode.

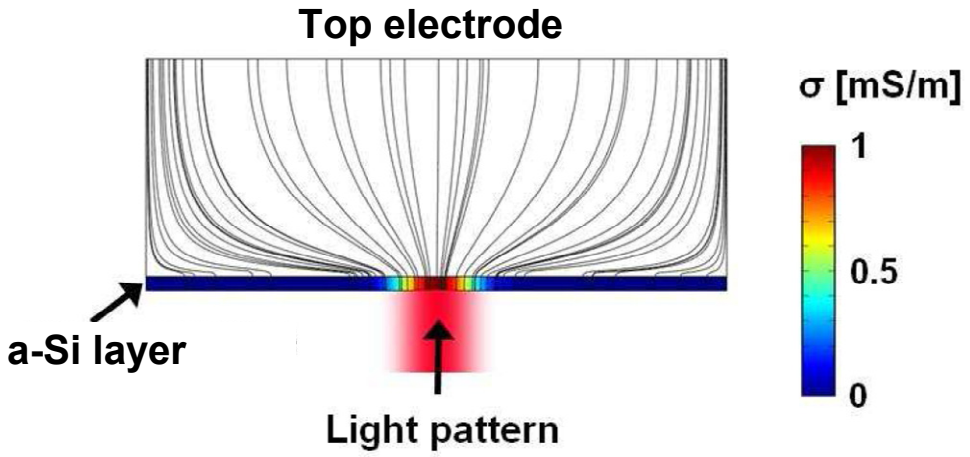

Figure 5.5 Simulated electric field distribution of OET. The color gradient shows the conductivity gradient in the a-Si layer, generated by the illumination. Note the major electric field direction is normal to the surface plane.

DEP forces result from the interaction of a non-uniform electric field and the induced dipole of a particle within the electric field. The DEP forces at each end of the particle's dipole are unequal due to the non-uniform field, resulting in a net force. The force is also dependent on the shape of the particle. For a spherical particle, the force can be expressed as [108]

$$F_{DEP} = 2\pi R^3 \varepsilon_m \,\mathrm{Re}\left(\frac{\varepsilon_p^* - \varepsilon_m^*}{\varepsilon_p^* - 2\varepsilon_m^*}\right)\nabla\left|\vec{E}\right|^2 , \tag{5.1}$$

where R is the radius of the sphere, $\vec{E}$ is the electric field, ε_m^* and ε_p^* are the permittivities of the surrounding medium and the particle, respectively. For the DEP force on a thin disk (radius much larger than thickness), the disk can be approximately treated as an oblate spheroidal particle (as shown in Figure 5.6) and the force can be written as [108]

$$F_{DEP} = \frac{4\pi abc\left(\varepsilon_p - \varepsilon_m\right)}{3}\left[\frac{E_x}{1+L_x\left(\frac{\varepsilon_p-\varepsilon_m}{\varepsilon_m}\right)}\frac{\partial}{\partial x} + \frac{E_y}{1+L_y\left(\frac{\varepsilon_p-\varepsilon_m}{\varepsilon_m}\right)}\frac{\partial}{\partial y} + \frac{E_z}{1+L_z\left(\frac{\varepsilon_p-\varepsilon_m}{\varepsilon_m}\right)}\frac{\partial}{\partial z}\right]\left|\vec{E}\right|, \quad (5.2)$$

where a and b are the equatorial radii (along the x and y axes), and c is the polar radius (along the z axis). L_x, L_y, and L_z are depolarization factors along x, y, and z axes. They can be expressed as

$$\begin{aligned} L_x = L_y &= \frac{a^2 c}{2\left(a^2-c^2\right)}\left[\frac{\pi}{2\sqrt{a^2-c^2}} - \frac{c}{a^2}\right] \\ L_z &= 1 - L_x - L_y \end{aligned} . \quad (5.3)$$

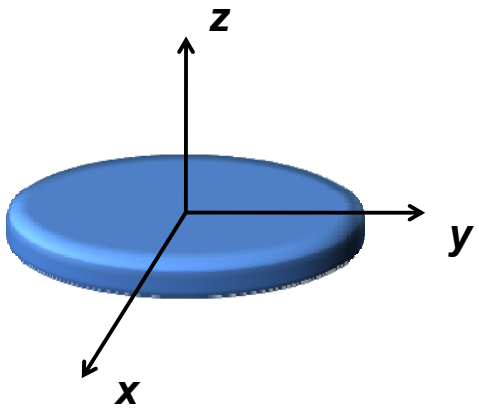

Figure 5.6 Coordinates of oblate spheroid used to mimic the disk.

The calculated DEP forces on microdisks with different radii are plotted in Figure 5.7. The maximum gradient of the electric field square ($\nabla\left|\vec{E}\right|^2$) is assumed 4.5×10^{15} V^2/m^3 for our calculation [109]. Because the force is proportional to the particle volume, it increases with the disk radius. For a 3-μm-radius semiconductor disk with a thickness of 200 nm and conductivity of 1 S/m, the DEP force is approximately 500 pN.

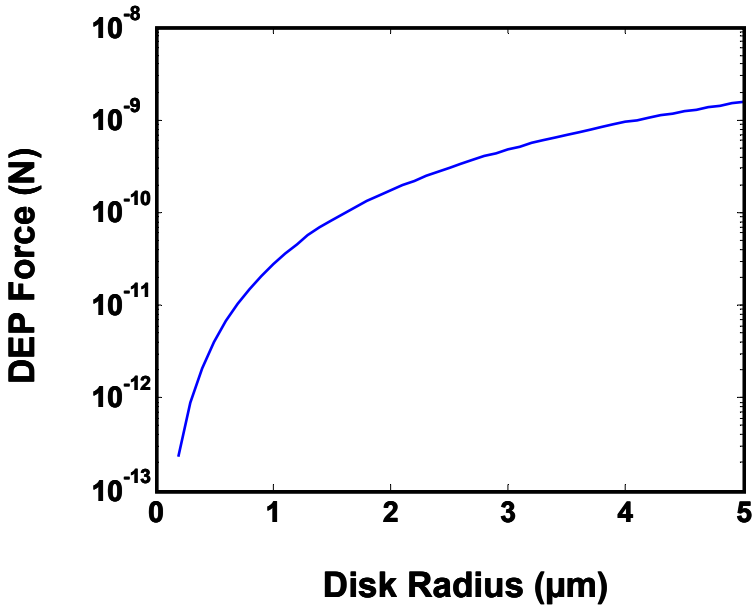

Figure 5.7 DEP forces on microdisks versus disk radius. Disk thickness is 200 nm and conductivity is 1 S/m. The gradient of the electric field square is 4.5×10^{15} V^2/m^3.

It should be noted that there are two types of DEP forces, positive and negative, depending on the relative permittivities of the surrounding medium and the particle. The particle is attracted by positive DEP forces while it's repelled by negative DEP forces. For semiconductor microdisks, OET generates an attractive force by the positive DEP.

5.3 Lateral-field Optoelectronic Tweezers (LOET)

5.3.1 Motivation

Although OET is a highly flexible and versatile device, certain limitations exist. The electric field in the OET device is created in a liquid layer between the planar top and bottom electrodes (Figure 5.3). As a result, it is difficult for OET to integrate with those devices that do not provide electrodes on both sides. In addition, anisotropic particles will align along the electric field direction, normal to the plane of the electrodes of OET

(Figure 5.5), due to the torque exerted on the induced dipole of the particle. It is not suitable for assembling microdisks as they stand perpendicular to the substrate and it is difficult to precisely position the microdisks.

To solve this problem, a new device with single-sided electrodes and an electric field parallel to the surface plane is developed. The lateral-field optoelectronic tweezers (LOET) [107, 110, 111] are a variation of OET. Instead of parallel plate electrodes, an interdigitated electrode array is used. Because both electrodes of LOET are on the same side, the resulting electric field direction is parallel to the device surface across the gap of the electrodes, as shown in Figure 5.8. Thus, microdisks can be directly placed on the substrate, which provides better alignment accuracy. The single-sided structure also enables integration with other devices. For example, the LOET can be integrated with silicon photonic circuits for heterogeneous laser assembly, which is described in the next chapter.

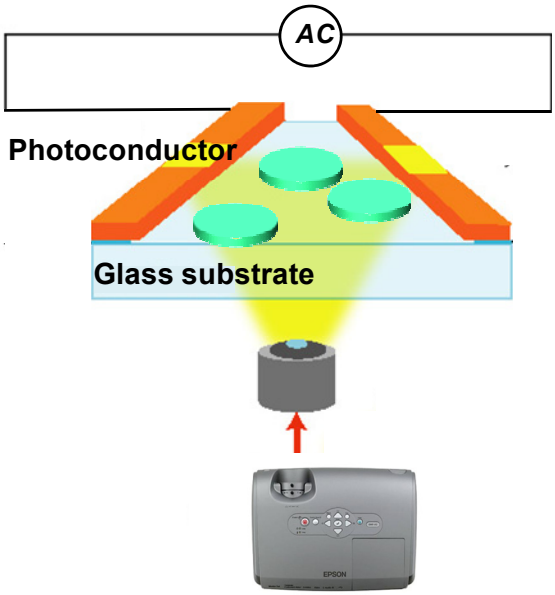

Figure 5.8 Schematic of later-field optoelectronic tweezers. The electrodes are both on the bottom side and thus provide electric field parallel to the surface plane.

5.3.2 Structure and Principle of LOET

The LOET is a single-sided device composed by an insulating substrate, a patterned metal layer, and a patterned photoconductive layer (Figure 5.9). The liquid layer containing particles of interest is introduced to the chamber between the photoconductive layer and the top cover glass. The interdigitated electrodes have smaller gap spacing, resulting in a strong electric field and thus larger forces. On the other hand, the manipulation area is determined by the area of interdigitated electrodes. Therefore, an LOET with a strong force and a large manipulation area is feasible.

The equivalent circuit of the LOET device is represented in Figure 5.9 [107]. As with standard OET, in the area without illumination the impedance of the a-Si layers is much larger than that of the liquid layer ($Z_{PC} > Z_{LIQUID}$), and thus, most of the ac voltage drops across the a-Si layers. To actuate the LOET device, both electrodes are illuminated to reduce the impedance of the a-Si layers to less than that of the liquid layer ($Z_{PC} < Z_{LIQUID}$). Most of the ac voltage switches from the a-Si layers to the liquid layer. This dramatically increases the electric field between the electrodes. The COMSOL simulation of the electric field distribution in the liquid layer is shown in Figure 5.10. The direction of the electric field is parallel to the device surface across the gap of the electrodes. As a result, microdisks can be placed on the substrate directly with their normal direction perpendicular to the electric field direction.

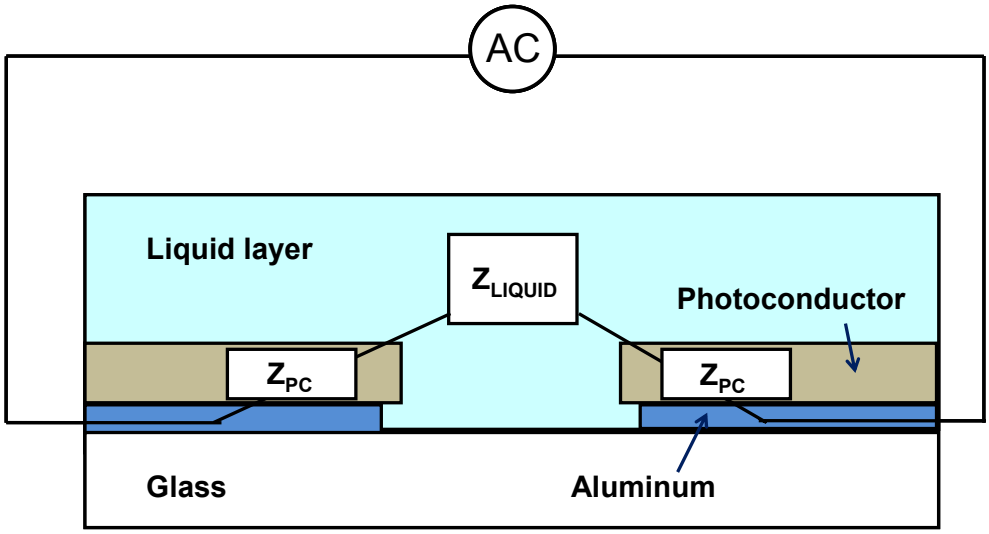

Figure 5.9 Cross-sectional view diagram of LOET which is composed by an insulating layer, a patterned metal layer, and a patterned photoconductive layer. The in-plane electrodes generate electric fields parallel to the substrate surface that place microdisks on the substrate directly.

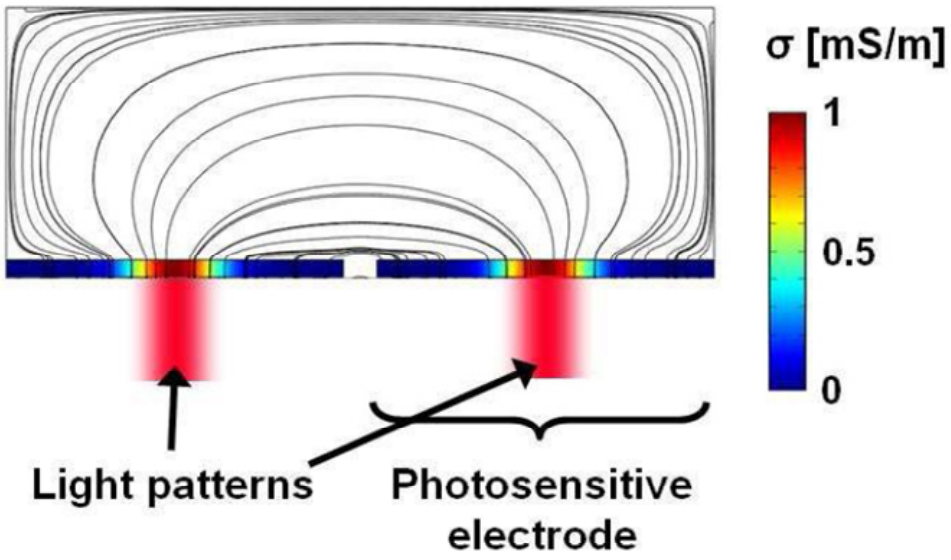

Figure 5.10 Simulated electric field distribution in the LOET devices by COMSOL with optical illumination. The electric field between the electrodes is parallel to the substrate surface [111].

5.4 Planar Lateral-field Optoelectronic Tweezers (PLOET)

The LOET is capable of trapping, transporting, and aligning anisotropic particles over the substrate precisely. However, it is difficult to rotate the particle. In addition, the topography over the device may hinder the movement of some particles. Therefore, another variation of OET, planar lateral-field optoelectronic tweezers (PLOET), is developed [112].

The structure of PLOET is similar to LOET, but the a-Si layer is not etched, creating a planar surface. As shown in Figure 5.11, it consists of an insulating layer, patterned metal electrodes, and a planar a-Si photoconductive layer. The a-Si acts as a virtual electrode controlled by optical illumination. It also acts as extensions of the metal electrodes with illumination and an insulator without illumination.

The equivalent circuit of PLOET is described in Figure 5.11. The a-Si layer is divided into two different regions, the extension of the metal electrode (Z_{PC1}) and the middle non-activated region (Z_{PC2}). Similar to LOET, without illumination, impedance of the a-Si (both Z_{PC1} and Z_{PC2}) is large so that it acts as an insulator to block the electrode field. However, the activation of PLOET is a little different from that of LOET. The light patterns are illuminated on the regions extending from the metal electrodes (Z_{PC1}) while the middle region (Z_{PC2}) remains un-illuminated. The impedance of the a-Si with illumination is smaller than that of the liquid layer, which is even smaller than that of the a-Si without illumination ($Z_{PC1} < Z_{LIQUID} < Z_{PC2}$). Thus, most of the ac bias voltage drops across the parallel network of Z_{PC2} and Z_{LIQUID}.

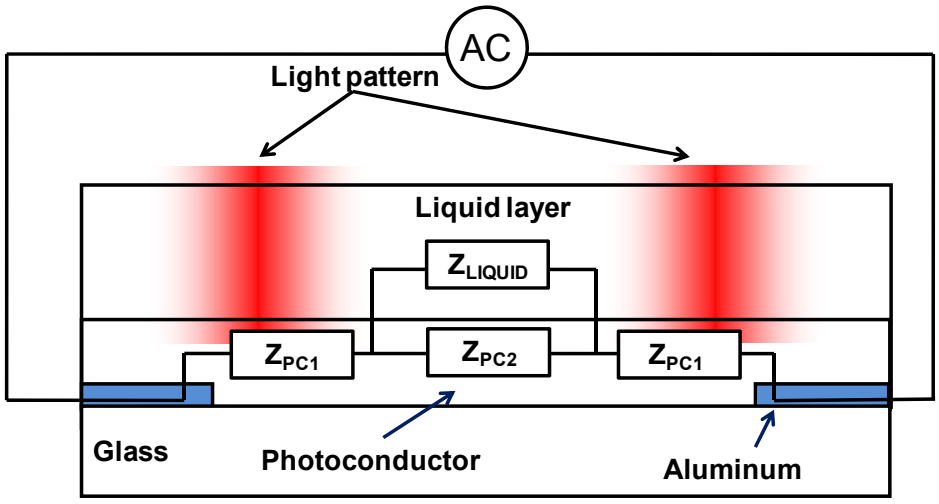

Figure 5.11 Cross-sectional view diagram and equivalent circuits of PLOET. It consists of an insulating layer, patterned metal electrodes, and a planar photoconductive layer. The equivalent circuit of the device is also labeled on the diagram.

Typically, two triangular optical patterns are illuminated on the PLOET for device operations, as shown in Figure 5.12. The illuminated a-Si acts as extensions of the metal electrodes, resulting in strong electric fields at the tips of the optical patterns. These virtual tips can *pick and place* the particles of interest to locations within the gap. For anisotropic objects, PLOET can also rotate the particles.

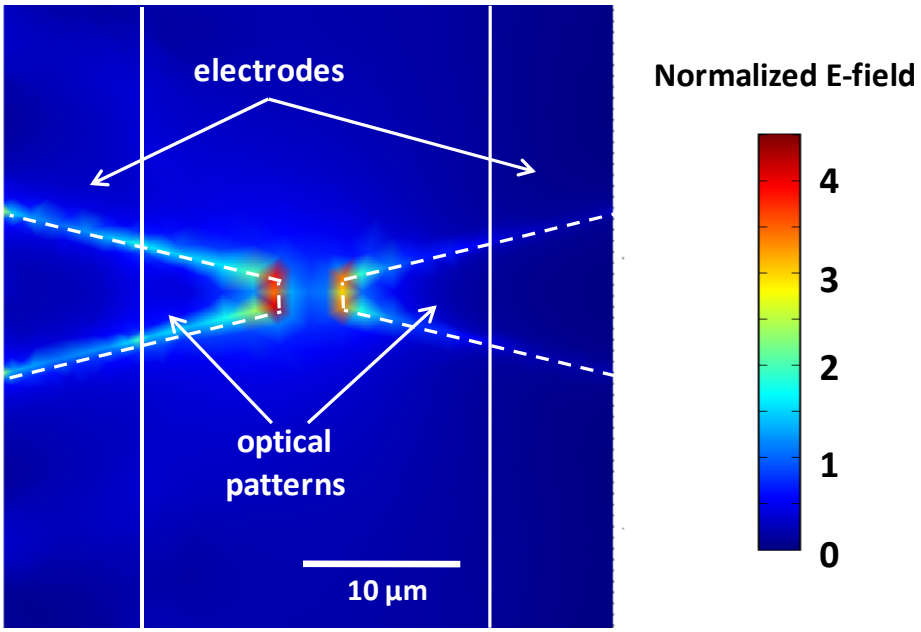

Figure 5.12 Simulated electric field intensity profile of PLOET (top view). The optical patterns are in triangular shape, and the strongest electric field occurs at the tips of the optical patterns. The separation of the metal electrodes is 20 µm.

Chapter 6 III-V Microdisk Lasers on Silicon Photonic Circuits

6.1 Overview of Optofluidic Assembly Using LOET

Copper interconnects have inherently limited bandwidth (< 10 Gb/s). This creates a bottleneck in computer servers as the data rate increases. Optical interconnects are an attractive alternative to copper because of higher bandwidth and potentially lower power consumption. They are increasingly employed in short-distance communication such as board-to-board interconnects. They have not yet been used in chip-to-chip or intrachip interconnects, partially because of the difficulty in integrating electronic and photonic components.

Fabricating optical elements directly on silicon can lower the manufacturing costs and increase integration of optical components. Silicon photonic devices are designed to be compatible with CMOS processes, leveraging the existing manufacturing infrastructure. Many silicon photonic devices such as modulators [8-10], filters [11],

multiplexers [12], switches [13, 14], and photodetectors [15, 16] have been successfully demonstrated. However, it is still challenging to directly integrate electrically-pumped lasers on silicon. An alternative solution is heterogeneous integration of III-V semiconductor lasers on silicon.

To integrate III-V semiconductor lasers on silicon-based electronic and photonic integrated circuits, wafer bonding is a commonly used [23, 24, 26]. However, some issues still exist. For instance, the surface topography presents a challenge for wafer bonding. In addition, the size and density mismatches between the silicon and III-V epitaxial wafers result in inefficient use of the III-V wafers. As depicted in Figure 6.1, the typical size of III-V wafers is two to four inches while that of silicon wafers (or SOI) is eight to twelve inches. In addition, only a few lasers are needed for applications such as optical transceivers. Most of the bonded III-V epi-materials end up being removed.

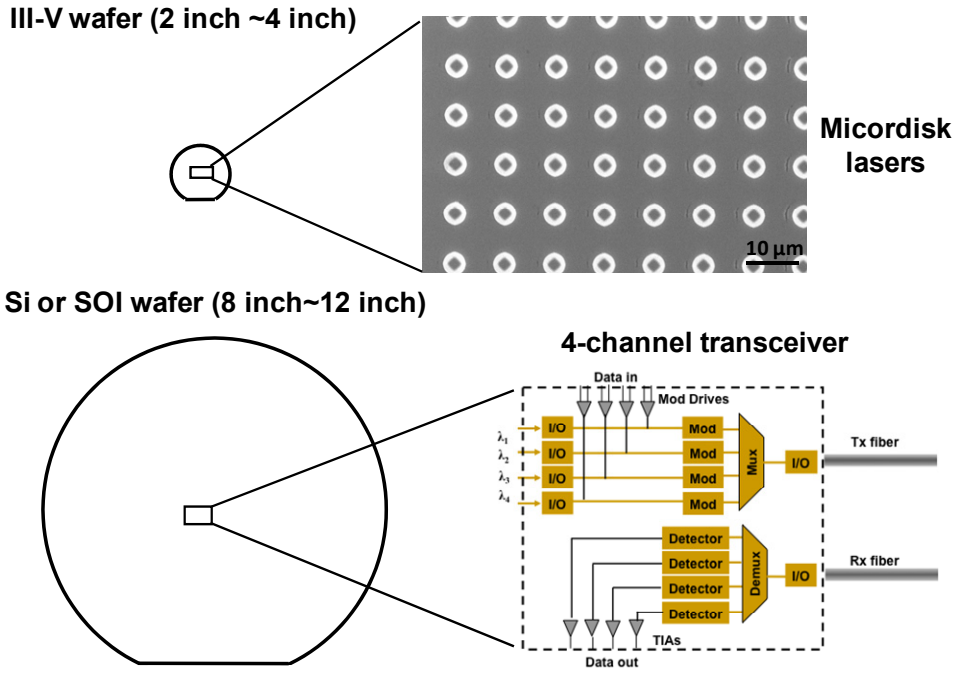

Figure 6.1 Schematic showing the size and density mismatches between III-V and silicon wafers. III-V wafers (2" ~ 4") are typically much smaller than Si wafers (8"~12"), while the device density on III-V wafers can be much larger than that required on silicon wafer, such as transceivers.

To solve these issues, we propose an optofluidic assembly process assisted by LOET to integrate III-V microdisk lasers onto silicon platforms. The LOET retains the capability of OET while enabling the integration with other electronic and photonic devices. Taking advantage of this feature, the LOET is integrated with the silicon photonic circuits to assist III-V microdisk laser assembly. The schematic diagram is shown in Figure 6.2. Optical patterns projected from a digital projector are focused on the LOET device through an objective. With proper bias voltage to the LOET electrodes, microdisk lasers are attracted to the illuminated area, and aligned to the silicon optical waveguides by light patterns. Optofluidic assembly can directly place the lasers on the silicon waveguides. Since a larger number of lasers can be harvested from a single III-V substrate, they can potentially be assembled on multiple silicon wafers. The assembly is performed at room temperature, which is compatible with post-CMOS processing.

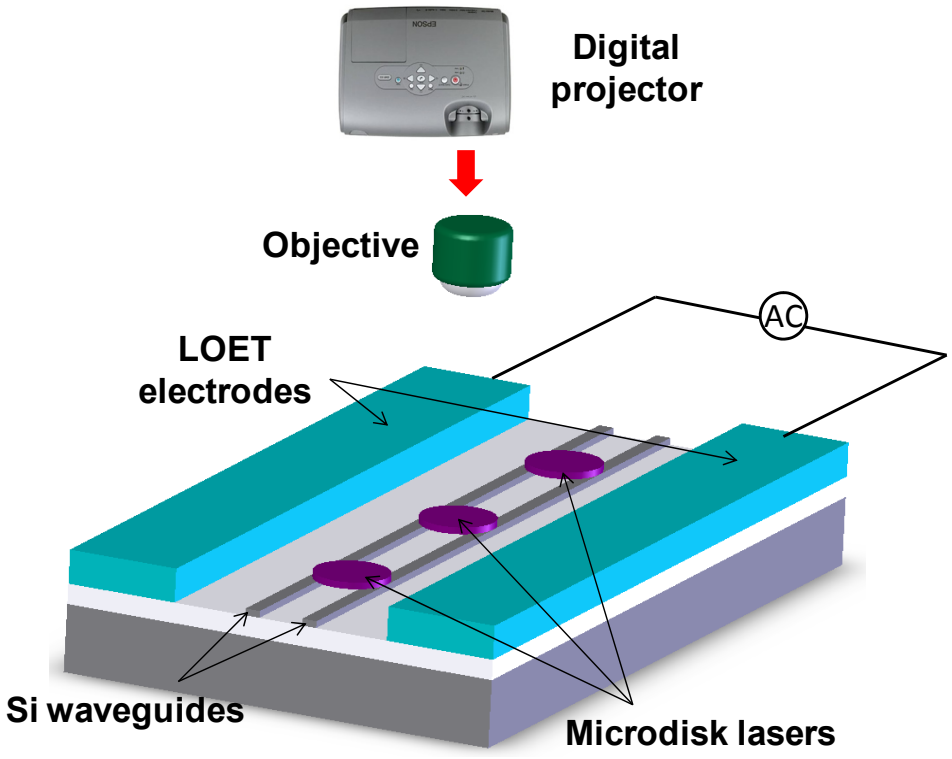

Figure 6.2 Schematic diagram of silicon photonic circuits integrated with LOET for microdisk laser assembly. The optical image patterns are projected from the digital projector controlled by a computer. Microdisk lasers are assembled and aligned to the waveguides with the assistance of LOET.

6.2 Microdisk Laser Preparation

6.2.1 Structure and Fabrication

The microdisk laser is fabricated using an InGaAs/InGaAsP/InP MQW epitaxial wafer with a photoluminescence peak at 1550 nm [90, 113]. Optical gain is provided by three 7-nm-thick InGaAs quantum wells separated by 10-nm-thick InGaAsP (bandgap wavelength λ_g = 1.2 μm) barrier layers. The MQW layers are sandwiched between two symmetric InGaAsP optical confinement layers (λ_g = 1.1μm). The detailed epitaxial structure is shown in Table 6.1. The total thickness of the microdisk laser is intentionally kept very thin (200 nm) so that output light can easily couple evanescently to the Si

waveguides. The microdisk lasers were grown by metal organic chemical vapor deposition (MOCVD) on an InP substrate (by Landmark Optoelectronics Corp.).

Layer (bandgap)	Thickness	Description
1.1 μm -InGaAsP	20 nm	Optical confinement layer
1.2 μm -InGaAsP	50 nm	Optical confinement layer
1.2 μm -InGaAsP	10 nm × 4	4-layer barriers
$In_{0.53}Ga_{0.47}As$	7 nm × 3	3-layer wells
1.2 μm -InGaAsP	50 nm	Optical confinement layer
1.1 μm -InGaAsP	20 nm	Optical confinement layer
InP	350 μm	Substrate (sacrificial layer)

Table 6.1 Epitaxial layer structure of microdisk lasers. The InGaAs/InGaAsP MQW with a photoluminescence peak at 1550 nm are sandwiched by larger-bandgap optical confinement layers.

Microdisk lasers with different diameters are fabricated using standard optical lithography and wet etching processes, as shown in Figure 6.3. The circular microdisk pattern is transferred from a photoresist to a silicon nitride hardmask by plasma etching. After removing the photoresist, the hardmask pattern is then transferred through the active layers to the InP sacrificial layer by a nonselective etchant of 0.5% Br_2 in methanol. Finally, after stripping the hardmask, the MQW microdisks are released by etching the InP sacrificial layer using a diluted hydrochloric acid (HCl). The microdisks are re-suspended in ethanol for assembly onto a silicon platform. Figure 6.4 (a) shows the fabricated 5-μm-diameter microdisks on a partially etched InP sacrificial layer. A close-up view of the microdisk is shown in Figure 6.4 (b). The wet etching produces a smooth sidewall and therefore low scattering loss for the laser cavity.

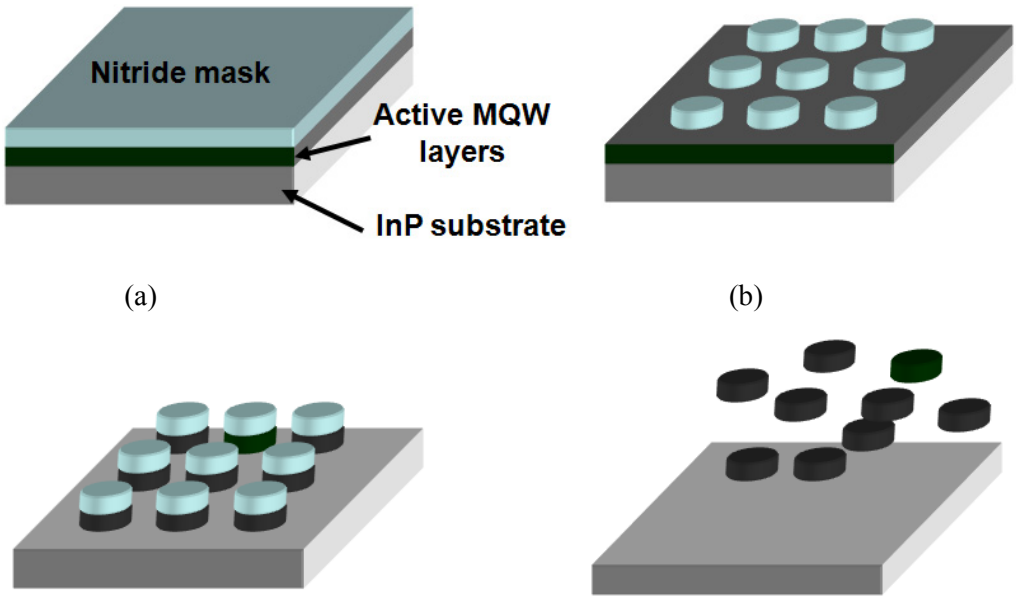

Figure 6.3 Fabrication processes of fully released InGaAs/InGaAsP MQW microdisk lasers. (a) Deposition of silicon nitride hardmask. (b) Etched microdisk patterns in a silicon nitride hardmask. (c) Transfer of the microdisk pattern from the hardmask to the active MQW layers using a nonselective etchant of 0.5% Br_2 in methanol. (d) Stripping the nitride mask and releasing the microdisks by etching the InP sacrificial layer using diluted HCl.

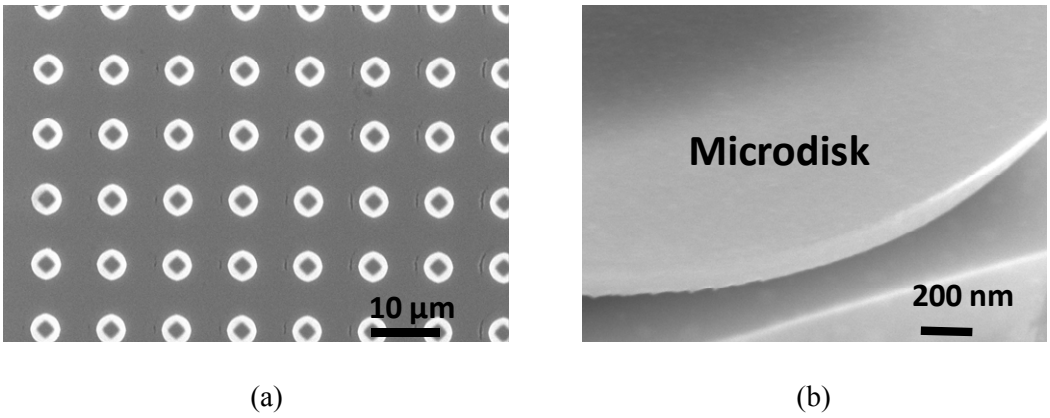

Figure 6.4 SEM images of 5-µm-diameter microdisks on an InP substrate. (a) The disks are wet etched by 0.5% Br_2 in methanol, followed by a partial etch of the InP sacrificial layer using diluted HCl. The rhombic grey region is an InP pedestal under the active InGaAsP/InGaAs MQWs. (b) A close-up image showing the disk sidewall after etching. The smooth sidewall provides a low-loss cavity for the microdisk laser.

6.2.2 Laser Characterization before Release

The microdisk lasers are optically pumped on InP substrates to measure the laser quality before being released and assembled onto the silicon platform. In addition, the performance of the microdisk lasers before and after assembly can be compared. The experimental setup for optical characterization is shown in Figure 6.5. The microdisk lasers are optically pumped at room temperature (18^{o}C) using a 780-nm CW diode laser. The pump beam is focused onto the disk using a 40× objective, resulting in a beam spot size of 3 μm. The emitted light is collected by the same objective. An optical filter is used to block the pump light in the detection path. The filtered optical signal is coupled to a multimode fiber, and the output spectrum is measured by an optical spectrum analyzer. The microdisk lasers are mounted on a thermoelectric cooler (TEC) to maintain a stable temperature.

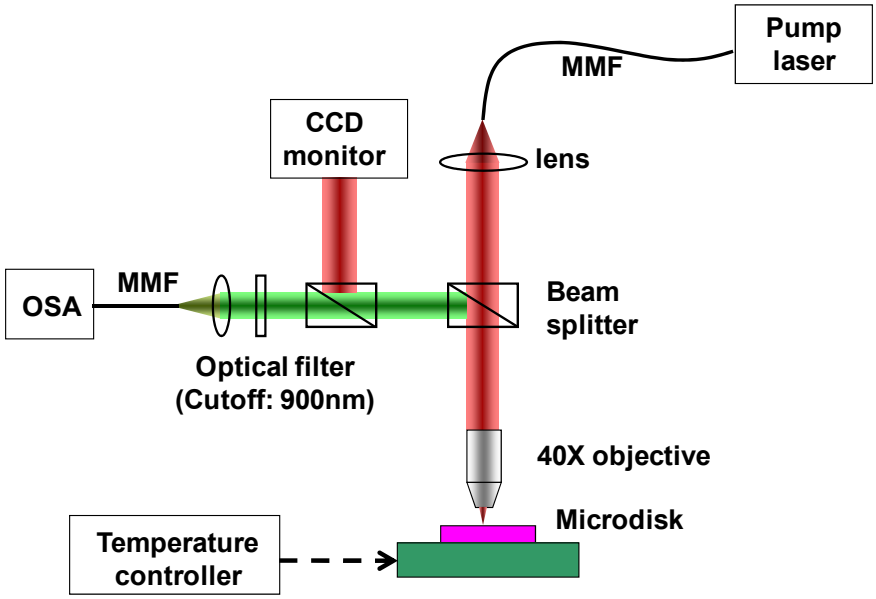

Figure 6.5 Optical measurement setup for microdisk laser characterization. A 780-nm diode laser is used as the pump source. Scattered microdisk laser power is collected by the objective and sent to the OSA through an optical long-pass filter, which prevents the interference from the pump laser. OSA stands for optical spectrum analyzer, and MMF stands for multimode fiber.

The light-versus-pump curve (L-L curve) of a 5-μm-diameter microdisk laser on a partially etched InP sacrificial layer is shown in Figure 6.6 (a). It exhibits an effective threshold pump power of 0.3 mW when excited by a CW 780-nm diode laser. The effective pump power is the power absorbed by the microdisk laser and is given by the following expression [114]:

$$P_e = P_i(1-R)\frac{1-e^{-\alpha d}}{1-\mathrm{Re}^{-\alpha d}}, \tag{6.1}$$

where P_e is effective pump power, P_i is incident optical power on the microdisk surface, d is the total thickness of the microdisk, R is the power reflectivity at the disk surface (~30%), and α is the optical absorption coefficient of the microdisk. For InGaAsP layers with 1.1-μm and 1.2-μm of bandgap, the absorption coefficient at wavelength of 780 nm is about 20,000 cm^{-1} [115]. Therefore, the ratio of the effective pump power to the incident power on the microdisk surface is approximately 30% for 200-nm-thick microdisks.

The CW lasing spectrum of the 5-μm-diameter microdisk laser with an effective pump power of 0.7 mW is measured using an optical spectrum analyzer and shown in Figure 6.6 (b). The peak laser wavelength is 1539.3 nm and the free spectral range is 51.5 nm. The group index of the optical mode (n_g ~ 2.93) can be extracted according to Equation (4.3), which is consistent with theoretical calculations of TE-polarized whispering-gallery mode.

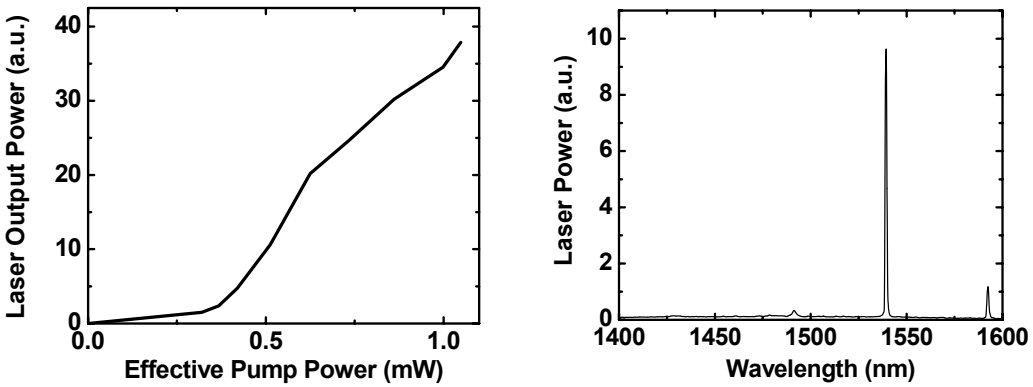

(a) (b)

Figure 6.6 (a) The light-vs-pump (L-L curve) characteristics of the 5-μm-diameter microdisk laser on a partially etched InP sacrificial layer. The effective threshold pump power is 0.3 mW. (b) Lasing spectra of the microdisk lasers on InP substrates under an effective pump of 0.7 mW. The lasing wavelength is 1539.4 nm.

The temperature dependency of microdisk laser performance is also studied. The lasing spectra at different temperatures are shown in Figure 6.7. The microdisk continues to lase in CW for temperatures up to 28^{o}C, due to the good thermal conductivity of InP (68 W/m.K). When the temperature increases, the lasing peak shifts toward longer wavelength and becomes broader.

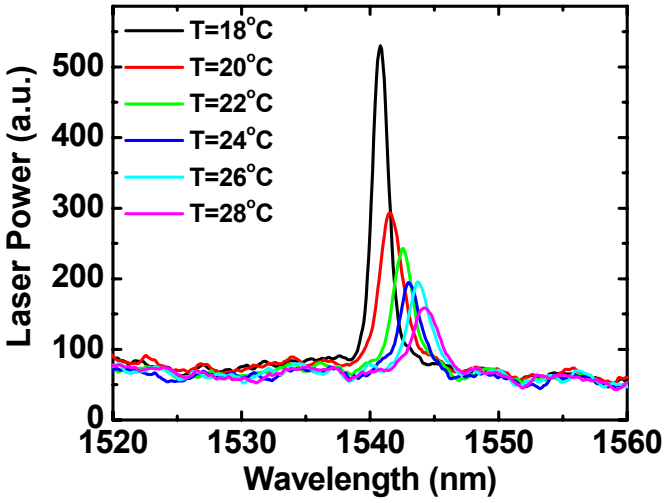

Figure 6.7 Temperature dependency of microdisk lasing spectra.

6.3 LOET with Silicon Pedestals

6.3.1 Device Fabrication

The microdisk lasers support whispering-gallery mode (WGM). Figure 6.8 shows the calculated magnetic field intensity profiles of the fundamental transverse electric (TE) WGM mode for the 5- and 10-μm-diameter microdisk lasers using the eigenmode expansion model. The electromagnetic field is concentrated near the edge of the microdisk. To minimize scattering loss and optical leakage due to the underneath silicon pedestals, the diameters of the Si pedestals supporting the microdisk lasers are designed to be 3 and 7 μm, respectively, for the 5- and 10-μm-diameter lasers [85].

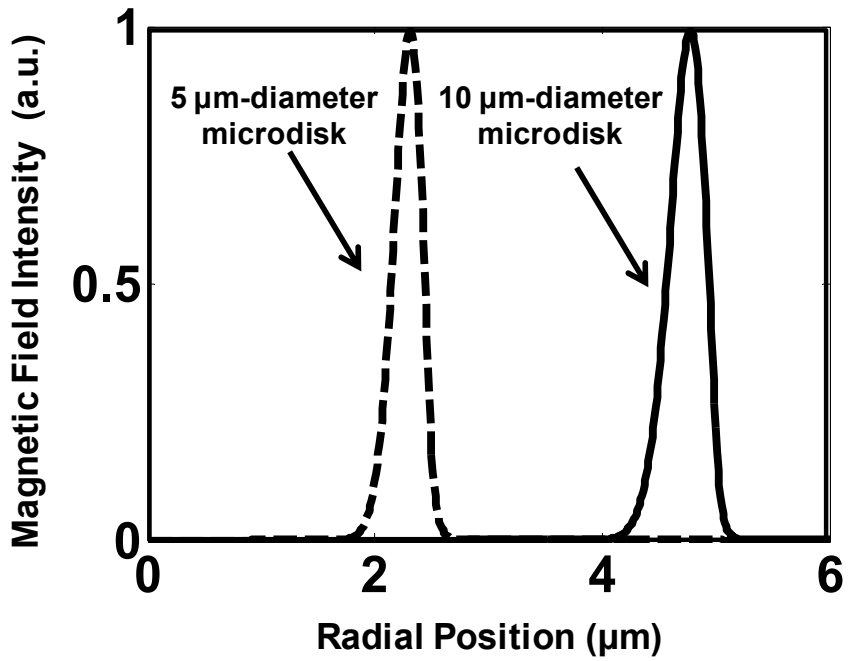

Figure 6.8 The calculated magnetic field intensity profiles of the fundamental TE WGM for 5- and 10-μm-diameter microdisks using the eigenmode expansion model.

The schematic of the LOET with a silicon pedestal for microdisk laser assembly is illustrated in Figure 6.9. A pair of photoconductive electrodes is patterned around a silicon pedestal, upon which the microdisk laser will be assembled. An ac voltage is applied across the electrodes, which consist of a 100-nm-thick aluminum layer, topped by 0.8 μm of a-Si. The operation of the LOET has been described in Section 5.3. The highest forces occur near the edges of the LOET electrode (Figure 6.10), which attract and align the microdisks in the center of the electrodes when the size of the disk is equal to or larger than the gap spacing [111]. The simulated electric field distribution in the LOET device with a silicon pedestal is shown in Figure 6.10, where arrows indicate the direction of the DEP forces.

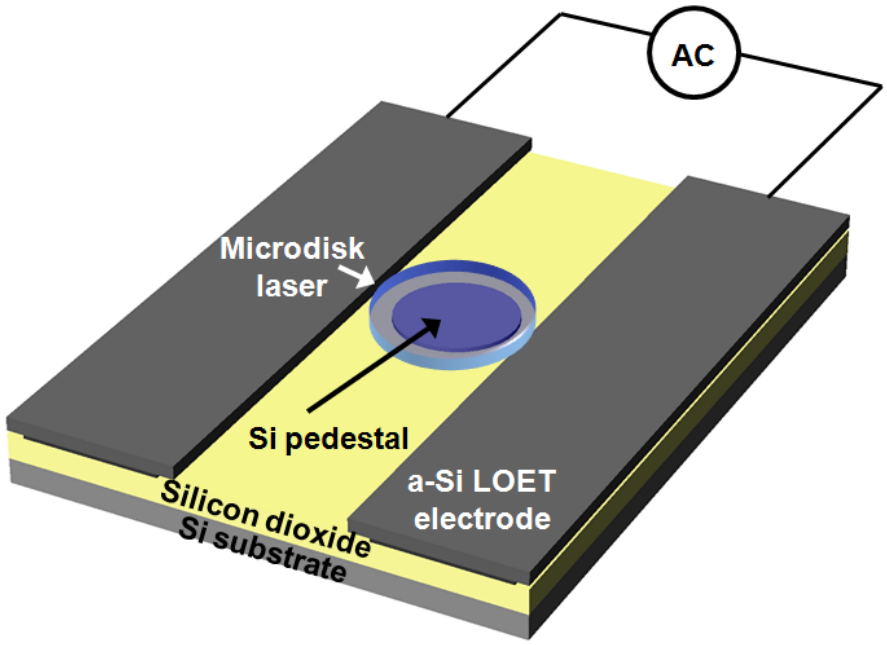

Figure 6.9 Schematic of LOET with a microdisk laser assembled onto a silicon pedestal.

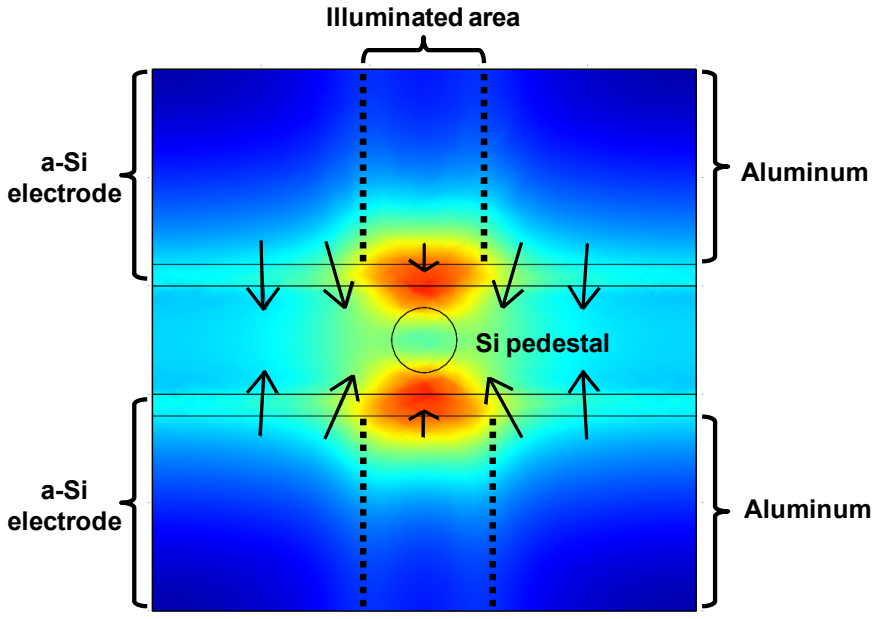

Figure 6.10 Finite-element simulation of the electric field profile across the LOET electrodes. The arrows show the direction of the optically-induced DEP force. The strongest forces occur near the edges of illuminated electrodes.

The detailed fabrication process of the LOET structure is shown in Figure 6.11. It is fabricated on an SOI wafer using a two-mask process. Silicon pedestals are first patterned in the top silicon layer by optical lithography and dry etching (Figure 6.11(b)). A thin layer of oxide is grown by thermal oxidation to passivate the pedestals (Figure 6.11(c)). The 100-nm-thick aluminum and 0.8-μm-thick a-Si layers are then deposited and patterned to create the LOET electrodes (Figure 6.11(d), (e)). The pedestals are centered in the gap between the electrodes. At this point, the device is ready for the microdisk assembly process (Figure 6.11(f), (g)), which is described in Section 6.3.2. After assembly, the a-Si layer is removed by XeF_2 etching at 40°C (Figure 6.11(h)).

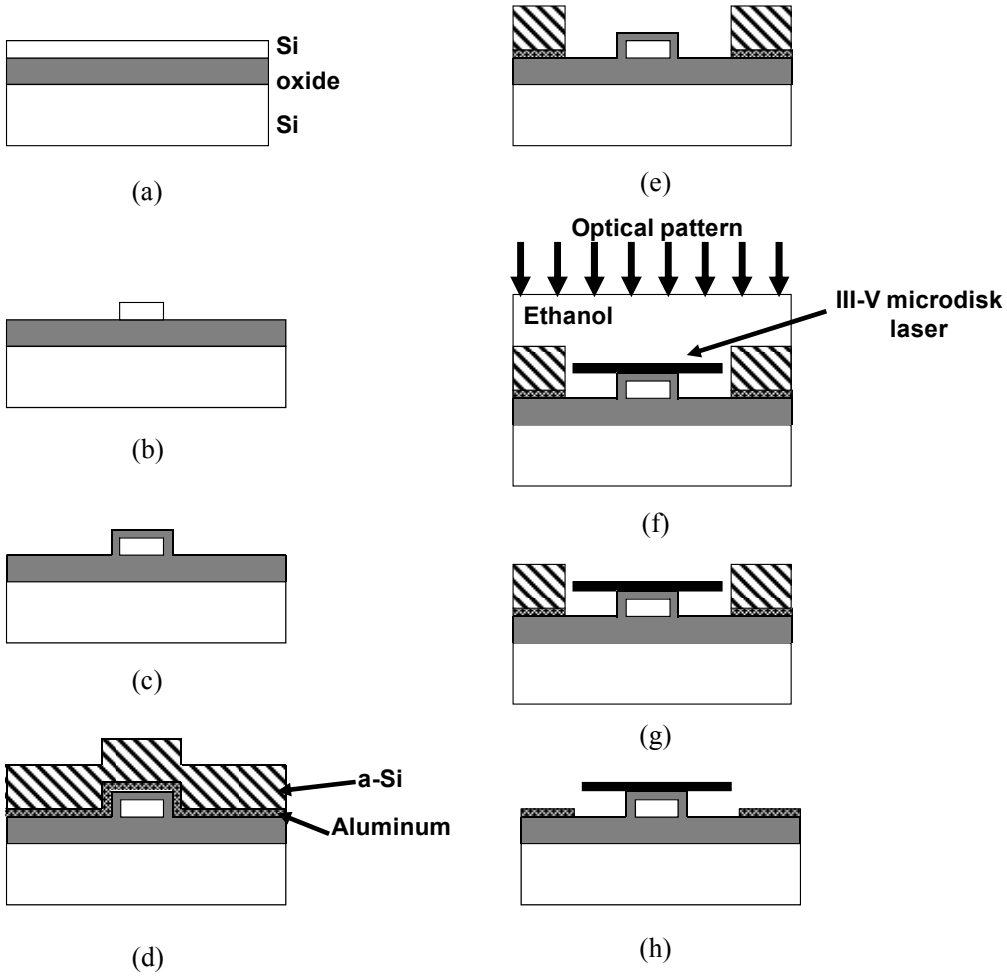

Figure 6.11 (a) The fabrication of pedestal-integrated LOET starts with an SOI wafer. (b) A Si pedestal is patterned using standard optical lithography. (c) A 50-nm-thick thermal oxide is grown to protect the pedestal from subsequent etches. (d) 100-nm-thick aluminum and 0.8-μm-thick a-Si are deposited by an e-beam evaporator and plasma-enhanced chemical vapor deposition (PECVD), respectively. (e) The LOET electrodes are defined by etching a-Si and aluminum. (f) The suspended microdisks are pipetted onto the substrate. The disks can then be trapped and positioned in solution. (g) The microdisks are held on the pedestals until the solution dries. (h) The a-Si layer is removed to avoid interference with the optical mode of the microdisk.

6.3.2 Microdisk Laser Assembly Using LOET

The fabricated InP-based microdisks, suspended in ~90% ethanol, are pipetted onto the substrate. The LOET electrodes create an optically-induced DEP force which attracts microdisks to illuminated areas, and the microdisks self-align in the gap between the electrodes. A computer-controlled optical pattern is projected onto the LOET device through an objective, as shown in Figure 6.12. A CCD is used to monitor the relative locations of the projected pattern, the microdisks, and the pedestals. The projector provides real-time control over the optical patterns, which allow transportation of the microdisks along the length of the LOET electrodes using an applied ac voltage of 1 to 10 Vpp at 200 kHz. Once the disks are aligned over a pedestal, the applied voltage is increased to 20 Vpp to hold the disks in place as the solution dries. Ethanol is used to minimize surface tension forces during the drying process. After it is dry, the a-Si layer is removed to avoid interference with the optical modes in microdisks.

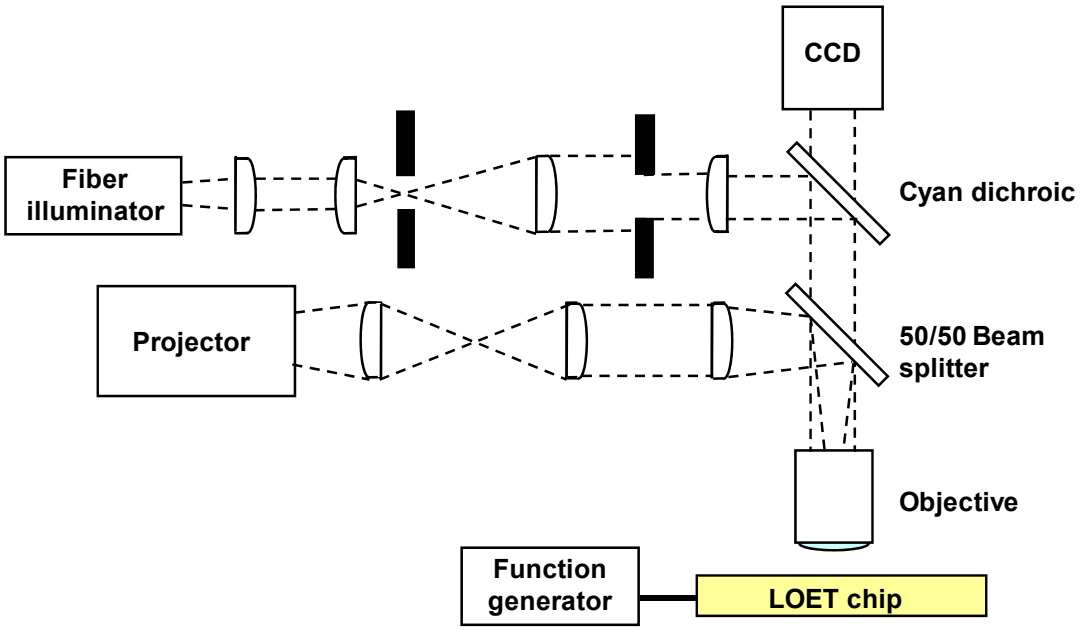

(a)

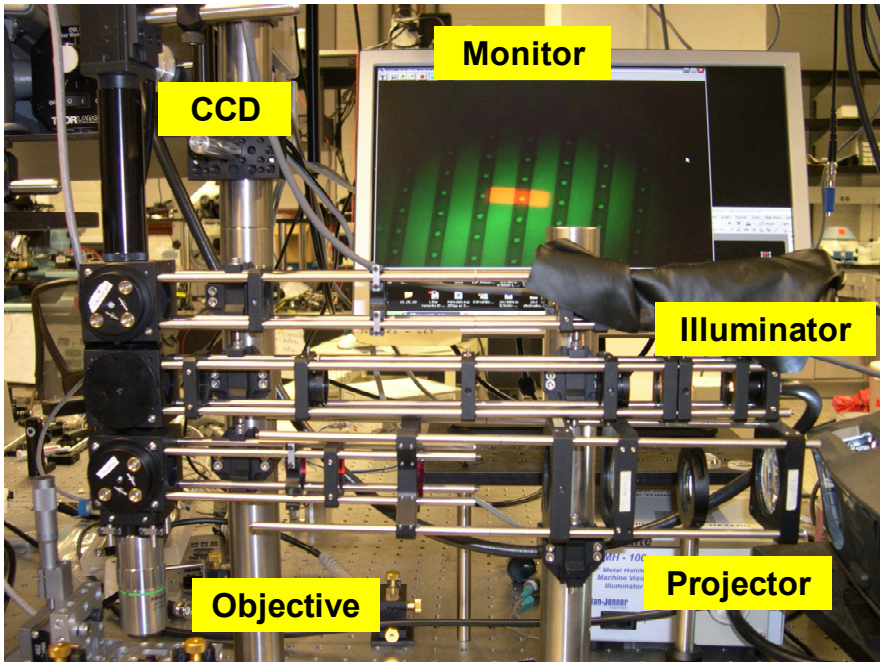

(b)

Figure 6.12 (a) Schematic of an experimental setup for parallel assembly of microdisks on Si. A computer-controlled projector generates optical patterns to attract and transport microdisks to a designated position. A function generator is used to apply the bias voltage to the LOET device. (b) Photo of the experimental setup for microisk assembly.

Figure 6.13 displays a series of microscope images showing the assembly process for the 5-µm-diameter (Figure 6.13(a)-(c)) and 10-µm-diameter microdisks (Figure 6.13(d)-(f)). As the gap between electrodes is 5 µm, the 5-µm-diameter microdisks fit in between the electrodes (Figure 6.13(a)-(c)), while the 10-µm-diameter microdisks self-align in the middle of the gap (Figure 6.13(d)-(f)). Both microdisks can be moved along the length of the electrodes by the optical patterns. The SEM images of the assembled 10-µm-diameter microdisk are shown in Figure 6.14.

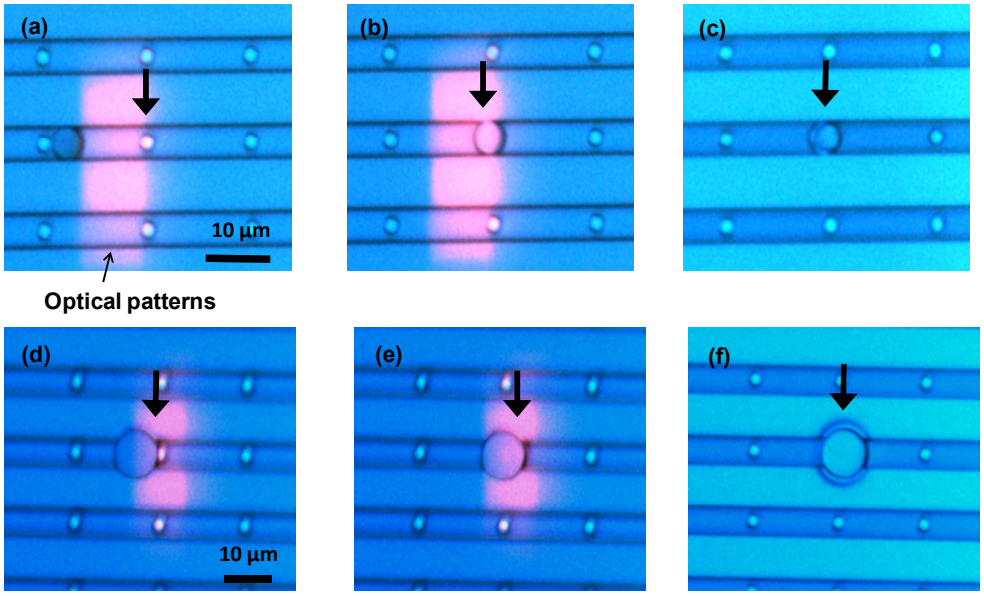

Figure 6.13 Assembly of the 5-µm-diameter (a-c) and 10-µm-diameter (d-f) InGaAs/InGaAsP microdisk lasers onto 3-µm-diameter silicon pedestals using LOET. (a, d) The initial positions of the microdisks. The optical trapping pattern, generated by a computer projector, is visible as a red rectangle. The microdisks are attracted towards the trapping pattern by an optically-induced DEP force. The target Si pedestal for assembly is indicated by the arrow. (b, e) The microdisks are positioned over the target Si pedestal. The trapping force is then increased to immobilize the disks on the substrates. (c, f) The assembled microdisks remain in place after the liquid solution has dried.

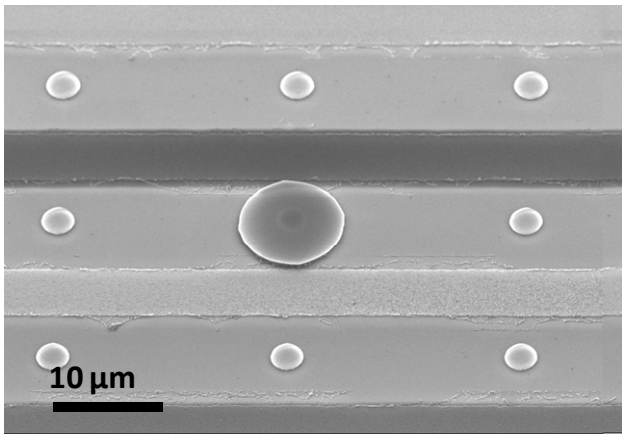

Figure 6.14 An SEM image of an assembled 10-µm-diameter microdisk.

The alignment accuracy of the assembled microdisks on the pedestals is also investigated [116]. As shown in Figure 6.15(a), the microdisk is self-aligned to the center of the gap in the direction perpendicular to the electrodes for those disks larger than the gap. The alignment in the direction parallel to the electrodes is controlled by the projected light. The resulting alignment accuracy is measured in three LOET chips. The disk misalignment is 0.13 µm in the direction perpendicular to the electrodes, and 0.25 µm along the direction of the electrodes, as summarized in Figure 6.15(b).

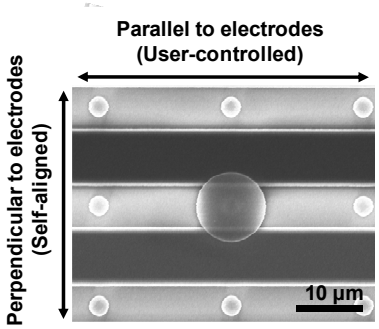

Chip	Misalignment [µm] perpendicular to electrodes	Misalignment [µm] parallel to electrodes
1	0.16 (1.5%)	0.08 (0.7%)
2	0.08 (0.8%)	0.23 (2.3%)
3	0.15 (1.4%)	0.45 (4.2%)
Average	0.13 ± 0.05	0.25 ± 0.18

Figure 6.15 (a) An SEM image of an aligned microdisk on an Si pedestal. (b) Alignment accuracy of assembled microdisks on three separate chips. The disk is self-aligned to the center of the gap in the direction perpendicular to the electrodes due to a symmetric DEP force. The alignment along the direction of the electrodes is controlled by the projected light pattern.

6.3.3 Laser Characterization

The assembled microdisk lasers are optically pumped at room temperature (18^{o}C) using a 780-nm diode laser with 0.5-μs pulses and 20 kHz repetition rate (1% duty cycle). The optical measurement setup is the same as depicted in Figure 6.5. The light-versus-pump curves of the microdisk lasers assembled on Si pedestals are shown in Figure 6.16 (a). Approximately 30% of the pump power is absorbed by the microdisks. The resulting effective thresholds are therefore 0.25 mW and 0.75 mW for the 5- and 10-μm microdisk lasers, respectively. A comparison of the light-vs-pump characteristics of unreleased microdisk lasers on InP pedestals is shown in Figure 6.6(a). There is no significant difference in the effective threshold pump powers between the unreleased and the assembled microdisk lasers, indicating the microdisks are not damaged during the assembly process. The measured lasing spectra of the assembled lasers are shown in Figure 6.16 (b). Both lasers exhibit single mode operation. The peak lasing wavelengths are 1558.7 and 1586 nm for the 5- and 10-μm microdisks, respectively.

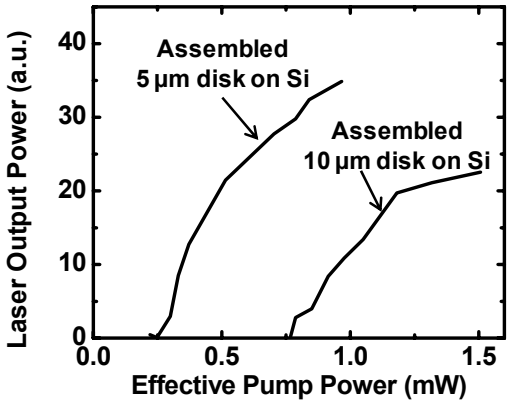

(a)

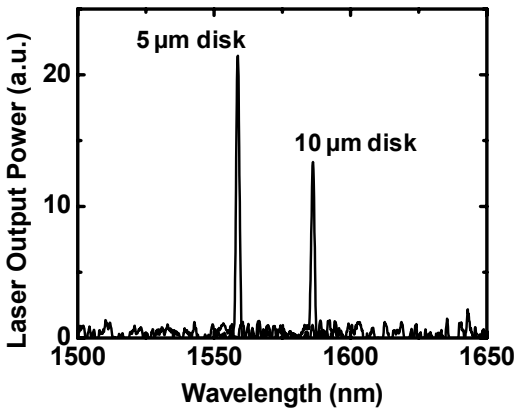

(b)

Figure 6.16 (a) The light-vs-pump characteristics of the assembled microdisk lasers on Si. The effective threshold pump powers are 0.25 and 0.75 mW for the 5- and 10-μm-diameter microdisk lasers, respectively. (b) Lasing spectra of assembled microdisks on Si. Single mode operations are observed for both lasers.

Heating of the microdisk lasers eventually limits the maximum output power when the effective pump powers exceed 0.5 and 1.2 mW for the 5-μm and 10-μm microdisks, respectively (Figure 6.16 (a)). The thermal resistances of the assembled lasers are higher than the unreleased lasers. The 3-μm-thick buried oxide under the Si pedestals substantially increases the thermal resistance due to the low thermal conductivity of silicon oxide (1.4 W/m.K). The poor contact between the microdisk lasers and the silicon pedestals may also contribute to the high thermal resistance. Preliminary experiments have shown that a low temperature thermal annealing (at 300ºC) after assembly could improve bonding and increase the maximum output power (Figure 6.17) [116].

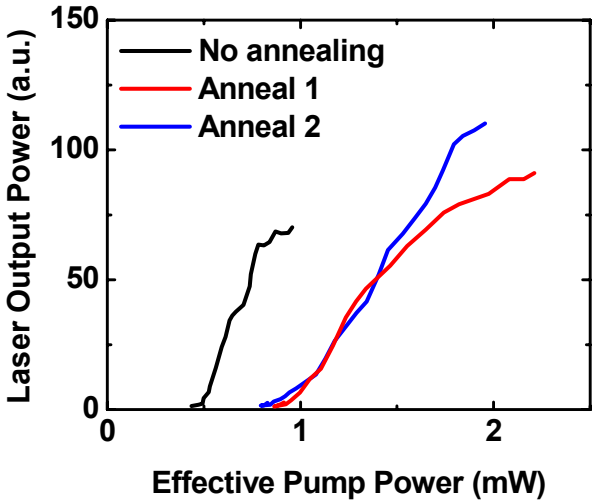

Figure 6.17 L-L curves of assembled 5-μm microdisk lasers before and after thermal annealing. The maximum output power of a 5-μm microdisk laser is improved by annealing at 300°C for 5 hours (Anneal 1), or 300°C for 5 hours followed by another annealing at 350°C for 5 hours (Anneal 2). After annealing, the maximum output power is increased by 30% and 57% for annealing conditions 1 and 2, respectively.

6.4 PLOET with Integrated Silicon Optical Waveguides

In the previous section, we demonstrated assembly of microdisk lasers onto silicon pedestals with the assistance of LOET. Microdisks self-align in the direction perpendicular to the LOET electrodes, but require manual control in the direction parallel to the electrodes. In addition, for silicon photonic circuits with sub-micron single-mode silicon optical waveguides, accurate alignment between the microdisk lasers and the waveguides is critical. Therefore, we propose a new design combining PLOET (described in Section 5.4) with lithographically-patterned matching wells (Figure 6.18). Once the microdisks are transported over the matching wells by PLOET, they drop into the wells and self-align to the underlying waveguides. The alignment accuracy is therefore determined by photolithography. With continuous improvement of photolithography technologies, the misalignment can be less than tens of nanometers.

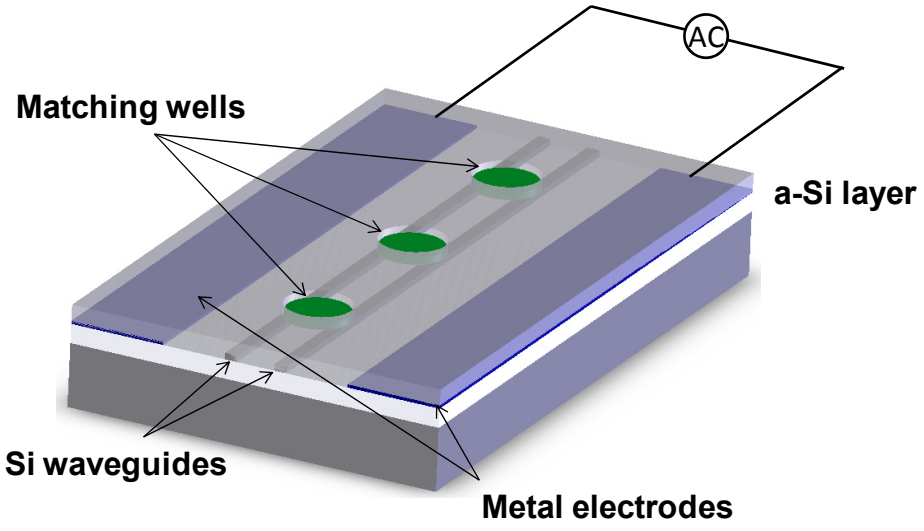

Figure 6.18 Schematic of PLOET with integrated waveguides. The matching wells provide lithographic alignment accuracy for microdisk lasers with the assistance of PLOET.

6.4.1 Device Fabrication

As shown in Figure 6.18, the PLOET device is integrated with silicon waveguides. A pair of 100-nm-thick aluminum electrodes are buried under a 0.8-μm-thick a-Si layer and connected to an ac bias voltage source. With optical illumination, the locally turned-on a-Si generates an electric field and thus induces DEP forces to trap and transport microdisk lasers (described in Section 5.4). Matching wells, created by photolithography and dry etching, provide lithographic assembly and alignment accuracy while PLOET can bring the microdisk lasers to the matching wells. Once the microdisk lasers drop into the well, they are held in place by gravity, van der Waals forces, and upon drying, capillary forces. The matching wells also provide an effective barrier to overcome surface tension forces during drying.

The detailed fabrication processes are depicted in Figure 6.19. The fabrication starts with an SOI wafer, where 3-μm-thick buried oxide electrically isolates PLOET electrodes from the silicon substrate. Silicon waveguides and pedestals are patterned simultaneously by photolithography and dry etching in the device layer of SOI wafers (Figure 6.19(a)). Thermal oxide is then grown to passivate the waveguides and pedestals (Figure 6.19(b)). The thickness of the oxide determines the output coupling from the laser to the waveguides. After that, 100-nm-thick aluminum electrodes are patterned by photolithography and wet etching (Figure 6.19(c)). Then 0.8-μm-thick a-Si photoconductive layer is deposited by PECVD (Figure 6.19(d)). The wells housing microdisks are patterned by photolithography and dry etching (Figure 6.19(e)). Though the alignment accuracy is limited to 100 nm by the stepper at the Berkeley Microlab

(GCA 8500 Wafer Stepper), much better alignment can be readily achieved by current lithography tools used in the industry.

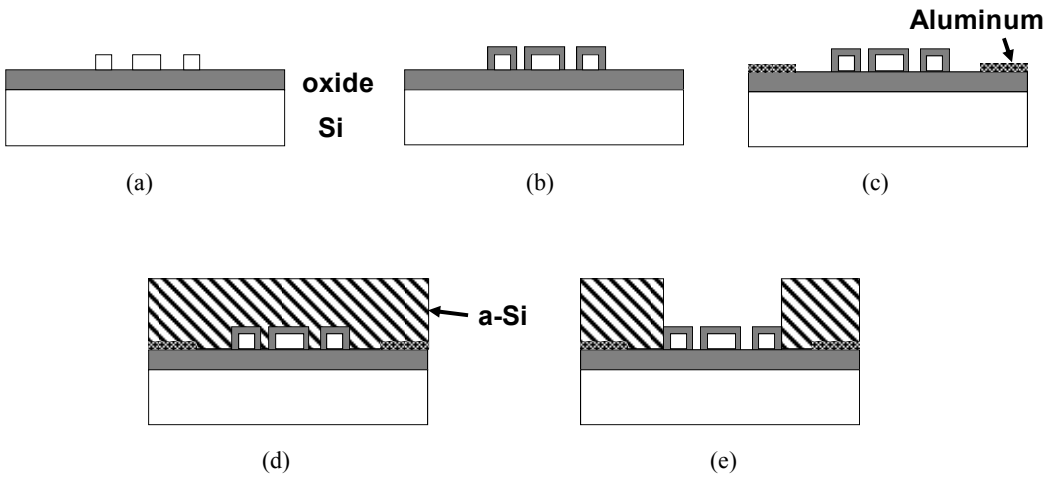

Figure 6.19 Fabrication processes of PLOET integrated with waveguides and matching wells for microdisk laser assembly. (a) Waveguides and pedestals are patterned on SOI wafers. (b) Thermal oxide is grown on top of the waveguides and pedestal to determine the coupling from the assembled microdisk laser to the waveguides. (c) 100-nm-thick aluminum is patterned as electrodes. (d) The 0.8-μm-thick a-Si layer photoconductive layer is deposited. (e) Matching wells are created by dry etching to define where the microdisk lasers will be assembled.

An SEM image of fabricated devices is shown in Figure 6.20. The matching wells are designed for 6-μm-diameter microdisk laser assembly, while the dimensions of the waveguides are 850 nm wide and 100 nm thick. The 200-nm-thick thermal oxide on top of the waveguides determines the coupling from the microdisk lasers to the output waveguides. The detailed design of microdisk lasers and the waveguide coupling has been described in Chapter 4.

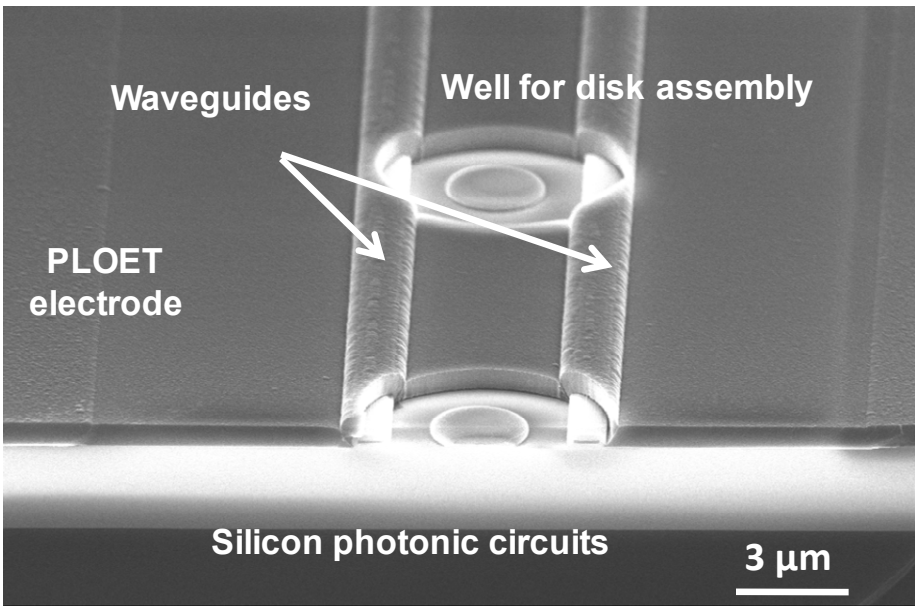

Figure 6.20 An SEM image of a fabricated PLOET device integrated with waveguides and matching wells for microdisk laser assembly. The wells are designed for 6-µm-diameter microdisk lasers. The dimensions of the silicon waveguides are 850 nm wide and 100 nm thick topped by 200-nm-thick oxide as the coupling gap.

6.4.2 Microdisk Laser Assembly Using PLOET

The operation of PLOET is described in Section 5.4. Figure 6.21 depicts a series of microscope images showing how a 6-µm-diameter microdisk laser is assembled and aligned to the silicon waveguides using PLOET with matching wells. Two rectangular optical patterns are illuminated on the device as a pair of tweezers that pick and transport the microdisk laser over the matching well, which is also 6-µm in diameter. Once the microdisk laser is transported over the well, it drops into the well by gravity. The microdisk laser is held in the well until the liquid dries, and assembled onto the output silicon waveguides by van der Waals forces.

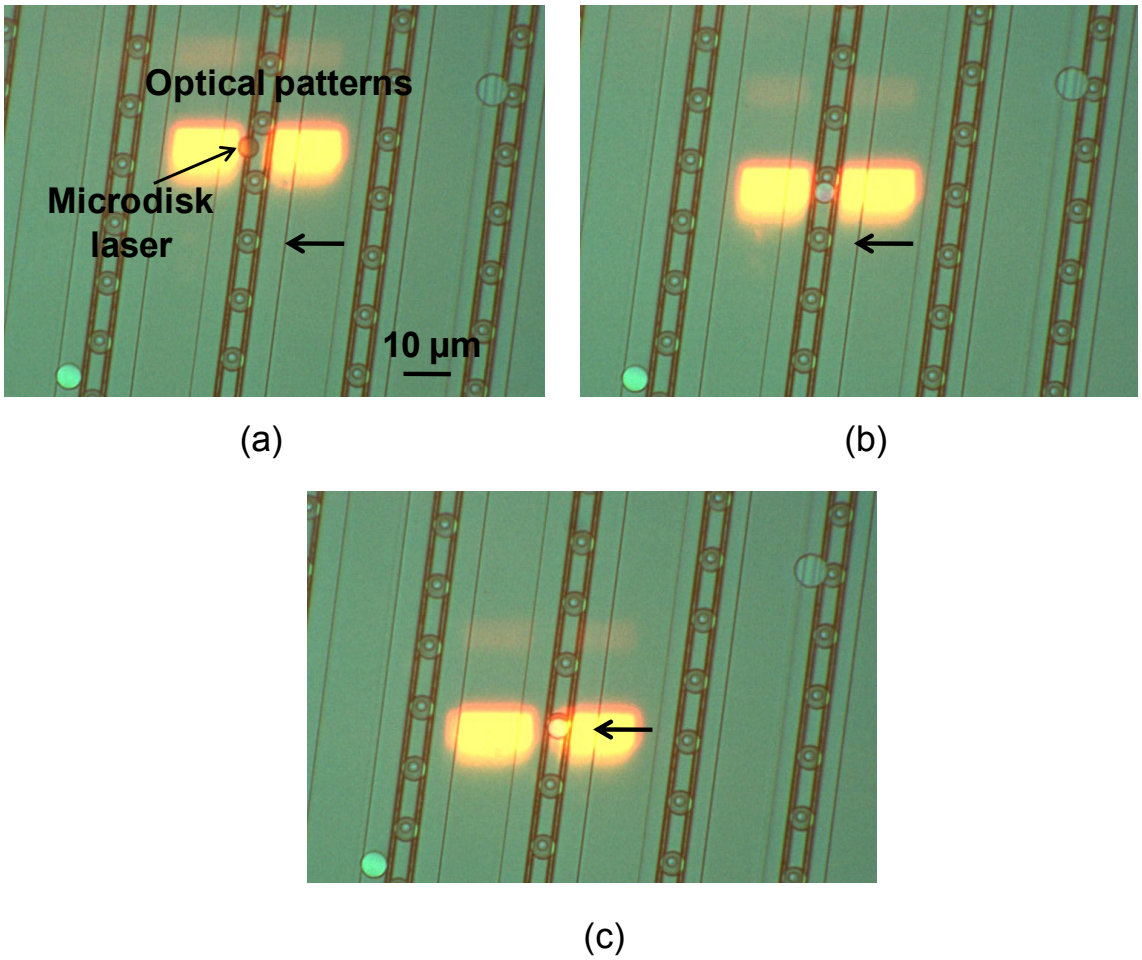

Figure 6.21 Microscope images of microdisk laser assembly onto silicon photonic circuits integrated with PLOET. The rectangular optical patterns act as extensions of the metal electrodes, which induce DEP forces and attract microdisk lasers. The optical patterns act as a pair of tweezers that pick and transport the microdisk over the matching well (where the arrow indicates), and then drop it into the well. The microdisk is held in the well by gravity until dry.

Figure 6.22(a) displays an SEM image of assembled 6-μm-diameter microdisks in the matching wells with the assistance of PLOET. Silicon waveguide circuits are buried under the a-Si layer, and only the target for assembly is exposed by dry etching. On the upper-right corner of Figure 6.22(a), a microdisk is tightly held in the matching well with lithographic alignment accuracy.

After assembly, the a-Si layer has to be removed by XeF_2 to avoid optical mode interference between microdisk lasers and a-Si. Figure 6.22(b) displays the assembled 6-μm-diameter microdisk lasers on silicon waveguides after removing the a-Si layer. It can be clearly seen that the microdisk sits on the pedestal and aligns to the silicon output waveguides for on-chip optical routing.

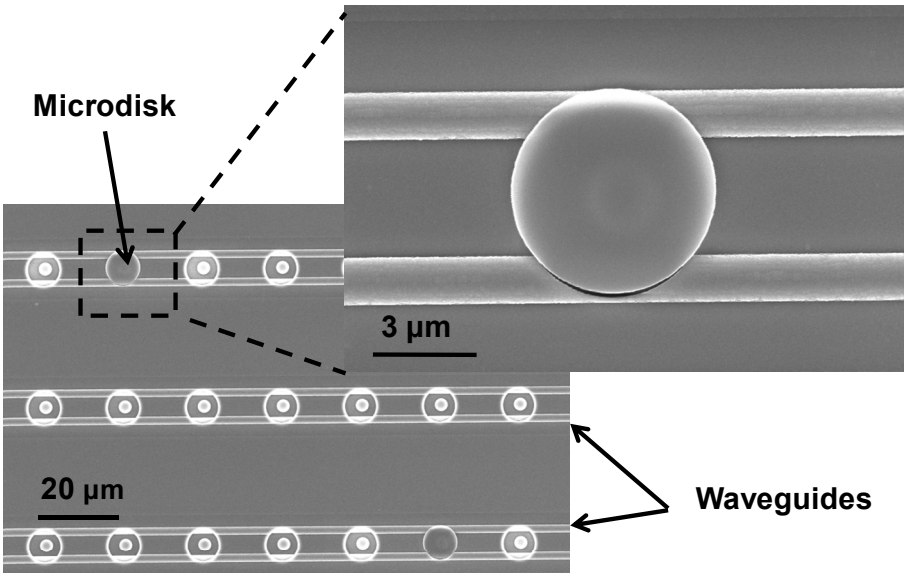

(a)

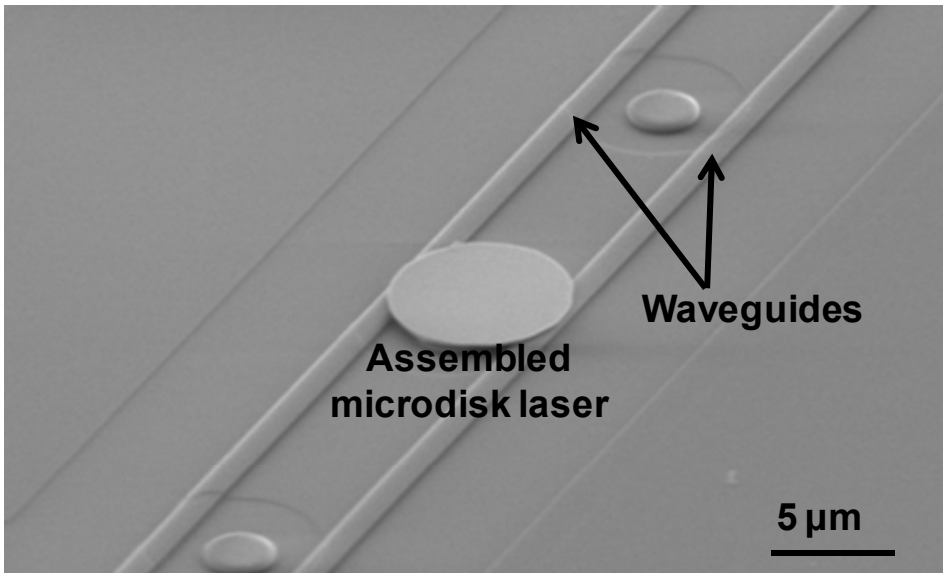

(b)

Figure 6.22 (a) Assembled 6-μm-diameter microdisks in the matching wells on PLOET devices before removing a-Si. Each matching well has optical waveguides and pedestals on the bottom for microdisk assembly. The upper-right inset shows a close-up image of the assembly microdisk. (b) The assembled 6-μm-diameter microdisk laser aligned to the output silicon waveguides after removing the a-Si layer by XeF_2.

6.4.3 Laser Characterization

The assembled microdisk lasers are optically pumped at room temperature (17^{o}C) using a 635-nm diode laser with 0.3-μs pulses and a 33.3 kHz repetition rate (1% duty cycle). The optical measurement setup is slightly different from that used for microdisk lasers without integrated waveguides (Figure 6.5). The optical pump is focused on the microdisks from the top using a 25× objective, as shown in Figure 6.23. A lensed fiber is used to collect the laser power from the cleaved facet of the waveguide because the emitted light is evanescently coupled from microdisk lasers to the underlying silicon waveguide on SOI. The lensed fiber is attached on a piezo-controlled three dimensional stage to precisely control the coupling from the silicon waveguide to the lensed fiber. Typical waveguide-to-fiber coupling loss is approximately 10 dB. With an advanced optical mode converter design it can be reduced to 1 ~ 3 dB [117-120].

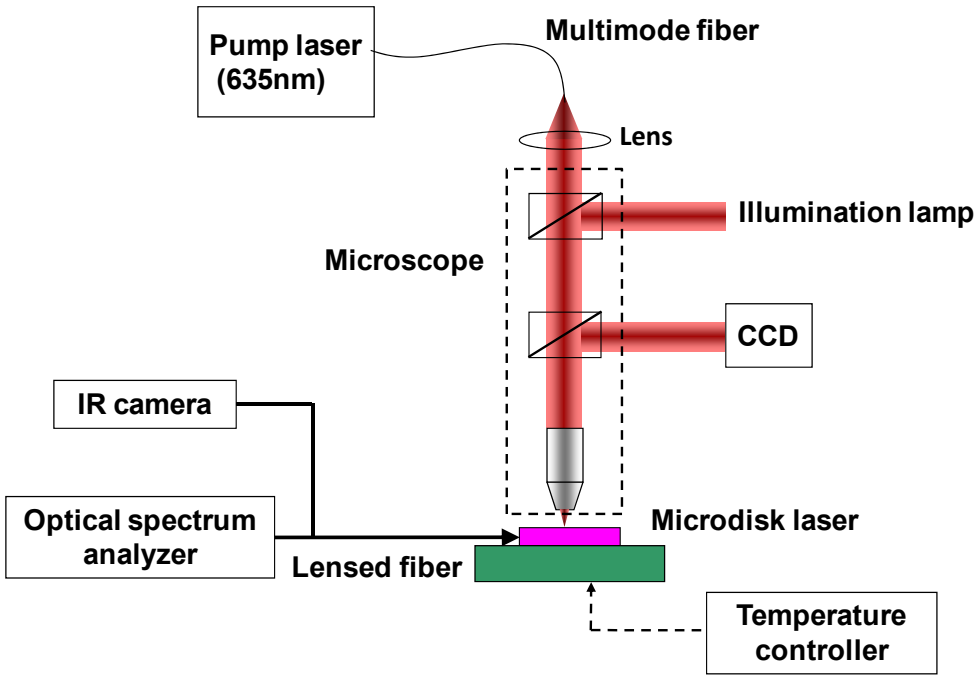

Figure 6.23 Optical measurement setup for assembled microdisk lasers on silicon photonic circuits.

The L-L curve of a 6-μm-diameter microdisk laser assembled and aligned to a silicon waveguide is shown in Figure 6.24(a), while the L-L curve on a logarithmic scale is shown in Figure 6.24(b). The effective threshold peak power of the microdisk laser is approximately 0.45 mW under a 635-nm diode pump laser excitation. A near-field infrared image of the cleaved waveguide was taken using an infrared camera with a 60× objective and shown in the inset of Figure 6.24(a). It should be mentioned that the laser output power was measured at one end of the waveguides for the L-L curve. There are two degenerate modes in microdisk lasers in clockwise and counterclockwise directions, which are both coupled to the waveguides but propagate in opposite directions. Therefore, we observed similar outputs at both ends of the waveguide. To extract differential quantum efficiency of the microdisk laser from the L-L curve, we take the output powers

at both ends into consideration. With an 850 nm by 100 nm silicon output waveguide separated from the microdisk laser by 200-nm-thick silicon dioxide, the extracted differential quantum efficiency is approximately 9.3%, which can be further optimized by adjusting the coupling spacing between the waveguide and the microdisk laser as described in Section 4.3. A maximum laser output at a single end of the waveguide was measured about 90 μW with 6.6 mW pump power.

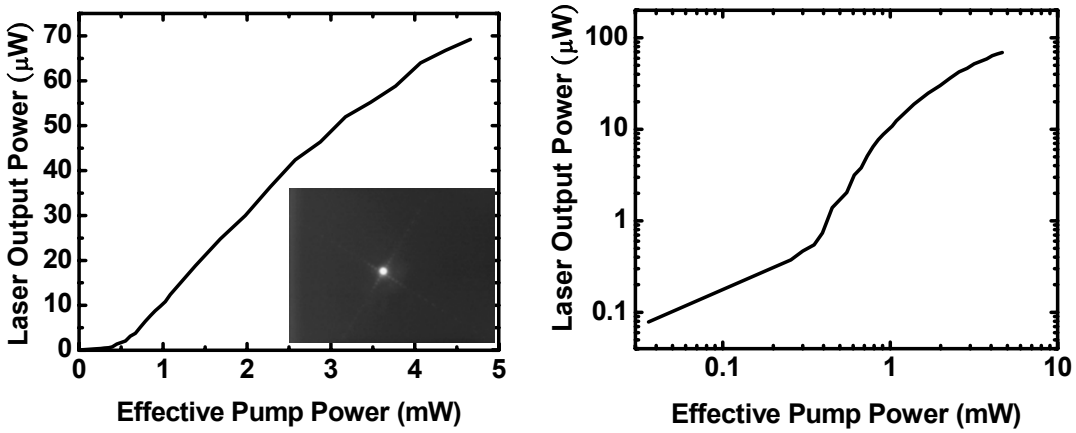

(a) (b)

Figure 6.24 L-L curve of 6-μm-diameter microdisk laser assembled and aligned to an output waveguide. The effective threshold pump power is approximately 0.6 mW under a 635-nm diode laser excitation, and the extracted differential quantum efficiency is about 7%. The near-field infrared of the cleaved waveguide facet is shown in the upper-left inset, and logarithmically-scaled L-L curve is shown in the lower-right inset.

The measured laser spectra are depicted in Figure 6.25. Under 0.45 mW excitation, single mode lasing is achieved with a peak wavelength of 1572.6 nm (Figure 6.25(a)). The measured linewidth is 23 pm, which is limited by the resolution bandwidth of the optical spectrum analyzer (inset of Figure 6.25(a)). At high pump powers, a second whispering-gallery mode with 15-dB suppression is observed as shown in Figure 6.25(b).

The free spectral range of the fundamental modes is 37.4nm with a corresponding group index of 3.4, which is consistent with theoretical calculations for fundamental TE-polarized whispering-gallery mode.

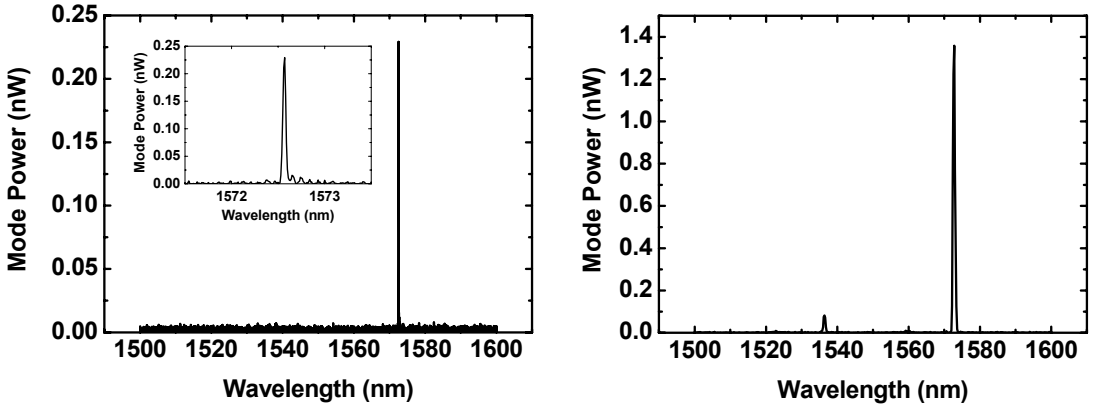

(a) (b)

Figure 6.25 Microdisk laser spectra under different pump powers. (a) Single mode lasing spectrum with a peak wavelength of 1572.6 nm under 0.45 mW excitation. The inset shows linewidth of the laser is approximately 23 pm limited by equipment resolution. (b) Laser spectrum under 2 mW excitation. The free spectral range is 37.4 nm.

Chapter 7 Conclusions and Perspectives

7.1 Conclusions

Optical microresonators are the key building block for many photonic integrated circuits (PIC) areas. The applications include laser sources [85], modulators [54], filters [11], switches [46], dispersion compensators [121], nonlinear optical devices [122], and sensors [123]. Tuning of the microresonators enables dynamic control and reconfigurable functions. Conventional tuning mechanisms such as a free carrier injection [54], the electro- and thermo-optical effect [52, 53], the gain-trimming effect [48], and the electroabsorption effect [47] have been used to modulate the loss and resonance wavelengths of the resonator. Recently, the tuning of the power coupling ratio between the resonator and the integrated waveguide couplers has been reported using MEMS actuators [45, 60, 63]. The Q factor is demonstrated to be tuned from 3,400 to 100,000 for microdisk resonators [60], and 5,400 to 110,000 for microtoroidal resonators [45]. However, the bonding process increases the difficulty for integration with CMOS circuits.

In this dissertation, we demonstrate a microring resonator with laterally-actuated waveguide couplers. The tunable power coupling ratio between the waveguides and the microring resonator was achieved using electrostatic MEMS actuators to move the waveguides, and thus control the gap spacing. The Q factor was tuned from 16,300 to 88,400. Two applications of this tunable microring resonator were also demonstrated: ON-OFF wavelength switches and tunable optical add-drop filters. Both of them exhibit an extinction ratio of 20 dB and an optical bandwidth of 10 GHz.

A doublet was observed in the transmission spectrum because of the intercoupling of the clockwise and counterclockwise modes caused by backscattering in the microring resonator. Coupled-mode theory was used to study the behavior of the doublet, and the mode splitting was found related to the backscattering power ratio, intrinsic cavity loss, and the power coupling ratio between the microring resonator and the waveguide couplers. With the introduction of the backscattering power ratio, the coupling regimes of microresonators are re-defined as: (1) under-coupled regime when $\kappa^2 < \gamma_0^2 + \beta^2$, (2) critically-coupled regime when $\kappa^2 = \gamma_0^2 + \beta^2$, (3) over-coupled regime when $\kappa^2 > \gamma_0^2 + \beta^2$.

We also discussed the design and fabrication issues of the MEMS actuators. The most serious problems of MEMS structures and actuators are stress-induced buckling and the pull-in effect. The buckling was alleviated using prebent waveguides to reduce the structure sensitivity to the stress. The pull-in problem was solved by properly designing actuators with a long traveling range. The actuator electrodes were placed close to the anchors of the waveguides, resulting in an absence of force in the middle region of the

waveguides. As a result, the traveling range of the center of the waveguides was increased. In addition, the whole device was fabricated using CMOS-compatible processes. Therefore, electronic driver circuits can be potentially integrated with the tunable microring resonator.

In order to realize electronic and photonic integrated circuits (EPIC), CMOS-compatible photonic devices are desirable. Silicon optical modulators [54], filters [11], switches [46], and photodetectors [15, 16] have all been demonstrated. However, it is still challenging to directly integrate electrically-pumped lasers on silicon because of the indirect bandgap. Heterogeneous integration of III-V semiconductor lasers on silicon is an alternative to bring light sources to electronic circuits. Integration of III-V lasers on silicon using low-temperature wafer bonding and flip-chip bond techniques have successfully been demonstrated [24, 25]. However, the advances of CMOS in low-dielectric-constant (low-k) material for interconnect layers reduce the thermal budget for post-CMOS processes. In addition, the surface topography presents a challenge for wafer bonding. These increase the difficulty for the integration of lasers on advanced CMOS circuits. Therefore, we propose and demonstrate a post-CMOS, room-temperature fluidic process to assemble III-V microdisk lasers onto silicon platforms with the assistance of optoelectronic tweezers (OET).

OET has been demonstrated for massively parallel fluidic micro- and nano-particle manipulation using projected optical images [105]. A variation of OET, lateral-field optoelectronic tweezers (LOET), provides the capability of integration with PICs on silicon. We have demonstrated InGaAsP microdisk laser assembly on silicon photonic

circuits using LOET with lithographic alignment accuracy. The assembled microdisk lasers exhibit a threshold pump of 0.6 mW and a maximum output power of 90 μW at room temperature under pulsed conditions. The light was evanescently coupled to the waveguides on SOI for on-chip optical routing.

7.2 Future Work

The future work of heterogeneous integration of III-V semiconductor lasers onto silicon photonic circuits can be divided into the following areas: (1) laser performance improvement, and (2) optofluidic self-assembly process with the assistance of LOET. In this dissertation, we have demonstrated the assembly of room-temperature optically-pumped microdisk lasers onto silicon photonic circuits. The next goal is to integrate continuous-wave (CW) electrically-pumped lasers on silicon platforms. This could be achieved by designing the proper epitaxial structure of the microdisk laser and metal contacts. The metal electrodes can be patterned on the III-V microdisk lasers and the silicon platform where the microdisk lasers will be assembled, such as the bottom of the matching wells for microdisk lasers (described in Chapter 6). Once the assembly is finished, the metal contacts on the microdisk lasers are connected to the electrodes on silicon. In addition, a better heat sink path can be designed via metal to the silicon substrate, and thus CW lasing is feasible.

From the perspective of optofluidic assembly, a fluidic self-assembly process will be the future goal while LOET will play the role of assisting the assembly, in coarse movement and assembly defect repair. Direct image controlled LOET can further offer

massively parallel microdisk laser assembly via a computer program. The whole assembly can be automated instead of manually controlled.

BIBLIOGRAPHY

[1] A. F. Benner, M. Ignatowski, J. A. Kash, D. M. Kuchta, and M. B. Ritter, "Exploitation of optical interconnects in future server architectures," *IBM Journal of Research and Development,* vol. 49, pp. 755-775, 2005.

[2] L. Schares, J. A. Kash, F. E. Doany, C. L. Schow, C. Schuster, D. M. Kuchta, P. K. Pepeljugoski, J. M. Trewhella, C. W. Baks, R. A. John, L. Shan, Y. H. Kwark, R. A. Budd, P. Chiniwalla, F. R. Libsch, J. Rosner, C. K. Tsang, C. S. Patel, J. D. Schaub, R. Dangel, F. Horst, B. J. Offrein, D. Kucharski, D. Guckenberger, S. Hegde, H. Nyikal, C. K. Lin, A. Tandon, G. R. Trott, M. Nystrom, D. P. Bour, M. R. T. Tan, and D. W. Dolfi, "Terabus: Terabit/second-class card-level optical interconnect technologies," *IEEE Journal of Selected Topics in Quantum Electronics,* vol. 12, pp. 1032-1044, Sep-Oct 2006.

[3] D. V. Plant and A. G. Kirk, "Optical interconnects at the chip and board level: Challenges and solutions," *Proceedings of the IEEE,* vol. 88, pp. 806-818, Jun 2000.

[4] E. Cassan, S. Laval, S. Lardenois, and A. Koster, "On-chip optical interconnects with compact and low-loss light distribution in silicon-on-insulator rib waveguides," *IEEE Journal of Selected Topics in Quantum Electronics,* vol. 9, pp. 460-464, Mar-Apr 2003.

[5] G. Chen, H. Chen, M. Haurylau, N. A. Nelson, D. H. Albonesi, P. M. Fauchet, and E. G. Friedman, "Predictions of CMOS compatible on-chip optical interconnect," *Integration, The VLSI Journal,* vol. 40, pp. 434-46, 2007.

[6] M. J. Kobrinsky, B. A. Block, J.-F. Zheng, B. C. Barnett, E. Mohammed, M. Reshotko, F. Robertson, S. List, I. Young, and K. Cadien, "On-chip optical interconnects," *Intel Technology Journal,* vol. 8, pp. 129-142, 2004.

[7] D. A. B. Miller, "Device Requirements for Optical Interconnects to Silicon Chips," *Proceedings of the IEEE,* vol. 97, pp. 1166-1185, 2009.

[8] A. S. Liu, R. Jones, L. Liao, D. Samara-Rubio, D. Rubin, O. Cohen, R. Nicolaescu, and M. Paniccia, "A high-speed silicon optical modulator based on a metal-oxide-semiconductor capacitor," *Nature,* vol. 427, pp. 615-618, Feb 2004.

[9] M. Lipson, "Compact Electro-Optic Modulators on a Silicon Chip," *IEEE Journal of Selected Topics in Quantum Electronics,* vol. 12, pp. 1520-1526, 2006.

[10] A. S. Liu, L. Liao, D. Rubin, H. Nguyen, B. Ciftcioglu, Y. Chetrit, N. Izhaky, and M. Paniccia, "High-speed optical modulation based on carrier depletion in a silicon waveguide," *Optics Express,* vol. 15, pp. 660-668, Jan 2007.

[11] B. E. Little, S. T. Chu, P. P. Absil, J. V. Hryniewicz, F. G. Johnson, E. Seiferth, D. Gill, V. Van, O. King, and M. Trakalo, "Very high-order microring resonator filters for WDM applications," *IEEE Photonics Technology Letters,* vol. 16, pp. 2263-2265, Oct 2004.

[12] E. J. Klein, D. H. Geuzebroek, H. Kelderman, G. Sengo, N. Baker, and A. Driessen, "Reconfigurable optical add-drop multiplexer using microring resonators," *IEEE Photonics Technology Letters,* vol. 17, pp. 2358-2360, Nov 2005.

[13] V. R. Almeida, C. A. Barrios, R. R. Panepucci, and M. Lipson, "All-optical control of light on a silicon chip," *Nature,* vol. 431, pp. 1081-1084, Oct 2004.

[14] Y. Vlasov, W. M. J. Green, and F. Xia, "High-throughput silicon nanophotonic wavelength-insensitive switch for on-chip optical networks," *Nature Photonics,* vol. 2, pp. 242-246, Apr 2008.

[15] S. J. Koester, J. D. Schaub, G. Dehlinger, and J. O. Chu, "Germanium-on-SOI infrared detectors for integrated photonic applications," *IEEE Journal of Selected Topics in Quantum Electronics,* vol. 12, pp. 1489-1502, Nov-Dec 2006.

[16] Y. M. Kang, H. D. Liu, M. Morse, M. J. Paniccia, M. Zadka, S. Litski, G. Sarid, A. Pauchard, Y. H. Kuo, H. W. Chen, W. S. Zaoui, J. E. Bowers, A. Beling, D. C. McIntosh, X. G. Zheng, and J. C. Campbell, "Monolithic germanium/silicon avalanche photodiodes with 340 GHz gain-bandwidth product," *Nature Photonics,* vol. 3, pp. 59-63, Jan 2009.

[17] A. Narasimha, B. Analui, Y. Liang, T. J. Sleboda, S. Abdalla, E. Balmater, S. Gloeckner, D. Guckenberger, M. Harrison, R. G. M. P. Koumans, D. Kucharski, A. Mekis, S. Mirsaidi, S. Dan, and T. Pinguet, "A Fully Integrated 4 x 10-Gb/s DWDM Optoelectronic Transceiver Implemented in a Standard 0.13 mm CMOS SOI Technology," *IEEE Journal of Solid-state Circuits,* vol. 42, pp. 2736-2744, 2007.

[18] J. V. Campenhout, P. R. A. Binetti, P. R. Romeo, P. Regreny, C. Seassal, X. J. M. Leijtens, T. de Vries, Y. S. Oei, R. P. J. van Veldhoven, R. Notzel, L. Di Cioccio, J. M. Fedeli, M. K. Smit, D. Van Thourhout, and R. Baets, "Low-Footprint Optical Interconnect on an SOI Chip Through Heterogeneous Integration of InP-Based Microdisk Lasers and Microdetectors," *IEEE Photonics Technology Letters,* vol. 21, pp. 522-524, Apr 2009.

[19] O. Boyraz and B. Jalali, "Demonstration of a silicon Raman laser," *Optics Express,* vol. 12, pp. 5269-5273, Oct 2004.

[20] H. Rong, A. Liu, R. Jones, O. Cohen, D. Hak, R. Nicolaescu, A. Fang, and M. Paniccia, "A continuous-wave Raman silicon laser," *Nature,* vol. 433, pp. 725-728, Feb 2005.

[21] G. Balakrishnan, A. Jallipalli, P. Rotella, S. H. Huang, A. Khoshakhlagh, A. Amtout, S. Krishna, L. R. Dawson, and D. L. Huffaker, "Room-temperature optically pumped (Al)GaSb vertical-cavity surface-emitting laser monolithically grown on an Si(100) substrate," *IEEE Journal of Selected Topics in Quantum Electronics,* vol. 12, pp. 1636-1641, Nov-Dec 2006.

[22] D. Pasquariello and K. Hjort, "Plasma-assisted InP-to-Si low temperature wafer bonding," *IEEE Journal of Selected Topics in Quantum Electronics,* vol. 8, pp. 118-131, Jan-Feb 2002.

[23] G. Roelkens, J. Brouckaert, D. Van Thourhout, R. Baets, R. Notzel, and M. Smit, "Adhesive bonding of InP/InGaAsP dies to processed silicon-on-insulator wafers using DVS-bis-benzocyclobutene," *Journal of the Electrochemical Society,* vol. 153, pp. G1015-G1019, 2006.

[24] A. W. Fang, H. Park, O. Cohen, R. Jones, M. J. Paniccia, and J. E. Bowers, "Electrically pumped hybrid AlGaInAs-silicon evanescent laser," *Optics Express,* vol. 14, pp. 9203-9210, Oct 2006.

[25] J. V. Campenhout, P. Rojo-Romeo, P. Regreny, C. Seassal, D. Van Thourhout, S. Verstuyft, L. Di Cioccio, J. M. Fedeli, C. Lagahe, and R. Baets, "Electrically pumped InP-based microdisk lasers integrated with a nanophotonic silicon-on-insulator waveguide circuit," *Optics Express,* vol. 15, pp. 6744-6749, May 2007.

[26] H. T. Hattori, C. Seassal, E. Touraille, P. Rojo-Rmeo, X. Letartre, G. Hollinger, P. Viktorovitch, L. Di Cioccio, M. Zussy, L. El Melhaoui, and J. M. Fedeli, "Heterogeneous integration of microdisk lasers on silicon strip waveguides for optical interconnects," *IEEE Photonics Technology Letters,* vol. 18, pp. 223-225, Jan-Feb 2006.

[27] D. R. Rowland and J. D. Love, "Evanescent-wave coupling of whispering-gallery modes of a dielectric cylinder," *IEE Proceedings-J Optoelectronics,* vol. 140, pp. 177-188, Jun 1993.

[28] M. L. Gorodetsky and V. S. Ilchenko, "Optical microsphere resonators: optimal coupling to high-Q whispering-gallery modes," *Journal of the Optical Society of America B-Optical Physics,* vol. 16, pp. 147-154, Jan 1999.

[29] Y. L. Pan and R. K. Chang, "Highly efficient prism coupling to whispering gallery modes of a square m cavity," *Applied Physics Letters,* vol. 82, pp. 487-489, Jan 2003.

[30] N. Dubreuil, J. C. Knight, D. K. Leventhal, V. Sandoghdar, J. Hare, and V. Lefevre, "Eroded monomode optical fiber for whispering-gallery mode excitation in fused-silica microspheres," *Optics Letters,* vol. 20, pp. 813-815, Apr 1995.

[31] A. Serpenguzel, S. Arnold, and G. Griffel, "Excitation of resonances of microspheres on an optical fiber," *Optics Letters,* vol. 20, pp. 654-656, Apr 1995.

[32] V. S. Ilchenko, X. S. Yao, and L. Maleki, "Pigtailing the high-Q microsphere cavity: a simple fiber coupler for optical whispering-gallery modes," *Optics Letters,* vol. 24, pp. 723-725, Jun 1999.

[33] J. C. Knight, G. Cheung, F. Jacques, and T. A. Birks, "Phase-matched excitation of whispering-gallery-mode resonances by a fiber taper," *Optics Letters,* vol. 22, pp. 1129-1131, Aug 1997.

[34] M. Cai, O. Painter, and K. J. Vahala, "Observation of critical coupling in a fiber taper to a silica-microsphere whispering-gallery mode system," *Physical Review Letters,* vol. 85, pp. 74-77, Jul 2000.

[35] T. M. Benson, S. V. Boriskina, P. Sewell, A. Vukovic, S. C. Greedy, and A. I. Nosich, "Micro-optical resonators for microlasers and integrated optoelectronics," in *Frontiers in planar lightwave circuit technology*. vol. 216: Springer Nethelands, 2006, pp. 39-70.

[36] M. Borselli, T. J. Johnson, and O. Painter, "Beyond the Rayleigh scattering limit in high-Q silicon microdisks: theory and experiment," *Optics Express,* vol. 13, pp. 1515-1530, Mar 2005.

[37] E. A. J. Marcatili, "Dielectric rectangular waveguide and directional coupler for integrated optics," *Bell System Technical Journal,* vol. 48, pp. 2071-102, 1969.

[38] K. Okamoto, *Fundamentals of Optical Waveguides*. London: Elsevier Inc., 2006.

[39] M. Matsuhara and A. Watanabe, "Coupling of curved transmission lines, and application to optical directional couplers," *Journal of the Optical Society of America,* vol. 65, pp. 163-168, 1975.

[40] H. A. Haus, *Waves and fields in optoelectronics*. New Jersey: Prentice Hall, 1983.

[41] M. L. Gorodetsky, A. D. Pryamikov, and V. S. Ilchenko, "Rayleigh scattering in high-Q microspheres," *Journal of the Optical Society of America B-Optical Physics,* vol. 17, pp. 1051-1057, Jun 2000.

[42] T. J. Kippenberg, S. M. Spillane, and K. J. Vahala, "Modal coupling in traveling-wave resonators," *Optics Letters,* vol. 27, pp. 1669-1671, Oct 2002.

[43] D. S. Weiss, V. Sandoghdar, J. Hare, V. Lefevreseguin, J. M. Raimond, and S. Haroche, "Splitting of high-Q Mie modes induced by ligh backscattering in silica microspheres," *Optics Letters,* vol. 20, pp. 1835-1837, Sep 1995.

[44] M. Soltani, S. Yegnanarayanan, and A. Adibi, "Ultra-high Q planar silicon microdisk resonators for chip-scale silicon photonics," *Optics Express,* vol. 15, pp. 4694-4704, Apr 2007.

[45] J. Yao, D. Leuenberger, M. C. M. Lee, and M. C. Wu, "Silicon microtoroidal resonators with integrated MEMS tunable coupler," *IEEE Journal of Selected Topics in Quantum Electronics,* vol. 13, pp. 202-208, Mar-Apr 2007.

[46] G. N. Nielson, D. Seneviratne, F. Lopez-Royo, P. T. Rakich, Y. Avrahami, M. R. Watts, H. A. Haus, H. L. Tuller, and G. Barbastathis, "Integrated wavelength-selective optical MEMS switching using ring resonator filters," *IEEE Photonics Technology Letters,* vol. 17, pp. 1190-1192, Jun 2005.

[47] K. Djordjev, S. J. Choi, S. J. Choi, and P. D. Dapkus, "Vertically coupled InP microdisk switching devices with electroabsorptive active regions," *IEEE Photonics Technology Letters,* vol. 14, pp. 1115-1117, Aug 2002.

[48] K. Djordjev, S. J. Choi, S. J. Choi, and P. D. Dapkus, "Gain trimming of the resonant characteristics in vertically coupled InP microdisk switches," *Applied Physics Letters,* vol. 80, pp. 3467-3469, May 2002.

[49] K. Djordjev, C. Seung-June, C. Sang-Jun, and P. D. Dapkus, "Active semiconductor microdisk switching devices utilizing gain and electroabsorption effects," in *Optical Fiber Communication Conference and Exhibit. OFC*, 2002, pp. FA2-1-FA2-3.

[50] P. Rabiei, W. H. Steier, Z. Cheng, W. Chuan-guang, and H. J. Lee, "Polymer micro-ring modulator with 1 THz FSR," in *Technical Digest Summaries of Papers Presented at the Lasers and Electro-Optics, CLEO*, 2002, pp. CPDB8-1-CPDB8-3 vol.2.

[51] H. C. Tapalian, J. P. Laine, and P. A. Lane, "Thermooptical switches using coated microsphere resonators," *IEEE Photonics Technology Letters,* vol. 14, pp. 1118-1120, Aug 2002.

[52] S. T. Chu, B. E. Little, V. Van, J. V. Hryniewicz, P. P. Absil, F. G. Johnson, D. Gill, O. King, F. Seiferth, M. Trakalo, and J. Shanton, "Compact full C-band tunable filters for 50 GHz channel spacing based on high order micro-ring resonators," in *Optical Fiber Communication Conference. OFC*, 2004, p. 3 pp. vol.2.

[53] P. Kopperschmidt, "Tunable band gaps in electro-optical photonic bi-oriented crystals," *Applied Physics B-Lasers and Optics,* vol. 73, pp. 717-720, Nov 2001.

[54] Q. F. Xu, B. Schmidt, S. Pradhan, and M. Lipson, "Micrometre-scale silicon electro-optic modulator," *Nature,* vol. 435, pp. 325-327, May 2005.

[55] K. Djordjev, S. J. Choi, S. J. Choi, and P. D. Dapkus, "Microdisk tunable resonant filters and switches," *IEEE Photonics Technology Letters,* vol. 14, pp. 828-830, Jun 2002.

[56] A. L. Huston and J. D. Eversole, "Strain-sensitive elastic-scattering from cylinders," *Optics Letters,* vol. 18, pp. 1104-1106, Jul 1993.

[57] V. S. Ilchenko, P. S. Volikov, V. L. Velichansky, F. Treussart, V. Lefevre-Seguin, J. M. Raimond, and S. Haroche, "Strain-tunable high-Q optical microsphere resonator," *Optics Communications,* vol. 145, pp. 86-90, Jan 1998.

[58] W. von Klitzing, R. Long, V. S. Ilchenko, J. Hare, and V. Lefevre-Seguin, "Frequency tuning of the whispering-gallery modes of silica microspheres for cavity quantum electrodynamics and spectroscopy," *Optics Letters,* vol. 26, pp. 166-168, Feb 2001.

[59] W. M. J. Green, R. K. Lee, G. A. DeRose, A. Scherer, and A. Yariv, "Hybrid InGaAsP-InP Mach-Zehnder racetrack resonator for thermooptic switching and coupling control," *Optics Express,* vol. 13, pp. 1651-1659, Mar 2005.

[60] M. C. M. Lee and M. C. Wu, "Tunable coupling regimes of silicon microdisk resonators using MEMS actuators," *Optics Express,* vol. 14, pp. 4703-4712, May 2006.

[61] L. Chen, N. Sherwood-Droz, and M. Lipson, "Compact bandwidth-tunable microring resonators," *Optics Letters,* vol. 32, pp. 3361-3363, Nov 2007.

[62] U. Levy, K. Campbell, A. Groisman, S. Mookherjea, and Y. Fainman, "On-chip microfluidic tuning of an optical microring resonator," *Applied Physics Letters,* vol. 88, p. 3, Mar 2006.

[63] M. C. M. Lee and M. C. Wu, "MEMS-Actuated microdisk resonators with variable power coupling ratios," *IEEE Photonics Technology Letters,* vol. 17, pp. 1034-1036, May 2005.

[64] M.-C. Tien, S. Mathai, J. Yao, and M. C. Wu, "Tunable MEMS Actuated Microring Resonators," in *2007 IEEE/LEOS International Conference on Optical MEMS and Nanophotonics*, 2007, pp. 177-178.

[65] E. S. Hung and S. D. Senturia, "Extending the travel range of analog-tuned electrostatic actuators," *Journal of Microelectromechanical Systems,* vol. 8, pp. 497-505, Dec 1999.

[66] J. Cheng, J. Zhe, and X. T. Wu, "Analytical and finite element model pull-in study of rigid and deformable electrostatic microactuators," *Journal of Micromechanics and Microengineering,* vol. 14, pp. 57-68, Jan 2004.

[67] J. H. Kuang and C. J. Chen, "The nonlinear electrostatic behavior for shaped electrode actuators," *International Journal of Mechanical Sciences,* vol. 47, pp. 1172-1190, Aug 2005.

[68] W. Fang and J. A. Wickert, "Post buckling of micromachined beams," *Journal of Micromechanics and Microengineering,* vol. 4, pp. 116-122, Sep 1994.

[69] D. K. Armani, T. J. Kippenberg, S. M. Spillane, and K. J. Vahala, "Ultra-high-Q toroid microcavity on a chip," *Nature,* vol. 421, pp. 925-928, Feb 2003.

[70] T. J. Kippenberg, S. M. Spillane, and K. J. Vahala, "Demonstration of ultra-high-Q small mode volume toroid microcavities on a chip," *Applied Physics Letters,* vol. 85, pp. 6113-6115, Dec 2004.

[71] T. Lehnert, D. M. T. Nguyen, L. Baldi, and M. A. M. Gijs, "Glass reflow on 3-dimensional micro-apertures for electrophysiological measurements on-chip," *Microfluidics and Nanofluidics,* vol. 3, pp. 109-117, Feb 2007.

[72] C. C. Wong, A. Agarwal, N. Balasubramanian, and D. L. Kwong, "Fabrication of self-sealed circular nano/microfluidic channels in glass substrates," *Nanotechnology,* vol. 18, Apr 2007.

[73] H. Kuribayashi, R. Hiruta, R. Shimizu, K. Sudoh, and H. Iwasaki, "Shape transformation of silicon trenches during hydrogen annealing," *Journal of Vacuum Science & Technology A,* vol. 21, pp. 1279-1283, 2003.

[74] H. Kuribayashi, R. Hiruta, R. Shimizu, K. Sudoh, and H. Iwasaki, "Investigation of shape transformation of silicon trenches during hydrogen annealing," *Japanese Journal of Applied Physics Part 2-Letters & Express Letters,* vol. 43, pp. L468-L470, Apr 2004.

[75] M. C. M. Lee and M. C. Wu, "Thermal annealing in hydrogen for 3-D profile transformation on silicon-on-insulator and sidewall roughness reduction," *Journal of Microelectromechanical Systems,* vol. 15, pp. 338-343, Apr 2006.

[76] K. K. Lee, D. R. Lim, L. C. Kimerling, J. Shin, and F. Cerrina, "Fabrication of ultralow-loss Si/SiO2 waveguides by roughness reduction," *Optics Letters,* vol. 26, pp. 1888-1890, Dec 2001.

[77] J. Takahashi, T. Tsuchizawa, T. Watanabe, and S. Itabashi, "Oxidation-induced improvement in the sidewall morphology and cross-sectional profile of silicon wire waveguides," *Journal of Vacuum Science & Technology B,* vol. 22, pp. 2522-2525, Sep-Oct 2004.

[78] W. H. Juan and S. W. Pang, "Controlling sidewall smoothness for micromachined Si mirrors and lenses," *Journal of Vacuum Science & Technology B,* vol. 14, pp. 4080-4084, 1996.

[79] S. Jeong and A. Oshiyama, "Complex diffusion mechanisms of a silicon adatom on hydrogenated Si(100) surfaces: on terraces and near steps," *Surface Science,* vol. 433, pp. 481-485, 1999.

[80] J. Nara, T. Sasaki, and T. Ohno, "Theory of adsorption and diffusion of Si adatoms on H/Si(100) stepped surface," *Journal of Crystal Growth,* vol. 201, pp. 77-80, 1999.

[81] D. B. Kao, J. P. McVittie, W. D. Nix, and K. C. Saraswat, "Two-dimensional thermal oxidation of silicon - 1. experiments," *IEEE Transactions on Electron Devices,* vol. 34, pp. 1008-1017, May 1987.

[82] S. M. K. Thiyagarajan, "Scaled microdisk lasers," in *Department of Electrical Engineering*: University of Southern California, 2001.

[83] S. L. McCall, A. F. J. Levi, R. E. Slusher, S. J. Pearton, and R. A. Logan, "Whispering-gallery mode microdisk lasers," *Applied Physics Letters,* vol. 60, pp. 289-291, Jan 1992.

[84] A. F. J. Levi, R. E. Slusher, S. L. McCall, T. Tanbunek, D. L. Coblentz, and S. J. Pearton, "Room-temperature operation of microdisk lasers with submilliamp threshold current," *Electronics Letters,* vol. 28, pp. 1010-1012, May 1992.

[85] M. Fujita, A. Sakai, and T. Baba, "Ultrasmall and ultralow threshold GaInAsP-InP microdisk injection lasers: design, fabrication, lasing characteristics, and spontaneous emission factor," *IEEE JOURNAL OF SELECTED TOPICS IN QUANTUM ELECTRONICS,* vol. 5, pp. 673-681, 1999.

[86] S. M. K. Thiyagarajan, D. A. Cohen, A. F. J. Levi, S. Ryu, R. Li, and P. D. Dapkus, "Continuous room-temperature operation of microdisk laser diodes," *Electronics Letters,* vol. 35, pp. 1252-1254, 1999.

[87] S. J. Choi, K. Djordjev, S. J. Choi, and P. D. Dapkus, "Microdisk lasers vertically coupled to output waveguides," *IEEE Photonics Technology Letters,* vol. 15, pp. 1330-1332, Oct 2003.

[88] C. Seassal, P. Rojo-Romeo, X. Letartre, P. Viktorovitch, G. Hollinger, E. Jalaguier, S. Pocas, and B. Aspar, "InP microdisk lasers on silicon wafer: CW room temperature operation at 1.6 mm," *Electronics Letters,* vol. 37, pp. 222-223, Feb 2001.

[89] P. R. Romeo, J. Van Campenhout, P. Regreny, A. Kazmierczak, C. Seassal, X. Letartre, G. Hollinger, D. Van Thourhout, R. Baets, M. Fedeli, and L. Di Cioccio, "Heterogeneous integration of electrically driven microdisk based laser sources for optical interconnects and photonic ICs," *Optics Express,* vol. 14, pp. 3864-3871, May 2006.

[90] M.-C. Tien, A. T. Ohta, K. Yu, S. L. Neale, and M. C. Wu, "Heterogeneous integration of InGaAsP microdisk laser on a silicon platform using optofluidic assembly," *Applied Physics A-Materials Science & Processing,* vol. 95, pp. 967-972, Jun 2009.

[91] L. A. Coldren and S. W. Corzine, *Diode Lasers and Photonic Integrated Circuits*. New York: Wiley, 1995.

[92] J. V. Campenhout, P. R. Romeo, D. Van Thourhout, C. Seassal, P. Regreny, L. Di Cioccio, J. M. Fedeli, and R. Baets, "Design and Optimization of Electrically Injected InP-Based Microdisk Lasers Integrated on and Coupled to a SOI Waveguide Circuit," *Journal of Lightwave Technology,* vol. 26, pp. 52-63, 2008.

[93] S. Adachi, *Physical properties of III-V semiconductor compounds: InP, InAs, GaAs, GaP, InGaAs, and InGaAsP*: John Wiley & Sons, 1992.

[94] J. Poprek, *Semiconductor optoelectroni devices: introduction to physics and simulation*. San Diego: Elsevier, 2003.

[95] J. E. Heebner, T. C. Bond, and J. S. Kallman, "Generalized formulation for performance degradations due to bending and edge scattering loss in microdisk resonators," *Optics Express,* vol. 15, pp. 4452-4473, Apr 2007.

[96] Y. A. Vlasov and S. J. McNab, "Losses in single-mode silicon-on-insulator strip waveguides and bends," *Optics Express,* vol. 12, pp. 1622-1631, 2004.

[97] T. Okamoto, N. Nunoya, Y. Onodera, T. Yamazaki, S. Tamura, and S. Arai, "Optically pumped membrane BH-DFB lasers for low-threshold and single-mode operation," *IEEE Journal of Selected Topics in Quantum Electronics,* vol. 9, pp. 1361-1366, Sep-Oct 2003.

[98] E. J. Snyder, J. Chideme, and G. S. W. Craig, "Fluidic self-assembly of semiconductor devices: A promising new method of mass-producing flexible circuitry," *Japanese Journal of Applied Physics,* vol. 41, pp. 4366-4369, 2002.

[99] U. Srinivasan, M. A. Helmbrecht, C. Rembe, R. S. Muller, and R. T. Howe, "Fluidic self-assembly of micromirrors onto microactuators using capillary forces," *IEEE Journal of Selected Topics in Quantum Electronics,* vol. 8, pp. 4-11, Jan-Feb 2002.

[100] S. C. Esener and D. Hartmann, "DNA assisted micro-assembly: A heterogeneous integration technology for optoelectronics," *SPIE Critical Reviews of Optical Science and Technology,* pp. 13-40, 1998.

[101] Y. Murakami, K. Idegami, H. Nagai, T. Kikuchi, Y. Morita, A. Yamamura, K. Yokoyama, and E. Tamiya, "Application of micromachine techniques to

biotechnological research," *Materials Science and Engineering C,* vol. 12, pp. 67-70, 2000.

[102] H.-J. J. Yeh and J. S. Smith, "Fluidic self-assembly for the integration of GaAs light-emitting diodes on Si substrates," *IEEE Photonics Technology Letters,* vol. 6, pp. 706-708, Jun 1994.

[103] J. K. Tu, J. J. Talghader, M. A. Hadley, and J. S. Smith, "Fluidic self-assembly of InGaAs vertical-cavity surface-emitting lasers on silicon," *Electronics Letters,* vol. 31, pp. 1448-1449, Aug 1995.

[104] W. Zheng, P. Buhlmann, and H. O. Jacobs, "Sequential shape-and-solder-directed self-assembly of functional microsystems," *Proceedings of the National Academy of Sciences of the United States of America,* vol. 101, pp. 12814-12817, Aug 2004.

[105] P. Y. Chiou, A. T. Ohta, and M. C. Wu, "Massively parallel manipulation of single cells and microparticles using optical images," *Nature,* vol. 436, pp. 370-372, Jul 2005.

[106] J. H. Wei and S. C. Lee, "Electrical and optical properties of implanted amorphous silicon," *Journal of Applied Physics,* vol. 76, pp. 1033-1040, Jul 1994.

[107] A. T. Ohta, P. Y. Chiou, H. L. Phan, S. W. Sherwood, J. M. Yang, A. N. K. Lau, H. Y. Hsu, A. Jamshidi, and M. C. Wu, "Optically controlled cell discrimination and trapping using optoelectronic tweezers," *IEEE Journal of Selected Topics in Quantum Electronics,* vol. 13, pp. 235-243, Mar-Apr 2007.

[108] T. B. Jones, *Electromechanics of particles*. New York: Cambridge University Press, 1995.

[109] P.-Y. Chiou, "Massively parallel optical manipulation of single cells, micro- and nano-particles on optoelectronic devices," in *Department of Electrical Engineering and Computer Sciences*: Uiversity of California, Berkeley, 2005.

[110] A. T. Ohta, A. Jamshidi, P. J. Pauzauskie, H. Hsan-Yin, Y. Peidong, and M. C. Wu, "Trapping and Transport of Silicon Nanowires Using Lateral-Field Optoelectronic Tweezers," in *Conference on Lasers and Electro-Optics, CLEO*, 2007, pp. 1-2.

[111] A. T. Ohta, "Optofluidic devices for cell, microparticle, and nanoparticle manipulatin," in *Department of Electrical Engineering and Computer Sciences*: University of California, Berkeley, 2008.

[112] A. T. Ohta, S. L. Neale, H. Hsan-Yin, J. K. Valley, and M. C. Wu, "Parallel assembly of nanowires using lateral-field optoelectronic tweezers," in *IEEE/LEOS Internationall Conference on Optical MEMS and Nanophotonics*, 2008, pp. 7-8.

[113] M.-C. Tien, A. T. Ohta, K. Yu, L. C. Chuang, A. Jamshidi, S. L. Neale, C. Hou, C. Chang-Hasnain, and M. C. Wu, "Hybrid microdisk laser on a silicon platform using lateral-field optoelectronic tweezers assembly," in *Conference on Lasers and Electro-Optics and Quantum Electronics and Laser Science. CLEO/QELS*, 2008, pp. 1-2.

[114] T. Baba and D. Sano, "Low-threshold lasing and purcell effect in microdisk lasers at room temperature," *IEEE Journal of Selected Topics in Quantum Electronics,* vol. 9, pp. 1340-1346, Sep-Oct 2003.

[115] W. Kowalsky, H. H. Wehmann, F. Fiedler, and A. Schlachetzki, "Optical absorption and refractive index near the bandgap of InGaAsP," *Physica Status Solidi a - Applied Research,* vol. 77, pp. K75-K80, 1983.

[116] A. T. Ohta, M.-C. Tien, K. Yu, S. L. Neale, and M. C. Wu, "Optofluidic assembly of microdisk lasers on a silicon chip," in *2008 Digest of the IEEE/LEOS Summer Topical Meetings*, 2008, pp. 207-208.

[117] T. Shoji, T. Tsuchizawa, T. Watanabe, K. Yamada, and H. Morita, "Low loss mode size converter from 0.3 mm square Si wire waveguides to singlemode fibres," *Electronics Letters,* vol. 38, pp. 1669-1670, Dec 2002.

[118] V. R. Almeida, R. R. Panepucci, and M. Lipson, "Nanotaper for compact mode conversion," *Optics Letters,* vol. 28, pp. 1302-1304, Aug 2003.

[119] M. Fritze, J. Knecht, C. Bozler, C. Keast, J. Fijol, S. Jacobson, P. Keating, J. LeBlanc, E. Fike, B. Kessler, M. Frish, and C. Manolatou, "Fabrication of three-dimensional mode converters for silicon-based integrated optics," *Journal of Vacuum Science & Technology B,* vol. 21, pp. 2897-2902, 2003.

[120] S. J. McNab, N. Moll, and Y. A. Vlasov, "Ultra-low loss photonic integrated circuit with membrane-type photonic crystal waveguides," *Optics Express,* vol. 11, pp. 2927-2939, Nov 2003.

[121] G. Lenz, B. J. Eggleton, C. K. Madsen, C. R. Giles, and G. Nykolak, "Optimal dispersion of optical filters for WDM systems," *IEEE Photonics Technology Letters,* vol. 10, pp. 567-569, Apr 1998.

[122] T. J. Kippenberg, S. M. Spillane, D. K. Armani, and K. J. Vahala, "Ultralow-threshold microcavity Raman laser on a microelectronic chip," *Optics Letters,* vol. 29, pp. 1224-1226, Jun 2004.

[123] A. M. Armani and K. J. Vahala, "Heavy water detection using ultra-high-Q microcavities," *Optics Letters,* vol. 31, pp. 1896-1898, Jun 2006.